

**FACULTY
OF MATHEMATICS
AND PHYSICS**
Charles University

DOCTORAL THESIS

Stefan Gohl

**Timepix Detector in Space Applications
and Radiation Belt Dynamics Observed
at Low Altitudes**

Department of Surface and Plasma Science

Supervisor of the doctoral thesis: Prof. RNDr. František Němec, PhD

Study programme: Physics of Plasmas and Ionized
Media [P4F2A]

Prague 2024

I declare that I carried out this doctoral thesis on my own, and only with the cited sources, literature and other professional sources. I understand that my work relates to the rights and obligations under the Act No. 121/2000 Sb., the Copyright Act, as amended, in particular the fact that the Charles University has the right to conclude a license agreement on the use of this work as a school work pursuant to Section 60 subsection 1 of the Copyright Act.

In date
Author's signature

I thank my supervisor František Němec for his support, patience and kindness during my time as his PhD student. I further thank Benedikt Bergmann from the Institute of Experimental and Applied Physics (IEAP), who practically acted as my secondary supervisor. I also thank the IEAP for allowing me to pursue my PhD, while being employed at the institute. I thank the people of the Department of Surface and Plasma Science of the Faculty of Mathematics and Physics of the Charles University, who accepted me as a PhD student. Additionally, I thank Miroslava Kassayová and Martin Pichotka for proof reading the thesis and the moral support.

Title: Timepix Detector in Space Applications and Radiation Belt Dynamics Observed at Low Altitudes

Author: Stefan Gohl

Department: Department of Surface and Plasma Science

Supervisor: Prof. RNDr. František Němec, PhD, Department of Surface and Plasma Science

Abstract: Radiation in space is harmful to both satellites and astronauts. Radiation monitors are used to measure the level of radiation on spacecraft, and efforts are made to reduce the resources needed for such devices while improving the data quality. Additionally, the complex response of the magnetospheric system to space weather events is investigated. In 2013, the Space Application of Timepix Radiation Monitor (SATRAM) was launched onboard the Proba-V satellite. The first part of this thesis demonstrates the capabilities of this single-layer Timepix detector. Particle identification methods are developed to distinguish between electrons, protons, and heavier particles, and particle fluxes are determined. These are compared with electron fluxes measured by the Energetic Particle Telescope (EPT) situated on the same satellite, showing reasonable agreement. The second part of the thesis investigates particle flux variations around geomagnetic storms and interplanetary shock arrivals. Five significant geomagnetic storms ($Dst < -100$ nT) are investigated using data from the Instrument for the Detection of Particle (IDP) on the DEMETER spacecraft. The results consider the respective solar wind parameters and demonstrate two distinct types of storms. Additionally, data from the EPT instrument are used to investigate electron flux variations around interplanetary shock arrivals. A delicate L-shell-dependent interplay between enhanced sources and losses is demonstrated.

Keywords: Particle Tracking Detector; Space Radiation Environment; Cross Calibration; Geomagnetic Storm; Interplanetary Shock Arrival

Contents

Introduction	3
1 From Solar Wind to Radiation Belts: A Brief Physical Introduction	5
1.1 Solar Wind	5
1.1.1 Overview	5
1.1.2 Interplanetary Shocks	8
1.2 Earth's Magnetosphere	10
1.2.1 Magnetosphere Structure	10
1.2.2 Magnetic Reconnection	13
1.2.3 Inner Magnetosphere	16
1.3 Radiation Belts	20
1.3.1 Particle Motions and Adiabatic Invariants	21
1.3.2 Particle Dynamics	24
1.3.3 Electron Populations	27
1.4 Geomagnetic Storms and Storm Indices	27
2 Timepix Detector	31
3 Instrumentation	35
3.1 Space Application of Timepix Based Radiation Monitor	35
3.1.1 Noisy Pixels	37
3.2 Energetic Particle Telescope	40
3.3 Instrument for the Detection of Particle	42
4 Particle Identification Methods	45
4.1 Simulation	45
4.2 Decision Tree Method	46
4.3 Energy per Pixel Method	52
4.4 Neural Network	55
4.5 Discussion of Methods	57
5 Comparison of Electron Fluxes Measured by SATRAM and EPT	59
5.1 SATRAM Data Determination of Electron Fluxes	59
5.1.1 Particle Counting	60
5.1.2 Effective Area	61
5.1.3 Geometric Factor	61
5.1.4 Secondary Particles, Track Interruption and Backscattering	62
5.2 SATRAM Comparison with EPT	64
5.3 Discussion of Electrons Flux Comparison	67

6 Electron Flux Variations During Geomagnetic Storms and Interplanetary Shock Arrivals	69
6.1 Energetic Particle Flux Variations Around Significant Geomagnetic Storms	69
6.1.1 Selection of Geomagnetic Storms and Data	70
6.1.2 Evolution of the Energetic Particle Fluxes	70
6.1.3 Evolution of Solar Wind Parameters	74
6.1.4 Observed L Barrier	75
6.2 Impact of Interplanetary Shocks on the Radiation Belt Environment	79
6.2.1 Methodology	79
6.2.2 Results	82
6.3 Discussion of Electron Flux Variations During Geomagnetic Storms and Interplanetary Shock Arrivals	84
Conclusion	87
Acknowledgements	91
Bibliography	93
List of Figures	116
List of Tables	121
List of Abbreviations	123
List of Publications	125
A Attachments	127
A.1 Complete Data for SATRAM comparison with EPT	127

Introduction

Earth's nearest space environment encompasses a complicated, dynamic system of energetic particles in the terrestrial magnetic field. This environment is further characterised by a complex system of currents that significantly affects the configuration of the magnetic field, along with an abundance of plasma waves. Numerous mechanisms, such as wave-particle interactions and the interaction between Earth's magnetic field and the solar wind, are responsible for a constantly varying radiation environment. This complex system has not yet been fully understood and is subject to intense research, both in the preceding and probably in the coming decades. The interest in this radiation environment and the underlying mechanisms has intensified due to the increasing activity of humankind, be it through human space flights or the deployment of satellites in orbits ranging from a few hundred to a few tens of thousands of kilometres in altitude.

It is well known that the radiation is harmful for astronauts and satellite electronics alike. The radiation environment consists mostly of electrons and protons, but also heavier ions up to iron can be found. Additionally, galactic cosmic rays from outside the heliosphere with extremely high energy can cause issues. Electrons are known to contribute to effects like spacecraft surface charging or dielectric charge build-up, as well as ionising doses through direct energy deposition and bremsstrahlung effects. Protons dominate the ionising dose, together with Non-Ionising Energy Loss (NIEL) deposition in a satellite and the Single Event Upset (SEU) rates. The highly fluid nature of the radiation environment adds another layer of threat, as recurring events with variable strength cannot be reliably predicted and protected against at the moment.

Fluctuations in the magnetosphere environment of Earth, as well as other magnetised planets, are driven by the ever-changing solar wind, which is carrying plasma from the Sun's exterior into interplanetary space. The solar wind is a result of the turbulent nature of the Sun itself, whose exact origin is still not unravelled. Local variations of the Sun's magnetic field at its surface can cause the solar wind to be slower or faster. This in turn causes density, pressure, and magnetic field variations within the solar wind plasma. The interaction of the solar wind with Earth's magnetosphere causes – immediately or with a time delay – the radiation environment to vary more or less drastically. This whole phenomenon, the solar wind variations and the consequent changes inside the magnetosphere environment, is generally summarised under the name “space weather”.

To study this perplexing environment, complex detector systems are needed. Given the rather limited access to space due to the necessity of using expensive launching systems to transport satellites into orbit, it is advantageous for these detectors to be small, light weight, and low power consuming. They also need to be robust, as they are usually not serviceable once they are launched into space, with the exception of the International Space Station (ISS). This includes also radiation monitors, which can provide information on the radiation level in real time. There are radiation monitors used as dosimeters for astronauts and for satellites alike. If given some autonomy, these monitors could initiate measures to protect certain electronic parts from radiation damage should they detect a

sudden rise in the radiation level. Additionally, data are frequently sent back to Earth, where they are carefully analysed. The analysis requires the development of sophisticated algorithms in order to extract information about the radiation environment, e.g., the composition of the radiation field or spectral information of the particle fluxes etc. Simulations are another important tool used to understand the detector response, to interpret the data, and to test new physics models.

The Timepix detector is an already well-established tool in medical and high energy physics. It has been used as a personal dosimeter for astronauts on the ISS as well. The aim of this thesis is to demonstrate its viability for particle measurements in the outer space by analysing data from the Space Application of Timepix Radiation Monitor (SATRAM). Therefore, new particle identification algorithms suitable for mixed radiation fields had to be developed. After a brief introduction to the solar wind and magnetosphere physics in Chapter 1 and a brief description of the Timepix detector in Chapter 2, as well as SATRAM together with two other instruments for particle measurements in space in Chapter 3, methods for particle identification in a single layer Timepix detector are presented in Chapter 4. In Chapter 5, the determination of electron fluxes with SATRAM is demonstrated and the results are compared with another particle instrument situated on the same satellite as SATRAM. Another important part of this thesis was to investigate particle flux variations in the radiation belts caused by significant geomagnetic events and interplanetary shocks using low altitude satellite data. The aim was to search for connections between solar wind parameters and their level of impact on the radiation belts. Data obtained by spacecraft in low-altitude polar orbits allow for a high sampling rate across all L-shells, offering an advantageous perspective. These studies are presented in Chapter 6.

1. From Solar Wind to Radiation Belts: A Brief Physical Introduction

In this chapter, the underlying physics needed to understand the research in this thesis shall be explained. It starts with a general overview of the solar wind, the main driver of the dynamic behaviour of Earth's magnetosphere. Then, the structure and mechanics related to the magnetosphere is discussed. The major focus of this research was the response of the radiation belts surrounding Earth to the dynamics mentioned before. Therefore, the next section in this chapter will cover the radiation belts in depth. The last section will touch on geomagnetic storms.

1.1 Solar Wind

1.1.1 Overview

In the 1950s, observations of comet tails, that were always blowing away from the Sun, regardless of their direction of motion [Biermann, 1951, 1952], or indications of then unknown magnetic fields in the interplanetary space [Simpson, 1954, Meyer and Simpson, 1954, Meyer et al., 1956], gave rise to the idea of the Sun emitting material into the interplanetary space. In the 1960s, space probes were able to measure a particle stream coming from the Sun, as well as a temporally varying interplanetary magnetic field [Neugebauer and Snyder, 1966, Ness et al., 1964, 1971]. The solar wind was discovered. Today, it is well known that the solar wind is a supersonic continuous stream of ionised plasma and a remnant of the solar magnetic field. Commonly observed wind speeds range from 250 km/s to 800 km/s at a distance of 1 AU (the distance between Sun and Earth). In extreme cases, the solar wind speed can reach above 1000 km/s. Proton densities at 1 AU reach $2\text{--}20\text{ cm}^{-3}$, electron densities are nearly the same and the helium abundance is about 0.5% to 5% [Cranmer et al., 2017]. Heavier ions like oxygen and carbon appear to a much smaller extent. The solar wind is often divided into slow ($\lesssim 450\text{ km/s}$) and fast ($\gtrsim 450\text{ km/s}$) wind, which originate in regions of different magnetic field configuration and feature different abundances in helium.

How exactly the solar wind is accelerated and heated is still a matter of debate. The first accepted idea came from Parker [Parker, 1958]. He proposed a non-steady equilibrium state between the high-pressure corona ($T \approx 10^6\text{ K}$) and the interstellar medium with a steady outflow of coronal plasma away from the Sun. The solution of Parker's momentum equation suggests that the particles would be accelerated with increasing radial distances from the Sun's corona and reach supersonic speeds at a critical distance. This was confirmed by many observations in the following decades. However, the mechanism that accelerates the particles as well as the mechanism that heats the escaping particles and the Sun's corona is not yet fully understood. There are a number of models that try to explain possible contributions to the acceleration of the solar wind. A further discussion

of the origin of the solar wind would go beyond the scope of this thesis. Further information can be found in, e.g., Cranmer et al. [2017] or Parker [1997].

A more relevant aspect of the solar wind is its magnetic field configuration. From magnetohydrodynamics (MHD) it is known that the magnetic field in a highly conductive plasma is “frozen in” [Gurnett and Bhattacharjee, 2017]. In the particular case of the solar wind, this means, that the magnetic field of the Sun is carried outwards with the solar wind plasma, forming the so-called Interplanetary Magnetic Field (IMF). The field lines of the solar magnetic field can be described as flux tubes. As the plasma flow is strongly intertwined with the magnetic field, the plasma parcel occurring at a given magnetic field line in one location must also occur at that given magnetic field line in another location.

If one considers a purely radially expanding solar wind, one might expect radially oriented magnetic field lines and the magnetic field magnitude of the solar wind would fall off with the radial distance r from the Sun as $1/r^2$. However, it is not that simple. The Sun’s atmosphere at its equator rotates around its axis with an average period of 24.5 days. At higher latitudes the rotation speed slows down. The rotation axis is nearly perpendicular to the ecliptic plane of Earth’s orbit around the Sun, so that the solar wind that passes by the Earth originates near the solar equator. The effect of this rotation is that the source of successive parcels of plasma at the base of a flux tube moves because of the rotation. As a consequence, the magnetic field lines reaching out into the interplanetary space create a spiral. This is called the Parker spiral, which is shown in Figure 1.1.

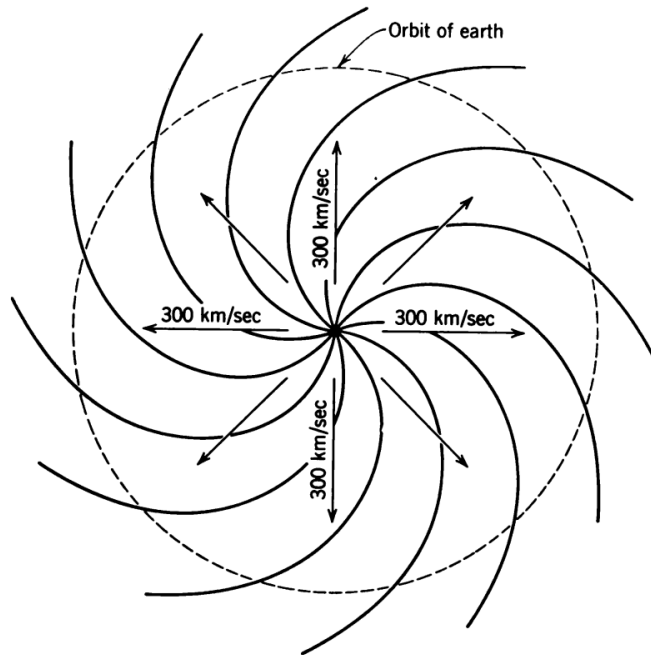


Figure 1.1: Spiral configuration of interplanetary magnetic field lines frozen into a radially expanding solar wind. The orbit of Earth is shown by a dashed curve. Taken from Parker [1963].

Due to the solar rotation, the IMF not only has a radial component B_r , but also an azimuthal component B_ϕ . Considering the Parker spiral magnetic field model and a constant solar rotation rate, the ratio between the IMF azimuthal and radial components depends on the distance from the Sun and the solar wind

speed. For the solar wind speed of 400 km/s, the angle between a straight line from Sun to Earth and a magnetic field line is about 45° , i.e., the B_r and B_ϕ IMF components are nearly the same [Kivelson and Russell, 1995]. The greater the distance from the Sun, the more tightly wound the field lines are.

As mentioned earlier, the solar wind can be classified into fast and slow wind. The fast wind seems to be related to coronal holes [Krieger et al., 1973, Neupert and Pizzo, 1974, McComas et al., 2002]. During the solar minimum, these appear over the poles of the Sun and reach down to mid-latitudes [Marsden, 2001], whereas during the solar maximum coronal holes appear more often at low latitudes. The slow solar wind is associated with any other source region [Suess and Nerney, 2002, Nerney and Suess, 2005]. Some of these regions are called helmet streamers. The magnetic field in these structures forms closed loops at low heights, surrounded by open field lines with opposing polarity converging above a cusp-like point at the top. Another example of the slow wind sources are pseudostreamers. They also feature loops at the bottom, but the outreaching magnetic field lines have the same polarity. Other loop-like magnetic structures are possible sources of the slow solar wind as well.

These sources of the slow wind are more common at lower latitudes. Therefore, solar wind speed measured around Earth corresponds more often to the slow wind, averaging about 400 km/s. This led to the understanding of the slow wind as the ambient solar wind. However, “ambient” does not mean “time-steady” in this regard. The solar wind is highly dynamic and coronal holes can appear at low latitudes even during the steadier solar minimum, resulting in the plasma release into interplanetary space at higher speeds. Then, the faster solar wind will chase after the slower wind. The interaction between the two streams results in both magnetic field and plasma compression at their interface [Pizzo, 1985, Balogh et al., 2000]. A stationary observer in the ecliptic plane would observe a steep increase of the solar wind speed and density, followed by a slow decay and a rarefaction of the solar wind plasma. If the coronal hole persists over a longer time (longer than 27 days), the high-speed streams will appear each solar rotation and give the impression that the streams are corotating with the Sun. Hence, these are called corotating interaction regions (CIRs) [Smith and Wolfe, 1976]. An illustration of these can be found in Figure 1.2.

Another phenomenon that can interrupt the ambient solar wind are Coronal Mass Ejections (CMEs) [Chen, 2011, Mishra and Teriaca, 2023]. In a CME, large-scale magnetised plasma structures are expelled into interplanetary space. These are the most dramatic events in space weather and can reach wind speeds well above 1000 km/s [Yashiro et al., 2004]. Given the high speed of CME’s, the compression of the magnetic field and plasma is more intense than for CIRs. However, CMEs last shorter, only from a few hours to days. The number of CMEs strongly correlates with the solar cycle, being highest during the solar maximum [Tsurutani et al., 2006, Jian et al., 2006]. On the other hand, CIRs depend much less on the solar cycle, appearing slightly more often in the declining phase towards the solar minimum.

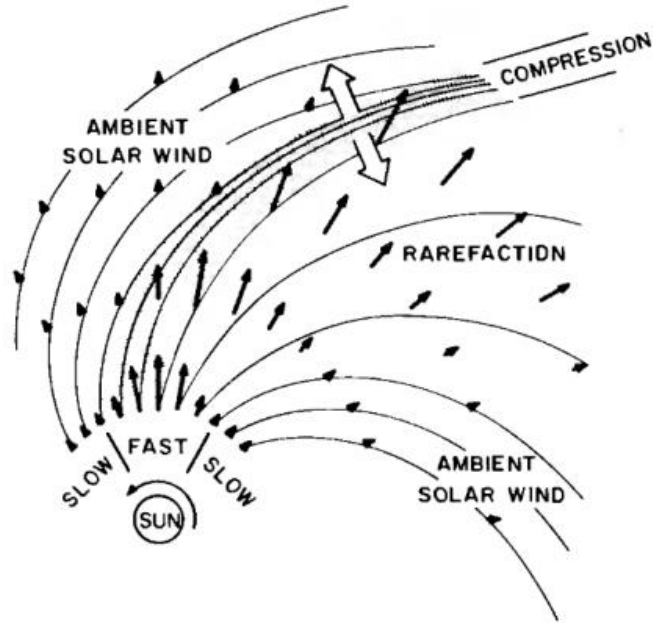


Figure 1.2: An illustration of fast solar wind catching up with slow solar wind causing compression at the front and rarefaction after. The solid arrows show the relative radial component of the wind at each position. The larger hollow arrows show the pressure gradient resulting from the compression of the plasma. Taken from Pizzo [1985].

1.1.2 Interplanetary Shocks

The compression of the plasma in front of CMEs and CIRs leads to a steepening of at least some of the solar wind parameters [Kivelson and Russell, 1995]. If the difference between the speed of the fast stream and the speed of the slow stream is larger than the speed of a relevant wave group velocity, the information about the approaching faster stream cannot reach the ambient solar wind ahead fast enough. The solution to the problems associated with the impossibility of the information transfer at large enough speeds is the formation of shocks in the solar wind, in this particular case called interplanetary shocks (IP shocks). These shocks allow for a non-adiabatic conversion of flow energy into thermal energy, resulting in the plasma heating behind the shock.

The mean free path of particles in the solar wind is calculated to be about 1 AU [Sagdeev and Kennel, 1991]. Therefore, collisions are unlikely to occur and IP shocks are considered collisionless. Momentum and energy among particles are transmitted via magnetic field. Additionally, plasma in the presence of a magnetic field does not only have a single typical speed. The evaluation of possible propagating waves in the magnetohydrodynamic approximation (i.e., at low frequencies) reveals three basic wave types propagating in the plasma medium: Alfvén wave and fast and slow magnetosonic waves. These eventually play a crucial role in the IP shock formation. The unshocked plasma in front of the shock is dubbed upstream and the shocked plasma after the shock is dubbed downstream. The equations describing the plasma condition up- and downstream are called Rankine-Hugoniot jump conditions (e.g., Kivelson and Russell [1995], Oliveira [2017]). The plasma parameters and also the angle between the shock

normal and the IMF vector on the upstream side play a major role in the plasma conditions on the downstream side.

There are different types and classifications of IP shocks [Landau and Lifshitz, 1982, Burlaga, 1995, Tsurutani et al., 2011]. The first classification is based on the direction of the shock propagation. Shocks propagate in the solar wind frame of reference either away or towards the Sun. In the former case, they are called forward shocks and, in the latter case, reverse shocks. However, all IP shocks are carried by the solar wind, and they are thus moving away from the Sun. The second classification considers a particular MHD wave, whose steepening resulted in the shock formation. A necessary condition for the shock to be formed is then the speed difference of the fast and slow stream to be larger than the respective magnetosonic wave speed. Consequently, fast shocks with an increase in the magnetic field magnitude downstream related to the fast magnetosonic wave, and slow shocks with a decrease in the magnetic field magnitude downstream related to the slow magnetosonic wave are formed. The possible combinations of forward/reverse and fast/slow result in four possible types of shocks. Figure 1.3 illustrates how the plasma parameters vary across the shock for each of these shock types.

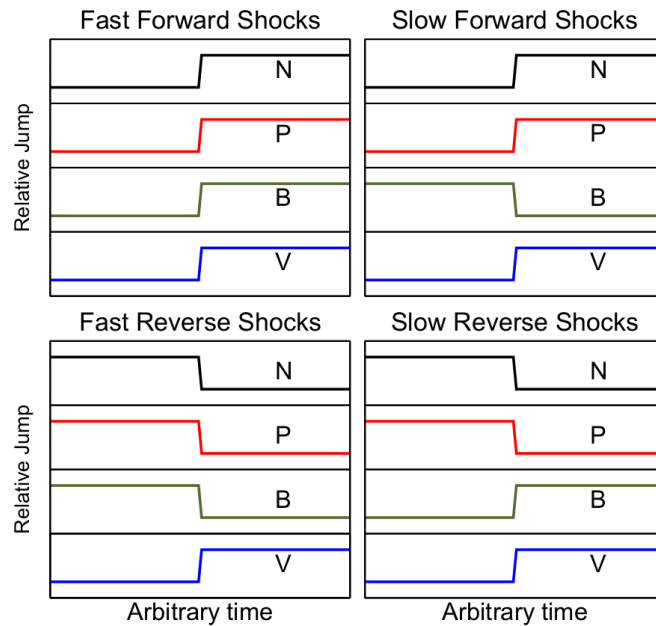


Figure 1.3: Schematic variations of the plasma number density (N), pressure (P), magnetic field magnitude (B), and flow speed (V) for all four types of interplanetary shocks. Taken from Oliveira [2017].

In interplanetary space, the fast forward shock is the most common type [Berdichevsky et al., 2000]. CIRs and CMEs (or ICMEs if they propagate through interplanetary space) are the main drivers for IP shocks. The CIR shown in Figure 1.2 has a forward shock at the outer edge of the compression region and a reverse shock at the inner edge of the compression region. Figure 1.4 depicts a typical topology of an ICME together with the shock propagating into interplanetary space. Shocks like these cause geomagnetic storms and aurorae, when reaching Earth's magnetosphere. ICMEs are responsible for the strongest geomagnetic perturbations, while CIRs typically produce only weak to moderate

disturbances.

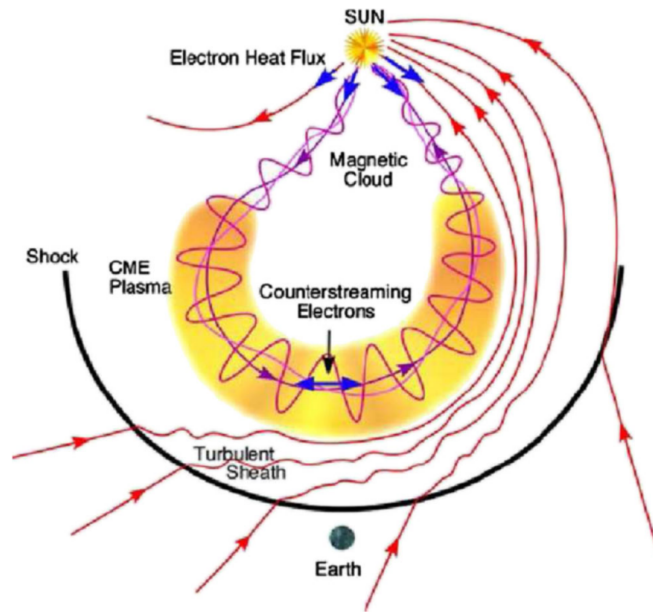


Figure 1.4: Representation of an ICME and the shock formation. Taken from Oliveira [2017].

1.2 Earth’s Magnetosphere

1.2.1 Magnetosphere Structure

IP shocks created by CMEs and CIRs are not the only shocks in the interplanetary space. For example, shocks are created around magnetised planets as well. Such a magnetic field forms an obstacle in the solar wind flow. As the solar wind is supersonic, inevitably a shock needs to form in front of the obstacle. This is called a bow shock. Due to its magnetic field, there is a bow shock in front of Earth.

Earth’s bow shock is where the solar wind drops from supersonic to subsonic speeds. While the speed decreases, there is also a compression at the shock. The plasma density, magnetic field strength, and temperature is increasing. Furthermore, the shock is not infinitesimally thin. There is a structure starting with a “foot”, followed by a “ramp” and an “overshoot”. The “ramp” is where the slowing and the compression occurs. Some particles can be reflected back into the solar wind before they move back again through the shock. These reflected particles form the “foot”. The “overshoot” comes from the deceleration of the ion flow. It is a balance act between the drop of the dynamic pressure and the increase of magnetic pressure [Zhou et al., 2020, Gedalin et al., 2023].

Behind the bow shock lies the magnetosheath. This is the region where the shocked solar wind plasma gets diverted around Earth’s magnetosphere. While initially subsonic, the solar wind accelerates again and becomes eventually supersonic once again. The majority of the magnetosheath plasma is comprised of the shocked solar wind plasma with a fraction of magnetospheric plasma as well.

Turbulences are very common in the magnetosheath, being controlled by the geometry of the magnetic field in the upstream solar wind plasma [Rakhmanova et al., 2021]. The angle between the shock normal and the direction of the IMF vector is particularly important [Wang et al., 2015, 2016]. Notable small-scale variations characterised by transient increases in the dynamic pressure, called magnetosheath jets and plasmoids, are at times present [Karlsson et al., 2015].

The magnetosheath adjoins the magnetopause, a boundary layer between the solar wind and the actual magnetosphere. The magnetopause is a relatively thin layer with a thickness of a few hundred kilometres. It is a sheet of electric current that separates regions of distinctly different magnetic fields. Current sheets are quite common in space plasma. They can be found in the magnetotail of the magnetosphere and also in the corona and heliosphere. Essentially everywhere, where two magnetised plasma regions describable by the (idealised) MHD equations interact with each other, a current sheet can be found. According to Ampère’s law, the respective current is responsible for the magnetic field jump between the two regions.

A very simplified picture of the magnetopause (Chapman-Ferraro) current formation is shown in Figure 1.5. In this picture, the magnetopause is not curved, there is no magnetic field in the solar wind and no plasma in the magnetosphere. The thermal properties of the incoming particles are also ignored. As the solar wind particles enter the boundary layer with a velocity \vec{u} , they encounter a magnetic field \vec{B} , which exerts a $\vec{u} \times \vec{B}$ Lorentz force on the particles. The oppositely charged particles will perform half a gyration in opposite directions before they leave the boundary layer again, giving rise to a current. In this case, the current sheet would have a thickness equivalent to the ion gyration radius. In reality, due to the effects of the magnetospheric plasma, the solar wind magnetic field, etc., the particle trajectories inside the boundary layer are much more complex, resulting in a much thicker current sheet, which varies under different solar wind conditions [Dunlop and Balogh, 2005, Leand and Russell, 1994]. The particles do not necessarily leave the current sheet this way either, but they may remain in the plane of the current sheet until they eventually reach its edge and are lost. The particle influx on either side of the sheet ensures its continuous existence.

The position of the magnetopause is determined by the balance between the total pressure on both sides of the boundary. The total pressure is composed of the dynamic pressure of the plasma flow, the magnetic pressure exerted by the magnetic field, and the thermal gas pressure. In the solar wind, the dynamic pressure dominates over the magnetic and thermal pressures, while in Earth’s magnetosphere, the magnetic pressure dominates over the dynamic and thermal pressures. The situation inside the magnetosheath is more complicated. However, one can roughly assume the pressure balance transition through the magnetosheath, obtaining the need for the pressure balance between the solar wind and the magnetosphere. Thus, in this very simplified picture, the subsolar magnetopause is where the solar wind dynamic pressure equals the magnetic pressure in Earth’s magnetosphere:

$$\rho_{\text{sw}} u_{\text{sw}}^2 = \frac{B_{\text{ms}}^2}{2\mu_0}, \quad (1.1)$$

where ρ_{sw} is the mass density of the solar wind plasma, u_{sw} is the solar wind

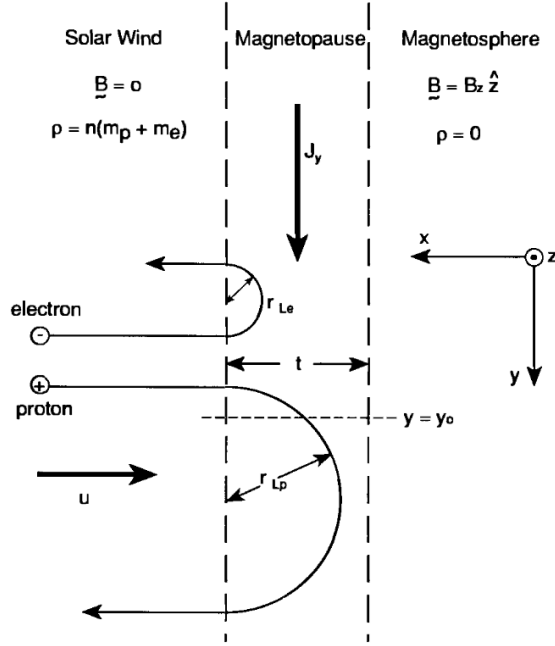


Figure 1.5: A simplified model of the magnetopause current sheet with an unmagnetised solar wind on the left and a plasma free magnetosphere on the right. The current flows downwards in the y -direction. It is carried by the collective action of solar wind particles. Each particle completes half a gyration in the magnetospheric magnetic field before returning to the magnetosheath. Taken from Kivelson and Russell [1995].

speed, B_{ms} is the magnetic field magnitude on the magnetospheric side of the magnetopause, and μ_0 is the magnetic permeability of vacuum. A more exact evaluation of the position of the magnetopause as well as the magnetopause location away from the subsolar point is a matter of more complex models [Lin et al., 2010, Liu et al., 2015], but as a first approximation, this is sufficient.

If the solar wind pressure increases, the magnetic field on the magnetospheric side of the magnetopause has to increase to maintain the pressure balance. This necessarily results to the movement of the magnetopause closer to the Earth, where Earth's magnetic field is stronger (note that it can be roughly approximated as a dipole, i.e., decreasing with a cube of a radial distance). At the same time, the Chapman-Ferraro current flowing through the magnetopause intensifies [Man et al., 2021]. This current, in line with the Biot-Savart law, cancels Earth's magnetic field outside the magnetopause and increases the magnetic field magnitude inside the magnetosphere. If the magnetopause current intensifies, the magnetic field inside the magnetosphere also increases, which can be readily measured even on Earth's surface. This effect is known as a sudden impulse (SI) or sudden storm commencement (SSC) if a geomagnetic storm follows.

Behind the magnetopause lies the actual magnetosphere. The magnetic field of Earth resembles a torus-shaped dipole field close to Earth itself with influences of higher moments than the pure dipolar field [Hulot et al., 2010]. Closer to the magnetopause, it is significantly deformed due to the interaction with the solar wind. On the dayside, the magnetic field is highly compressed by the pressure of the solar wind. The faster the wind the more the dayside magnetic field

is compressed. Closer to the north and south poles, the magnetic field lines turn nearly perpendicular to Earth’s surface and trace down to the atmosphere. These regions are called cusps and they form cone-shaped indentations in the magnetopause pattern.

On the nightside, the magnetic field is dragged out to distances of several hundreds Earth radii, depending considerably on the solar wind variations and their short-term history. This is called the magnetotail. Seen from the Sun, it has a more or less circular shape. The tail has a north lobe and a south lobe in the shapes of semicircular solenoids. The magnetic field lines in these regions connect to Earth’s magnetic poles. Field lines in the north lobe are directed towards Earth, while the southern field lines point away from Earth. The opposing magnetic fields of the two lobes require the formation of a current sheet in between them, the plasma sheet [Pilipp and Morfill, 1978]. This plasma sheet is relatively hot and dense compared to the lobes. It reaches from the dusk- to the dawnside of the magnetotail. The radius of the magnetotail is a few tens of Earth radii and it slightly increases with the distances from Earth.

A noon–midnight cross section of the magnetosphere can be seen in Figure 1.6. The x-axis points directly to the Sun, while the z-axis is perpendicular to the ecliptic of Earth’s orbit. The y-axis points out of the page. The tilt of the magnetic field axis is shown as well, causing the field to be asymmetric around the Sun-Earth line and adding further complexity to the whole system. It should be probably mentioned at this point that the magnetic dipole axis is also not aligned with the geographic rotation axis of Earth. Figure 1.6 also mentions a plasma mantle. There are the northern- and southernmost regions of the lobes, where the magnetic field lines coming from the polar region are open, but populated by a more dense plasma population than the lobes are. Open field lines do not connect to the field lines in the other hemisphere, but they connect to the IMF farther down the tail. The plasma number density in the plasma mantle is the highest close to the magnetopause, and it gradually decreases toward the lobes. Figure 1.6 further depicts the thinning of the plasma sheet at a distance of about $-115 R_E$ (Earth radii), which is marked with the term x-line. At this line magnetic reconnection occurs. Magnetic reconnection is an important mechanism for the plasma transfer between magnetic field regions, which would be impossible in the frame of an ideal MHD. This will be covered in the next section.

1.2.2 Magnetic Reconnection

In the ideal MHD theory, two plasma parcels, each tied to their own magnetic field line, would not be able to exchange particles, because of the frozen-in-flux condition. However, at least a limited particle exchange is clearly possible between the magnetosheath and the magnetosphere. Furthermore, the terrestrial magnetic field lines are sometimes connected to the solar wind magnetic field lines, as mentioned in the previous section. Such a situation cannot be described by the ideal MHD. At the border between two plasma regions, the frozen-in condition is thus violated at times. There is a mechanism that allows Earth’s magnetic field lines to connect to the solar wind magnetic field lines, thereby enabling a particle exchange along these “open” field lines. This mechanism is called magnetic reconnection (e.g., Kivelson and Russell [1995], Russell et al. [2016]).

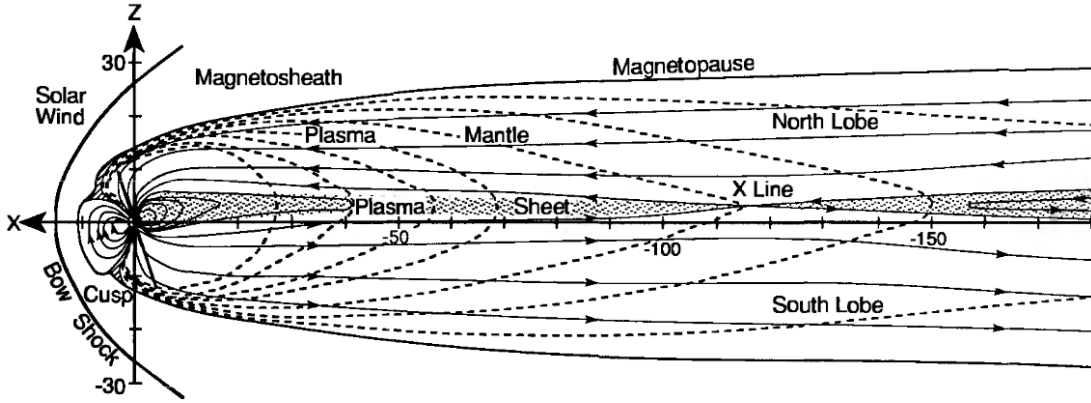


Figure 1.6: Noon–midnight cross section of Earth’s magnetosphere drawn to scale. The positive x-axis points towards the Sun, while the nightside is drawn on the negative side of the x-axis. Compressed dayside magnetic field and the cusps above the magnetic poles on the positive side of the x-axis can be seen. The dashed lines show trajectories followed by particles in the plasma mantle. For more information, see text. Taken from Pilipp and Morfill [1978].

The frozen-in condition holds as long as the magnetic Reynolds number $R_m \simeq \mu_0 \sigma u L$ is much larger than unity. Here, σ is the electrical conductivity, u is the speed of the plasma fluid, and L is the scale length of the system. In space, the scale lengths are typically very large. However, if the magnetic field magnitude and/or orientation in the two plasma regions considered is different, the corresponding characteristic scale length of the magnetic field change across the (thin) boundary can be very small (the magnetic field gradient very large). This is then the region, where the frozen-in concept can locally break down [Kivelson and Russell, 1995].

A basic description of the magnetic reconnection is achievable in 2D, assuming that the situation is independent of the third dimension. The situation is depicted in Figure 1.7. Two plasma regions with the magnetic fields of an equal magnitude but opposite directions are assumed located at the top and bottom of the figure. These are separated by a current sheet with a current flowing out of the page, which is responsible for the respective magnetic field jump. Additionally, there is an electric field on both sides in the same direction as the current. For a steady state, it stems from Faraday’s law that this electric field should be uniform. Then, as a result of an $\vec{E} \times \vec{B}$ drift, the plasma in both the top and bottom regions move towards the current sheet. The shaded area in the centre of the figure is the diffusion region, where the frozen-in condition is violated and the magnetic field reconfigures. In some sense, the magnetic field lines are “cut” and “reconnected” to different partners. This results in plasma parcels located originally on separate flux tubes to eventually occur on the same, reconnected flux tube. Considering the plasma inflow toward the diffusion from the top and bottom, there must be some plasma outflow from the diffusion region as well. This indeed occurs, as the plasma leaves the diffusion region to the left and right of the image. In the diffusion region, the magnetic field energy is converted to heat and acceleration of the plasma [Kivelson and Russell, 1995].

Magnetic reconnection was for the first time proposed as a mechanism for particle acceleration in solar flares [Giovannelli, 1947]. Indeed, magnetic reconnection

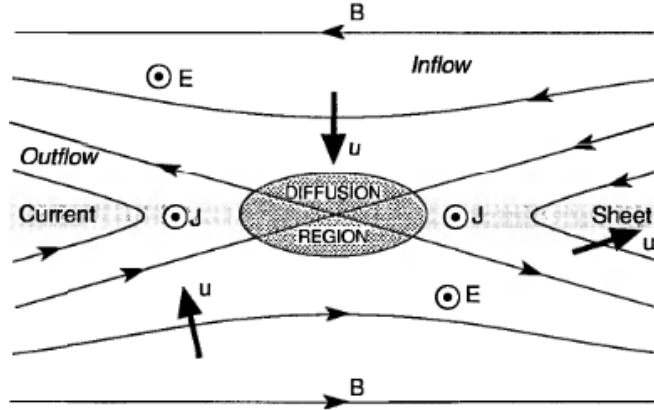


Figure 1.7: A very basic illustration of magnetic reconnection at an x-type magnetic line. The magnetic field and plasma flow inwards from the top and bottom and flow outwards to the left and right. The central shaded area corresponds to the diffusion region, where $R_m < 1$ and the ideal MHD breaks down. Taken from Kivelson and Russell [1995].

tion is a common process in solar flares, CMEs, at the magnetopause, and also in the plasma sheet in the magnetotail. The first model to describe magnetic reconnection was the Sweet-Parker model [Sweet, 1958, Parker, 1957]. In this model, the diffusion of the magnetic fields and the particle heating and acceleration were allowed only in a small region not unlike the shaded area in Figure 1.7. The problem was that the rate at which reconnection could occur in this model was very slow. Solar flares would need to grow in a matter of days instead of the observed minutes.

A magnetic reconnection model resulting in faster reconnection rates was subsequently developed by Petschek [1964]. He realised that not all plasma involved in the reconnection process needs to flow through the diffusion region. Instead, stationary shock waves are generated that are connected to the diffusion region. These shock waves reach out into the plasma, where MHD is still valid. In fact, the diffusion region can be reduced to a single point, while the shocks provide the necessary mechanism to heat and accelerate the plasma at a much larger rate than in the Sweet-Parker model. The detailed mechanism of the magnetic reconnection is still not fully understood. More recent models derive the rate at which particles are heated and accelerated on stochastic processes involving magnetic field turbulences [Lazarian and Vishniac, 1999] or a non-MHD process, called collisionless reconnection [Treumann and Baumjohann, 2013].

Reconnection at the Magnetosphere

The first to apply magnetic reconnection to the magnetosphere was Dungey [1961]. He proposed a cycle, where solar wind magnetic field lines reconnect with magnetospheric magnetic field lines on the dayside, are convected tailward, and eventually reconnect on the nightside. For this to happen, the IMF has to have a significant southward component, i.e., anti-parallel to the northward magnetic field of Earth. The magnetic field lines then undergo magnetic reconnection at the nose of the magnetosphere, so that there are two separate field lines, one connected to the north pole and the other to the south pole. The other ends of

these field lines would be connected to the interplanetary magnetic field. These new field lines are then dragged towards the nightside by the solar wind portion of the field line until they form the magnetotail. The field lines from the north and south lobe eventually meet again far down the tail and form an x-line, where they reconnect and reach a closed state again. The reconnected field line farther away from Earth is a purely interplanetary field line and it rejoins the solar wind flow farther away from the Sun and Earth.

This cycle is schematically shown in Figure 1.8, with the numbers corresponding to the temporal evolution of a given magnetic field line. It is a very simplified description, but it offers a basis which can be extended upon. A couple of years later, Dungey also proposed a picture for a northward IMF [Dungey, 1963]. In such a case, an IMF line wraps around Earth’s magnetosphere and magnetic reconnection occurs in the tail region. In fact, considering the full 3D configuration, one can see that conditions favourable for reconnection do not only occur at the nose of the magnetosphere. For a purely southward IMF, magnetic reconnection can appear essentially all the way from the dusk- to the dawnside. A so-called extended x-line is formed. Moreover, the IMF does not have to be purely southward for the dayside reconnection to occur. It is sufficient if the IMF has a component anti-parallel to Earth’s magnetic field. As a consequence, magnetic reconnection can occur at pretty much every point or line across Earth’s magnetic field [Trattner et al., 2021]. A model of magnetopause reconnection locations has been eventually developed. It aims to predict the likelihood of reconnection sites all over the magnetopause based on the level of parallelism of the IMF and Earth’s magnetic field lines. This model is called the Maximum Magnetic Shear model [Trattner et al., 2007].

1.2.3 Inner Magnetosphere

A depiction of the magnetospheric plasma environment can be seen in Figure 1.9. The plasma mantle and tail lobes were mentioned before. Together with the Plasma-Sheet Boundary Layer (PSBL) and the plasma sheet, they form the major plasma regions in the magnetotail. While the tail lobe densities are very small ($\approx 0.1 \text{ cm}^{-3}$) and the energies are quite low (less than a few tens of keV), the plasma sheet is formed by relatively hot particles with densities of about one order of magnitude higher. The PSBL can be seen as a transition region between the plasma sheet and the lobes. The tail lobe plasma is mostly comprised of ionospheric particles, while the plasma sheet consists of a mixture of ionospheric and solar wind particles. At the x-line, seen on the far right of Figure 1.9, magnetic reconnection occurs occasionally between the field lines of the north and south tail lobes. On the side that faces away from Earth, the outflow is antisunward, and the plasma gets expelled from the magnetosphere into the solar wind. On the opposite side, towards Earth, particles flow into the plasma sheet. These particles move along the field lines to high latitudes close to Earth, where they are either reflected by the magnetic field or interact with the atmosphere. In active times, this process is believed to be responsible for the occurrence of substorms and the auroral lights. The plasma sheet has a well defined inner edge on the duskside, but a less distinct boundary on the dawnside [Vasyliunas, 1968].

The Low Latitude Boundary Layer (LLBL) is a region that covers the entire

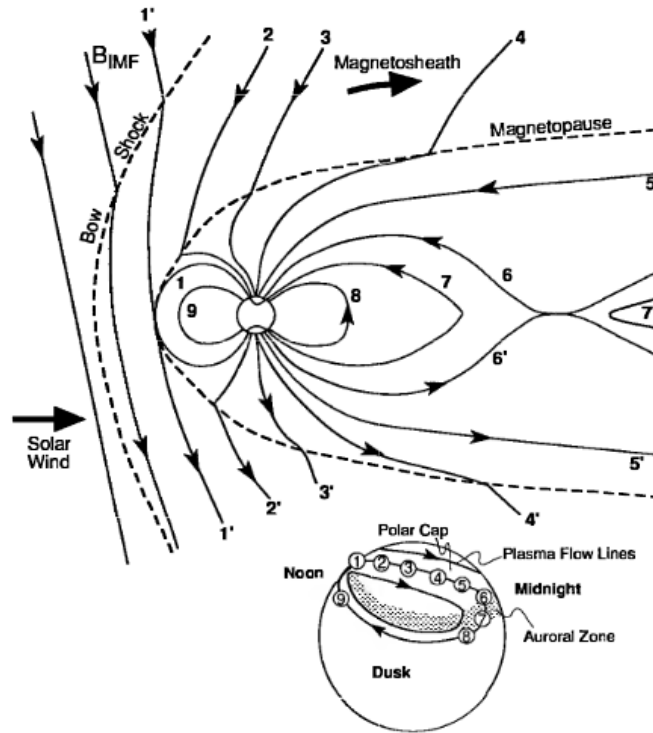


Figure 1.8: The Dungey cycle, describing the flow of plasma and magnetic field line convection within the magnetosphere driven by magnetic reconnection. The evolution of a given magnetic field line from Earth starts on the dayside (marked as 1 and 1'). Then, following the numbering, the newly reconnected field lines move to the nightside to eventually reconnect, in the far tail (6 and 6'). Taken from Kivelson and Russell [1995].

area along the magnetopause at lower latitudes (e.g., Eastman et al. [1976]). The plasma in this layer consists of a mixture of magnetosheath and magnetospheric plasma. It is still debated if the field lines in the LLBL are open field lines or a mix of open and closed field lines [Song and Russell, 1992, Paschmann et al., 1993, Fuselier et al., 1991, Le et al., 1996]. The formation of the LLBL probably cannot be explained by a single mechanism, but rather by a variety of mechanisms, such as reconnection, surface waves, diffusion, etc. The dayside LLBL is supplied by magnetosheath plasma via subsolar reconnection during southward IMF, whereas the tail is supplied through reconnection tailward of the cusps when the IMF is northward. The thickness of the LLBL is similar on the dayside and on the flanks, but the exact thickness depends on the particular state of the IMF [Němeček et al., 2003]. Rossolenko et al. [2008] reported, that the thickness of the LLBL also depends on solar wind conditions.

Closer to Earth, where the distortion of Earth's magnetic field due to the interaction with the solar wind is quite negligible, and the magnetic field can be to the first order approximated by a dipole. Two significant regions occur within the inner magnetosphere the Van Allen belts and the plasmasphere [Pierrard et al., 2009, Singh et al., 2011]. They may occupy roughly the same space at times. While the plasmasphere consists of primarily cold particles (eV range), particles in the radiation belts have energies from keV to MeV. The radiation belts will be treated in depth in the next section.

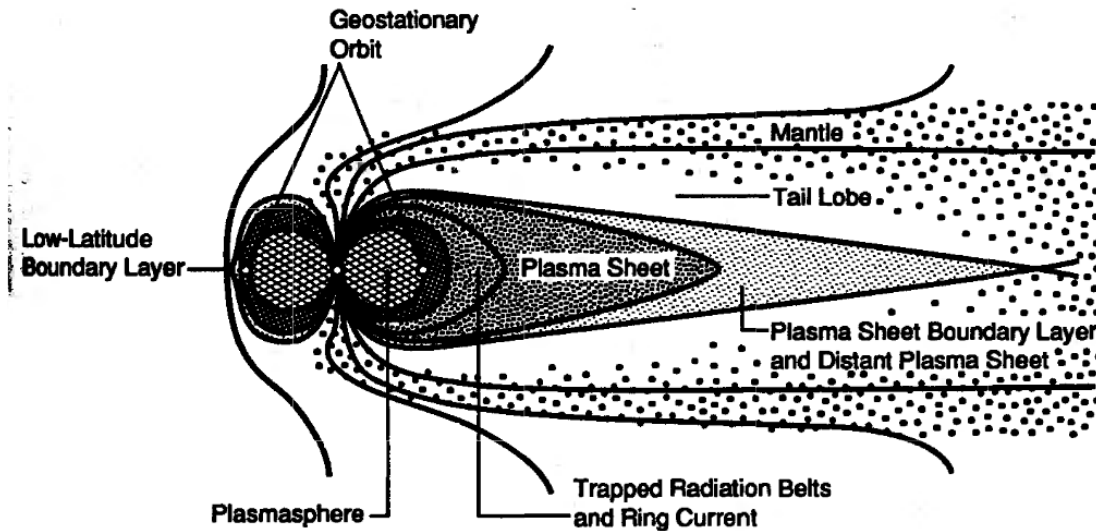


Figure 1.9: Noon-midnight view of the plasma regions in the inner magnetosphere. The plasmasphere and the radiation belts occupy more or less the same region. Taken from Kivelson and Russell [1995].

The plasmasphere is supplied with charged particles from the ionosphere, i.e., from the upper part of the atmosphere, where radiation from the Sun and, to a lesser extent, precipitating energetic particles ionise neutral particles. The latter process is more relevant at higher latitudes and larger zenith angles, where the precipitating energetic particle fluxes are larger and the solar ionising radiation is weaker. The magnetosphere-ionosphere coupling is a very complex system with various linear and non-linear mechanisms providing the exchange of mass, energy, and momentum between the two regions. In the polar region, the key elements for the coupling are field aligned currents and ultra-low frequency (ULF) shear Alfvén waves (e.g., Mishin and Streltsov [2022]).

The plasmasphere has a sharp boundary called the plasmopause [Laakso and Jarva, 2001, Moldwin et al., 2003]. Its location is given by the topology of electric field equipotentials inside the magnetosphere, i. e., by the combined effect of the convection and corotation electric fields. The reason is that, due to their comparatively low energy, the motions of charged particles within the plasmasphere are for the most part governed by the $\vec{E} \times \vec{B}$ drift. A typical radial distance of the plasmopause in the equatorial region is about $4 R_E$. In extended quiet times, the plasmasphere can reach even beyond the geostationary orbit. During geomagnetically active times, the plasmopause occurs closer to Earth, as the region with the closed topology of the equipotentials shrinks considerably. This can happen relatively quickly in a matter of hours. The plasma at the outer layers of the plasmasphere is then no more trapped and escapes the system. The plasmasphere becomes smaller. When the geomagnetic activity and the convection electric field decrease again, the region with the closed topology of the equipotentials extends and gets replenished by new plasma particles originating in the ionosphere.

Current Systems

With the presence of charged particles in a complex system of magnetic and electric fields, the existence of currents follows quite naturally. Two principal

currents were already described in Section 1.2.1 and in this section, the magnetopause Chapman-Ferraro current and the current sheet in the tail. However, these are not the only ones. Other currents are present and their complex system results in the creation of the corresponding magnetic field, the so-called external magnetic field. Under the influence of the ever-varying solar wind, this system is very dynamic and the respective geomagnetic disturbances are readily detectable even on the ground. Here, a short overview of the most important currents shall be given [Ganushkina et al., 2018]. An overview of the here mentioned currents can be viewed in Figure 1.10.

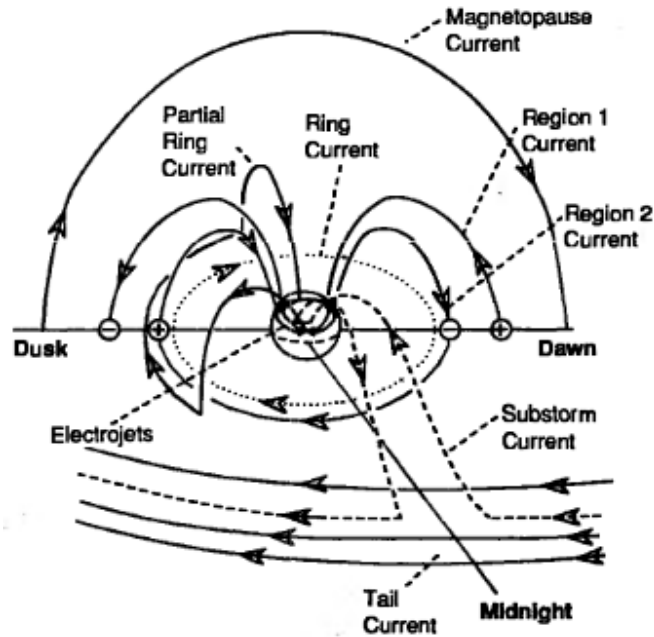


Figure 1.10: Rough schematic representation of the currents in the magnetosphere. See text for explanation. Taken from Kivelson and Russell [1995].

The magnetopause current sheet is also called the Chapman-Ferraro currents [Chapman and Ferraro, 1931]. The respective current flow through the subsolar magnetopause, oriented from the dawn to dusk, has been already mentioned. The Chapman-Ferraro currents cancel the terrestrial magnetic field outside the magnetosphere and, at the same time, enhance the magnetic field just inside the magnetosphere. They thus considerably influence the balance between the solar wind dynamic pressure and the magnetospheric magnetic pressure. The current sheet in the tail is a part of the plasma sheet. In the central plasma sheet, the current flows towards dawn from one side of the magnetotail to the other. This current is ultimately responsible for the sudden change of the magnetic field orientation in the tail from the away-from-the-Earth orientation in the south to toward-the-Earth orientation in the north. Instabilities in that region, particularly an enhanced magnetic reconnection, lead to magnetospheric substorms (e.g., Hones [1979], Baker et al. [1996]). The return current flows duskwards along the magnetopause curvature on both the north and south side.

A set of field-aligned currents was predicted by Birkeland and Muir [1908] and later confirmed by satellite measurements [Iijima and Potemra, 1976, Zmuda et al., 1966]. These currents were later separated into Region 1 and Region 2

currents. Region 1 currents are flowing upwards out of the ionosphere on the duskside, then dawnwards near or along the magnetopause and back into the ionosphere on the dawnside. Region 2 currents occur at lower latitudes and move generally in opposite directions to Region 1 currents. Inside the ionosphere, in the polar regions, these currents flow perpendicular to the magnetic field and along the electric field. They are called auroral electrojets. Some Region 1 currents flow along open field lines, where the currents are connected to the dayside magnetopause. Other Region 1 currents lie on closed magnetic field lines where they connect to the plasma sheet, boundary layer, and nightside magnetopause (e.g., Ohtani and Uozumi [2014], Xing et al. [2009]). These currents play an important role in the magnetosphere–ionosphere coupling [Siscoe et al., 1991]. Region 1 and 2 currents that connect to the tail current during substorm events are also called substorm currents [Kepko et al., 2015].

In the equatorial region, the existence of a westward-flowing ring current had already been predicted in early studies of magnetospheric physics [Schmidt, 1917, Störmer, 1912]. The ring current is particularly important during geomagnetic storms and for their classification [Akasofu and Chapman, 1961, Kamide, 1974]. A series of processes during geomagnetic storms enhances the ring current, which, in turn, decreases the magnetic field magnitude at Earth’s surface. More complicated equatorial current structure, including the partial ring current and occasional currents flowing westward, was eventually revealed [De Michelis et al., 1999]. In the dayside region, closer to the magnetopause, the current may possibly split into two branches, following the presence of the two magnetic field minima. No such current splitting is expected to occur on the nightside, as there is only a single minimum present.

When the magnetosphere is highly disturbed, the ring current becomes strongly asymmetric. In this situation, partial ring currents can form on the nightside [Alfvén, 1950, Egeland and Burke, 2012]. These currents only flow partially around the Earth near the equatorial plane, being subsequently connected to the ionosphere through field aligned currents. Note that there are more currents that might appear in the magnetosphere during geomagnetically disturbed periods. These form a very complex and dynamic system, which is beyond the scope of this thesis.

1.3 Radiation Belts

The radiation belts, also called Van Allen belts, are two regions of trapped energetic particles around Earth, shaped like toroids [Van Allen et al., 1959]. The two regions are called the inner and the outer belt separated by a slot region. The inner belt lies roughly at radial distances between 1.03 Earth radii and 2 Earth radii. It is comprised of protons with energies of few MeVs up to several hundred MeV (e.g., Albert et al. [1998], Selesnick et al. [2016] and electrons of hundreds of keV. The outer belt lies somewhere between 3 and 10 Earth radii and it contains mostly electrons between 0.1 and 10 MeV. It is subject to widely varying electron fluxes (e.g., Reeves et al. [2003], Baker et al. [2014b], Turner et al. [2014]). The slot region stretches out between about 2 and 3 Earth radii and shows greatly reduced electron fluxes for energies above about 0.5 MeV [Baker et al., 2004]. Energetic ions of helium, oxygen, and heavier elements are also present to a much

lesser extent [Kovtyukh, 2018]. Note that the numbers are rather vague and at times overlapping, as the radiation belts respond dynamically to the variable solar wind and the corresponding magnetospheric disturbances. This is especially true for the outer belt. It is significantly more responsive to solar wind variations, while the inner belt is relatively stable and mostly reacts only to the most severe activities. Also, the aforementioned structure comprising the two radiation belts is subject to change. The slot region may be temporarily (\approx few days) filled by energetic particles and effectively disappear [Nikitina and Trichtchenko, 2021] or the outer belt may split into two, resulting in a three-belt structure being formed for a period of a few weeks [Baker et al., 2013].

1.3.1 Particle Motions and Adiabatic Invariants

Energetic particles trapped in the radiation belts execute three basic motions: gyration, bounce motion, and azimuthal drift motion around the Earth. The gyration is the cyclotron motion around the magnetic field line as a result of the Lorentz force $\vec{F}_L = q(\vec{v} \times \vec{B})$, where q and \vec{v} are, respectively, the particle charge and velocity, and \vec{B} is the ambient magnetic field. The radius of this cyclotron motion (gyroradius or Larmor radius) r_g is given by

$$r_g = \frac{mv_{\perp}}{|q|B}, \quad (1.2)$$

and the gyrofrequency ω_g is given by

$$\omega_g = \frac{|q|B}{m}, \quad (1.3)$$

with m being the mass of the particle, and v_{\perp} being the particle velocity perpendicular to the ambient magnetic field. For ions, the gyroradius is significantly larger than for electrons, because of their much larger mass. Moreover, the sense of gyration depends on the particle charge, i.e., the negatively charged electrons gyrate in an opposite sense than the positively charged ions.

A particle gyrating around a magnetic field line can be assigned a magnetic moment μ :

$$\mu = \frac{mv_{\perp}^2}{2B} = \frac{W_{\text{kin}\perp}}{B}, \quad (1.4)$$

where $W_{\text{kin}\perp}$ is the kinetic energy of the particle. The magnetic moment μ is also referred to as the *first adiabatic invariant*. In the theory of adiabatic invariants [Landau and Lifshitz, 1976] the closed integral:

$$\oint \vec{p} \, d\vec{q} \quad (1.5)$$

is conserved under slow changes in a system that demonstrates periodic motion in the spatial coordinate \vec{q} (not to be confused with the charge q), and where \vec{p} is the canonical momentum:

$$\vec{p} = m\vec{v} + q\vec{A}, \quad (1.6)$$

with \vec{A} being the magnetic vector potential. It can be shown that Equation 1.5 leads to the magnetic moment in Equation 1.4. The magnetic moment μ of a particle is conserved as long as changes in the magnetic field are much slower than the duration of the gyration period of that particle.

For a particle moving along an Earth magnetic field with a parallel velocity v_{\parallel} , B is weakest at the geomagnetic equator. As the particle moves closer to the polar region, B increases. Considering that μ is to remain constant, $W_{\text{kin}\perp}$ has to increase as well. Because the total kinetic energy in a static magnetic field does not change ($W_{\text{kin}\perp} + W_{\text{kin}\parallel} = \text{const.}$), $W_{\text{kin}\parallel}$, and therefore v_{\parallel} , must eventually go to zero for sufficiently large B . The particle will be thus stopped at a critical magnetic field strength B_m , and will start to move in the opposite direction. This particle reflection is called magnetic mirroring. Energetic charged particles in Earth's radiation belts are trapped by Earth's magnetic field in this way, and they periodically bounce between northern and southern reflection points.

As the period of the bounce motion is significant longer than the gyration period of the particle, μ can be assumed to be constant and the magnetic field magnitude at the mirror point B_m can be determined via

$$B_m = \frac{W}{\mu}, \quad (1.7)$$

where W is the total kinetic energy of the particle. Using this relation, and considering that any periodic motion can be associated with a respective adiabatic invariant, the *second adiabatic invariant* J can be derived by relating Equation 1.5 to the particle motion along a magnetic field line:

$$J = \oint \vec{p}_{\parallel} ds = \sqrt{2m\mu} \int_{m_1}^{m_2} \sqrt{B_m - B(s)} ds, \quad (1.8)$$

where s is the distance along the magnetic field line, and m_1 and m_2 are the locations of the mirror points. J should be conserved if magnetic field changes are very slow compared to the bounce period of the particle. Note that the integral in J does not depend on the energy of the particle, but only on the mirror points and the magnetic field magnitude profile along a given magnetic field line.

The third motion is the precession around the Earth, which is the drift perpendicular to the magnetic field. The drift is a result of an $\vec{E} \times \vec{B}$ drift, the gradient drift, the curvature drift. The gradient drift is the result of the charged particle gyrating in a non-uniform magnetic field. The curvature of Earth's magnetic field lines causes a drift that is perpendicular to the local magnetic field line and the local direction of the curvature. The gradient and curvature drift point in the same azimuthal direction and depends on the sign of the particle charge. Positively charged particles drift westwards and negatively charged particles drift eastwards. The $\vec{E} \times \vec{B}$ drift does not depend on the charge or the energy of the

particle, but the gradient and curvature drift do. At high enough particle energies (\simeq few hundred keV), the latter two drifts dominate over the $\vec{E} \times \vec{B}$ drift and define direction and drift period around Earth. It is this azimuthal drift of charged particles in Earth's magnetic field, which is responsible for the formation of the ring current around Earth.

Considering that the motion of the particles is a periodic motion around the Earth, an adiabatic invariant can be assigned to it. The gyration and bounce motion in the Integral 1.5 for the drift motion give zero, only the drift momentum $p_\Phi = mv_\Phi + qA_\Phi$ for the azimuthal motion of the bounce-averaged centre remains. The drift velocity v_Φ is rather small compared to the second term in the closed integral from the Integral 1.5 and can be written as:

$$\oint p_\Phi ds \simeq q \oint A_\Phi ds = q\Phi, \quad (1.9)$$

where the integral is taken along the path of the guiding centre (bounced averaged) s and the *third adiabatic invariant* Φ is thus the total magnetic flux enclosed by the drift shell of the particle. A more detailed derivation can be found in, e.g, Kivelson and Russell [1995] or Fitzpatrick [2021]. The three particle motions are exemplarily presented in Figure 1.11.

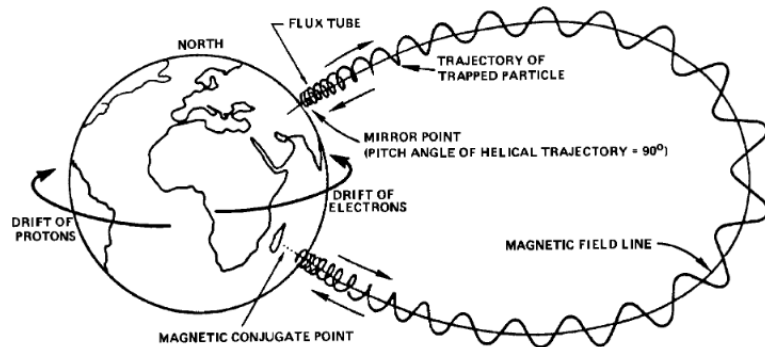


Figure 1.11: Exemplary presentation of the three basic particle motions executed by particles trapped in the radiation belts: Gyration, bounce motion in between mirror points, and drift motion around the Earth. Taken from [Gruntman, 1997].

If all the three adiabatic invariants μ , J and Φ remained exactly conserved, particles trapped in Earth's magnetic field would be contained in the radiation belts forever. In reality, the adiabatic invariants are violated by various short-period changes of the magnetic field (most importantly, plasma waves). The most easy to violate is the third adiabatic invariant, whose relevant time scales are the largest. Overall, the lifetimes of the trapped particles depend, among others, on the particle equatorial distance and energy, ranging from minutes to many years [Wentworth et al., 1959, Claudepierre et al., 2020].

To describe the movement of a particle in a dipole field, let alone in the distorted magnetic field of Earth, in Cartesian coordinates is very impractical. The desire to find more useful, but still physical coordinates, led to the definition of the magnetic shell parameter L [McIlwain, 1961]. This parameter describes the drift shell of a trapped particle in Earth's magnetic field. Starting with the integral I from Equation 1.8:

$$I = \int_{m_1}^{m_2} \sqrt{1 - \frac{B(s)}{B_m}} ds = \text{const.}, \quad (1.10)$$

which is valid in the absence of electric fields, McIlwain found an expression for $I = I(L, B_m)$, initially for a pure dipole field, where L is simply the distance from the geomagnetic centre to the equatorial point of a particle’s drift shell (measured in R_E). The quantity I , however, has no simple physical analogy. He argued that this relation can be reversed, so that $L = L(I, B_m)$:

$$\frac{L^3 B_m}{B_e} = F \left(\frac{I^3 B_m}{R_E^3 B_e} \right), \quad (1.11)$$

where B_e is the value of the magnetic field at the geomagnetic equator, R_E the Earth radius, and F a numerical function. Instead of calculating L from a dipole field, McIlwain used the *real* magnetic field values to compute L [McIlwain, 1966]. This is called the “McIlwain L -value” of a particle, its field line, and drift shell. It takes into account the real multipole geomagnetic field, but not external asymmetric and time-variable sources of the magnetospheric field [Roederer and Lejosne, 2018]. This led Roederer [1967] to consider the relationship between L and the third adiabatic invariant Φ of a particle in a pure dipole magnetic field:

$$\Phi = \frac{2\pi B_e R_E^2}{L}, \quad (1.12)$$

and eventually to define, following McIlwain’s strategy, an adiabatically invariant quantity L^* (L-star):

$$L^* = \frac{2\pi B_e R_E^2}{\Phi}. \quad (1.13)$$

However, here, Φ is not computed for a dipole, but the third invariant for a particle of a given pitch angle α (the angle between the magnetic field vector and the particle’s velocity vector) at a given place and time. It is not so much a point in space as it is a property of a stably trapped particle. It also takes into account shell splitting, where particles with different pitch angles do not remain on the same field line at other longitudes. Further suggestions for the definition of McIlwain L were made to improve its accuracy [Pilchowski et al., 2010].

The displacement of the magnetic dipole axis compared to geographic axis is primarily responsible for the magnetic field above the south Atlantic ocean to be weaker than elsewhere. As a result, the trapped particles come closer to the geographic centre of Earth, and create a region roughly between Brazil and the African continent with higher radiation intensity at lower altitudes. This region is called the South Atlantic Anomaly (SAA) [Vernov et al., 1967].

1.3.2 Particle Dynamics

As already mentioned in the former section, the adiabatic invariants are no “pure” invariants, but they can be violated. In the highly dynamic magnetospheric environment, there are a number of mechanisms that constantly remove particles

from the radiation belts. As the belts are persistent, there are obviously sources that supply them with new particles. Furthermore, the radiation belt particles have energies higher than observed in the solar wind or elsewhere in the magnetosphere [Kanekal and Miyoshi, 2021, Ripoll et al., 2020]. This means, particles have to be accelerated in some way. The particle flux variations are most striking during times of intense geomagnetic activity, when mechanisms for particle injection, energisation, and loss are the strongest. However, some radiation belt dynamics have also been observed during quiet times, e.g., through the interaction of electromagnetic ion cyclotron (EMIC) waves with radiation belt particles [Greeley et al., 2024].

Particle Sources

One possible source of radiation belt particles is obviously the solar wind. It was already discussed how the solar wind can supply particles to the magnetosphere through the magnetic reconnection. These particles can be either directly injected into the radiation belts [Schiller et al., 2014, Foster et al., 2015, Kanekal et al., 2016] or they are inserted into the magnetotail. From the magnetotail, particles can be injected and accelerated by substorm events into the radiation belts. The solar wind particle and energy entrance to the magnetosphere depends heavily on the solar wind conditions and it is most intense during periods with large negative IMF B_z (< -10 nT) and a duskward-electric field of > 5 mVm⁻¹ over time periods larger than 3 h [Gonzalez and Tsurutani, 1987]. These intense periods are often associated with IP shock arrivals and they are called geomagnetic storms [Jurac et al., 2002].

The other significant source of radiation belt particles comes from the cosmic ray albedo neutron decay (CRAND) [Selesnick et al., 2013, 2014]. Neutrons are produced by the interaction of galactic cosmic rays (GCR) with Earth’s atmosphere. Some of those neutrons reach the lower Earth orbit and decay into protons. This is the predominant source of inner radiation belt protons ($L \leq 1.3$). Other sources for protons are the decay of solar neutrons [Ifedili, 1997] and the radial diffusion of protons from the outer belt to the inner belt probably injected during solar events [Fälthammar, 1966, Nakada and Mead, 1965].

Particle Energization

One of the most important energisation processes is radial diffusion [Lejosne and Kollmann, 2020]. This is caused by magnetic and electric field perturbations [Fälthammar, 1965], which result in the violation of the third adiabatic invariant, while the first and the second adiabatic invariants remain conserved. The particles move radially inwards or outwards, to a different L-shell. The particles which move inwards experience a larger magnetic field. As the first adiabatic invariant is still conserved, the particles are accelerated in the direction perpendicular to the ambient magnetic field. Radial diffusion is considerably sped up by the enhanced ULF wave activity [Elkington et al., 1999, Shprits et al., 2017, Su et al., 2015]. Moreover, the conservation of the second adiabatic invariant results in the particle acceleration in the direction parallel to the ambient magnetic field. The process of radial diffusion slows down considerably closer to Earth, and particle loss mechanisms are becoming predominant. An impenetrable barrier for relativistic

electrons has been found at around $L = 2.8$ [Baker et al., 2014a]. The exact nature of the barrier is not yet fully understood [Foster et al., 2016, Ozeke et al., 2018].

Another important mechanism for the particle acceleration is through wave-particle interactions [Baker, 2021]. Two different processes are arguably most important: First, drift resonance between drifting particles and MHD fast mode waves, and second, cyclotron resonance between gyrating particles and Whistler mode/magnetosonic mode waves [Kanekal and Miyoshi, 2021]. The respective waves can originate in the magnetosphere due to anisotropies of energetic electrons and protons [Thorne et al., 2016], and they can propagate over considerable distances from the source region [Bortnik et al., 2009]. Whistler mode waves have been shown to accelerate electrons to MeV energies in the outer belt [Thorne et al., 2013, Fennell et al., 2014, Kurita et al., 2018].

Particle Losses

Looking back to Section 1.3.1, it is possible to imagine that a mirror point lies inside Earth’s atmosphere (below ≈ 100 km altitude). Radiation belt particles that reach the atmosphere will lose energy and get scattered through collisions or charge exchange and are lost from the radiation belts. For a particle to move that close to Earth, its equatorial pitch angle α_0 must be sufficiently small. The condition can be written as

$$\sin \alpha_0 < \sqrt{\frac{B_0}{B_i}}, \quad (1.14)$$

where B_0 is the magnetic field magnitude at the equator and B_i is the magnetic field magnitude on that particular field line at collisional atmospheric altitudes. This equation describes geometrically a cone, which is called the loss cone. The size of the loss cone is a monotonically decreasing function of L-shell, and for $L \gtrsim 3$ its size is only a few degrees. This means that, in case of the conservation of the first adiabatic invariant, only a small fraction of the particles would be lost.

However, the first adiabatic invariant may be violated due to wave-particle interactions, resulting in pitch angle scattering. This represents an important process to cause the loss of relativistic electrons [Miyoshi et al., 2015, Kurita et al., 2018, Miyoshi et al., 2020]. It also means that plasma waves do not only accelerate particles, but they are also responsible for their loss mechanisms [Shprits et al., 2006, Su et al., 2015]. It has been shown that the both EMIC and Whistler-mode waves cause the particle precipitation [Millan and Thorne, 2007, Usanova et al., 2014, Blum et al., 2019]. Plasmaspheric hiss waves are of particular importance, as they induce pitch angle scattering of MeV electrons and are responsible for the formation of the slot region [Lyons et al., 1972, Lyons and Thorne, 1973, Meredith et al., 2007, Zhao et al., 2019].

Another important mechanism of the particle loss from the radiation belts is the magnetopause shadowing. When, for example, a ICME compresses the magnetosphere, the magnetopause moves inwards. Particles, that were previously on closed drift shells, may not be on the closed drift shells anymore, and they may

be even outside the magnetopause. These particles are not trapped in Earth's magnetic field anymore, and they escape the system. In a similar manner, the radial diffusion also contributes to the particle loss, when the diffusion is outward. Particles are decelerated, because they move to a region with a weaker magnetic field. Moreover, when their L-shell increases sufficiently, they can leave the closed drift shells, and eventually reach the magnetopause, and leave the magnetosphere [Turner et al., 2012].

A process that mainly concerns protons (due to their larger mass and, thus, larger gyroradius) is related to the breakdown of the first adiabatic invariant. This happens when the relatively large gyroradius of an energetic proton becomes comparable to the curvature of the magnetic field and the motion of the energetic proton cannot be considered adiabatic anymore. This process is called magnetic field line curvature scattering or μ scattering [Tu et al., 2014].

1.3.3 Electron Populations

Electrons in the radiation belts can be sorted into inner radiation belt electrons and to four different energy ranges of the outer belt electrons. The precise energy ranges for the outer belt electrons are not quite clear and vary among different studies. The lowest energy population is the source population in the range of a few tens of keV to about 200 keV. These electrons originate from substorm injections and large-scale magnetospheric convections. The next population of electrons is the seed population with up to several hundred keVs. Same as the source population, they are produced by substorm injections and by global convection. The names source and seed population stem from the observation that source electrons provide a source of free energy to whistler-mode chorus waves that interact with the seed population and further energise them up to relativistic energies [Jaynes et al., 2015]. Electrons in the range of 500 keV to 2 MeV are relativistic and called the core population. Electrons of even higher energies are called ultra-relativistic [Koskinen and Kilpua, 2022].

1.4 Geomagnetic Storms and Storm Indices

Throughout this chapter, substorms and geomagnetic storms have been mentioned several times. Geomagnetic storms occur as a direct consequence of IP shock arrivals at the magnetopause. Disturbances throughout the magnetosphere occur and are a major concern for satellites and astronauts alike. Strong geomagnetic storms can even affect power grids on the surface of Earth, mainly on the higher latitudes. These storms usually last for a couple of days. Substorms are related to instabilities in the plasma sheet and occur more often than geomagnetic storms and last only a few hours. They occur primarily over the polar regions and are the cause for auroral lights.

Both, geomagnetic storms and substorms, cause depressions in the magnetic field on Earth's surface through enhanced currents in the magnetosphere system. Geomagnetic storms are related with an increased ring current and magnetopause currents, while substorms are related to currents in the ionosphere at high latitudes. The respective variations in the magnetic field are routinely measured by magnetometers on the surface of Earth. Based on these measurements, so-called

geomagnetic indices are derived to provide simple single-number characterization of a particular current system strength. These indices are used to monitor changes in the magnetospheric currents, to classify the level of geomagnetic activity, and to provide a simple parametrisation for various empirical models of the magnetosphere. There is quite a large number of indices derived in slightly different ways and with different time resolutions, each serving its own purpose and focusing on slightly different effects and/or being derived under different historical circumstances [Menvielle et al., 2011]. Here, only a few are selected.

The most commonly used index to classify geomagnetic storms is the Disturbance Storm Time (Dst) index [Sugiura et al., 1991]. The index is derived from a network of low latitude geomagnetic observatories that measure horizontal magnetic variations in the Earth magnetic field. The Dst index is determined every hour as the average difference between the current measurements and a quiet-time reference. Considering that the enhanced ring current during geomagnetic storms decreases the horizontal magnetic field magnitude on the ground, the value of the Dst index is the negative change of the magnetic field in units of nT. The classification into different levels of storm intensity is listed in Table 1.1.

Table 1.1: Classification of geomagnetic storms according to the Dst index.

Storm class	Dst range [nT]
quiet-minor	> -50
moderate	$[-50, -100]$
intense	< -100
superintense	< -200

The Dst index assumes an axially symmetric disturbance field (the ring current magnitude independent of local time), which is generally not the case. Therefore, a symmetric (SYM) and an asymmetric (ASY) disturbance index were introduced. They are derived from the horizontal magnetic field component H (directed positive towards the northern magnetic pole)(ASY-H, SYM-H) and orthogonal (East-West) direction D (ASY-D, SYM-D) at a time resolution of 1 minute. SYM-H is essentially the same as the Dst index, but with a higher resolution, based on measurements at different stations, and using a slightly different coordinate system [Iyemori et al., 2000].

The Auroral Electrojet (AE) index was originally introduced as a measure of global electrojet activity in the auroral zone [Davis and Sugiura, 1966]. The H magnetic field component is measured at twelve stations near the auroral zone and the data is superimposed. Then, the largest and smallest values are selected and defined as the AU and AL indices (U – upper, L – lower). The AE index is the difference from these two values. The average of AU and AL is the AO index. The four indices together are referred to as AE indices. The time resolution for these indices is one hour. They are typically used in relation to substorms. The AE index was found to be correlated to the ASY-H index [Borojev and Vasiliev, 2020].

The causes of geomagnetic storms have been already thoroughly discussed in this chapter. Figure 1.12 shows a classic storm signature as recorded in the Dst index. The storm often begins with a sudden increase in Dst, which is called a sudden storm commencement (SSC), which may last from a few hours up to a

day. This is followed by a rapid decrease in Dst. This decrease is associated with the particle injection into the radiation belts and, consequently, an increase in the ring current. This is the main phase of a geomagnetic storm, and it can last up to a day. The last phase is the recovery phase, where the ring current relaxes and particles are gradually lost from the radiation belts. This phase lasts several days.

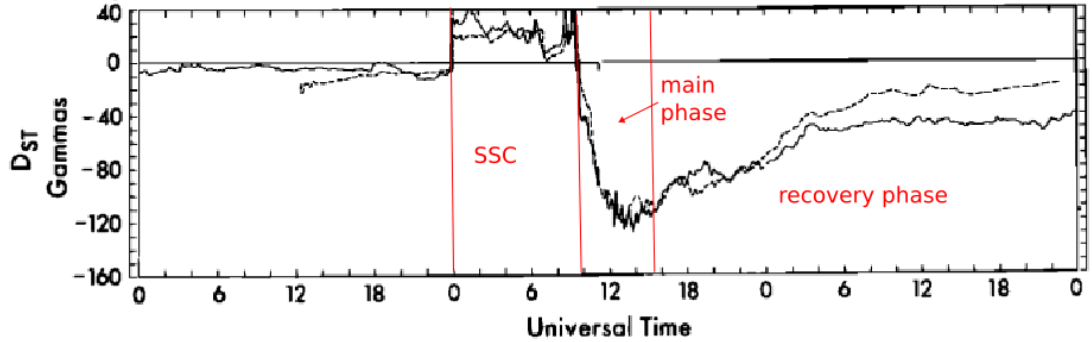


Figure 1.12: A typical geomagnetic storm as seen by the Dst index. Taken from Burton et al. [1975]. The red vertical lines and text were added to show the three phases of the storm.

The sudden increase at the start of the SSC can often be associated with the arrival of an IP shock. The SSC itself corresponds to the sheath region that follows the shock and precedes the ejecta, the actual magnetic flux rope of an ICME (see Figure 1.4), which is related to the main phase of the storm (e.g., Kalliokoski et al. [2020]). The arrivals of the shock, sheath, and ejecta have distinct magnetospheric impacts caused by distinct solar wind properties (e.g., Kilpua et al. [2017]). Several studies reported a prompt acceleration of relativistic electrons to higher energies within 20 minutes of the shock arrival (e.g., Foster et al. [2016], Kanekal and Miyoshi [2021]). The piston-like compression of the magnetopause causes a dawnward-duskward bipolar electric variation and subsequent ULF wave processes, responsible for the electron energy increase. A statistical survey by Schiller et al. [2016] showed that 25% of IP shocks produce these shock-induced enhancements at $L < 5$, while 14% result in depletion of relativistic electrons at $L > 5$. They also found that these energy enhancements occur preferably on the duskside and depend on the shock Mach number, although not exclusively. They conclude that the conditions inside the magnetosphere at the time of the shock arrival (e.g., the availability of an electron population that can be accelerated) may play a role in the occurrence probability.

A sudden drop-out of electron fluxes (> 300 keV) immediately after the IP shock arrival, associated with repeated drop-out and recovery signatures, was reported by Hao et al. [2016]. This phenomenon was dubbed “electron drop-out echoes”. Liu et al. [2017] showed that the initial drop-outs related to IP shock arrivals occur mostly on the duskside. The periodically reappearing drop-outs could be related to the drift periods of the electrons, which disperse for different energies due to the energy dependent drift velocities. A different response to shock arrivals resulting in moderate storms was found by Cattell et al. [2017] and Halford et al. [2015], where the duskward electric field showed a double peak structure and electrons at lower energies (> 50 keV) were accelerated to

relativistic energies, albeit with lower intensity in accordance with the dependency on the Mach number postulated by Schiller et al. [2016]. However, Zong et al. [2009] showed that this is not always the case and small shocks can also cause strong radiation belt responses.

IP shocks can also have a significant impact on ions (H^+ , He^+ , O^+) in the keV range (e.g., Lee et al. [2007], Zong et al. [2012]). Ions in different phases of their bounce motion may be affected in various ways. While equatorial ions are mostly unaffected, ions moving tailwards close to their mirror points can be accelerated quite significantly [Tsuji et al., 2017]. The increased occurrence of EMIC waves in connection to IP shock arrivals may cause the precipitation of ring current ions [Jordanova et al., 2007, Shoji and Omura, 2011], and, thus, IP shocks may have an indirect impact on energetic ions as well.

The sheaths are compressed structures with large amplitude magnetic field variations and high dynamic pressure. Some of the more recent studies extensively investigated the response of the outer radiation belt to sheaths and ejecta of ICMEs separately, as well as combined (“full-ICME”) (e.g., Kilpua et al. [2015], Turner et al. [2019]). They found that storms driven by only sheaths or ejecta, are more likely to deplete electrons above 1 MeV, while full-ICMEs tend to enhance electrons at this energy level. Kalliokoski et al. [2020] reported that, during sheaths, electron flux enhancement occurs predominantly at L-shells between 3 and 5 for source and seed energies, while depletion dominates the core and ultra-relativistic populations, though the balance between depletion and enhancement varies with L-shell. They further concluded that the wave activity during sheaths is enhanced regardless of their geoeffectiveness, in agreement with Kilpua et al. [2019] and Blum et al. [2021]. The depletion/enhancement at $3 \leq L \leq 5$ further depends on the pitch angle [Drozdov et al., 2019]. Whether relativistic or ultra-relativistic electron fluxes increase or decrease further depends on the L-shell, as well as on the strength of the geomagnetic storm or the appearance of chorus and plasmaspheric hiss waves (e.g., Turner et al. [2019], Gu et al. [2020]).

2. Timepix Detector

The Timepix detector [Llopart et al., 2007] is a hybrid semiconductor pixel detector and will be the central piece of technology in a significant part of this thesis. It is part of the Timepix/Medipix detector family developed by an international collaboration hosted by the European Organization for Nuclear Research (CERN) and released in 2006. The first Medipix [Campbell et al., 1998] was developed in the early '90s and it has had four iterations since then. Timepix is a “sibling” of the Medipix2 [Llopart et al., 2002] and it has four iterations by now, with the latest being the Timepix4 [Wong et al., 2020, Poikela et al., 2014, Llopart et al., 2022]. Each consecutive version features improved capabilities, e.g., better time resolution or data-driven readout. The Medipix detectors find applications primarily in X-ray [Tichý et al., 2008, Žemlička et al., 2009, Ballabriga et al., 2013], medical imaging [Butler et al., 2008, Procz et al., 2019, Rosenfeld et al., 2020], and X-ray spectroscopy [Sievers et al., 2011, Hahn et al., 2016, Tremsin et al., 2021], while the Timepix detectors are used in high energy physics [Bergmann et al., 2016, 2019a, 2021], and space radiation dosimetry [Kroupa et al., 2015, Stoffle et al., 2015].

An example of a Timepix detector can be seen in Figure 2.1. In this particular case, the top layer of the detector is the sensor layer made of 300 μm thick silicon. Other semiconductors are also commonly used, such as GaAs or CdTe, and the thickness may vary between 300 μm , 500 μm , 1 mm and 2 mm. The layer underneath the sensor layer consists of the pixel electrodes which are bump-bonded to the CMOS electronics layer. The pixel matrix consists of 256×256 pixels with a pixel pitch of 55 μm , covering a total area of $14.08 \text{ mm} \times 14.08 \text{ mm}$ (198 mm^2). Each pixel is connected to its respective preamplifier, discriminator and a 14-bit digital counter. Timepix can thus be considered as 65,536 individual detectors due to its pixelation, achieving good spatial resolution. Compared to other radiation imaging detectors, it offers a high readout speed, no noise, no dark current, wide dynamic range for measurement of fluxes, and energy discrimination for deposited energy. The dead time depends on the particular readout interface and is of the order of a few tens of milliseconds.

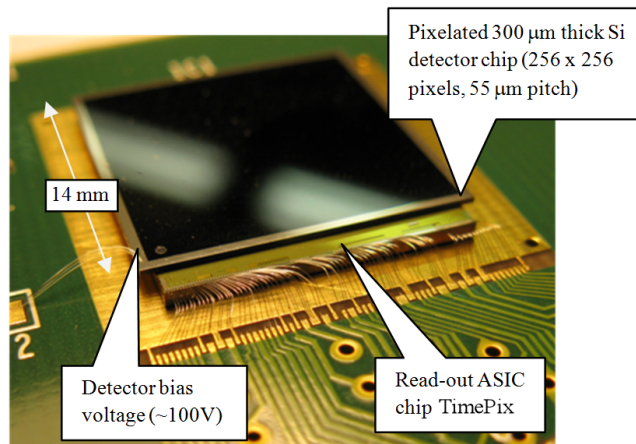


Figure 2.1: An example of a Timepix detector [ESA, 2019].

The general set up of a Timepix detector (common for all Medipix/Timepix

detectors) is illustrated in Figure 2.2. When an ionising particle strikes the sensor, it creates a number of electron-hole pairs. These charge carriers are then separated by the applied bias voltage and drawn to an electrode on either side of the sensor. The drifting charge carriers induce a mirror charge in the pixel electrodes. The induction mainly takes place when the charge carriers are in close vicinity of the electrodes due to the small pixel size to sensor thickness ratio. This is known as the small-pixel effect. This signal is amplified and compared with a pre-set comparator level (energy threshold). If the signal exceeds the energy threshold it will be digitised.

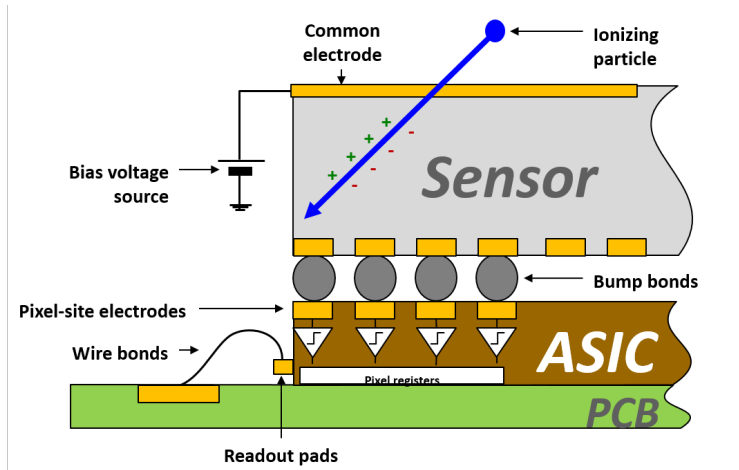


Figure 2.2: Schematic of the Timepix detector. An ionising particle strikes the sensor and creates electron-hole pairs. When the charges approach the bottom, a signal is created. Adapted from [Mánek et al., 2019]

Using a global threshold as well as individual adjustment bits for each pixel, in the so-called THL equalisation the pixel response is homogenised and set to a value safely above the electronic noise level of the detector. Typically this value, which is considered the lowest usable energy threshold for a particular device, is chosen to be ten standard deviations from the noise centroid to allow for practically noise-free operation. For Timepix, this is around 3-5 keV. Data acquisition is handled in so-called “frames”. The sensor is set active for a certain amount of time, where charge carriers generated in the sensor by ionising radiation is being registered. After that period of time (acquisition time), the sensor is set inactive and pixel content of the entire matrix is read out. The resulting image reflects the collected data in a 2D grid of identical volumes. This image is what is called a frame. The acquisition time is defined by the user and it typically ranges from milliseconds to seconds and longer. The Timepix detector has three modes to operate in. The modes can not be used simultaneously in this version of Timepix, but they can be configured individually in each pixel. These modes are the counting mode, the so-called “Time-over-Threshold” (ToT) mode, and the “Time-of-Arrival” (ToA) mode.

Counting mode In the counting mode, the per pixel counter is increased by one each time the signal raises above the threshold.

Time-over-Threshold (ToT) In ToT mode (Wilkinson type analogue-to-digital converter), the time a signal stays above the threshold is measured. In

the background, a high-frequency oscillator clock is running. As long as the signal is above the threshold, the pulses from this clock are counted. The number of these pulses, using a Krummenacher-type amplifier, is proportional to the deposited energy, which again is proportional to the particle energy, if fully stopped. By calibrating the detector with sources of ionising radiation with known energy, the deposited energy can be determined [Jakûbek, 2011].

Time-of-Arrival (ToA) In ToA mode, the time of the detection of a radiation quanta above the threshold is measured. Once a signal crosses the threshold, the pulses from the same high-frequency oscillator clock as for ToT are counted until the end of the frame. From the duration of the respective time interval and the start of the acquisition time, the time of the first detection of a signal can be determined for each pixel.

Timepix detectors are sensitive to all charged particles and to photons in a limited energy range. The sensitivity for charged particles above the threshold energy is essentially 100%. Photons are detected via secondary electrons and they are barely distinguishable from low energy electrons. Charged particles mostly move through several pixels before they either deposit all their energy or leave the sensor on the opposite side, creating a pattern of adjacent pixels. This pattern is called a cluster or track. A cluster is thus the spatially resolved trajectory of a charged particle through the pixel matrix of a Timepix detector.

While electrons produce a rather small amount of electron-hole pairs in the sensor, protons and especially heavier particles create large clouds of charges, with equal numbers of positive and negative charge carriers, travelling in opposite directions to their respective electrode. The two effects which broaden the charge distribution during drift time are diffusion and Coulomb repulsion. Coulomb repulsion occurs once the charge carriers have been separated by sign and its effect increases with the effective energy transfer to the sensor. This causes signals to be registered in adjacent pixels, which are not part of the actual trajectory of the particle through the sensor. However, these additional pixels are symmetrically distributed around the original interaction points of the particle. This is known as the charge sharing effect [Gatti et al., 1987, Campbell et al., 2008, Bouchami et al., 2009].

An additional signal can be induced in neighbouring pixels. Each cloud has its own electrical field. This field produces mirror charges in the readout electronics in nearby pixels, which is registered as a signal, if it surpasses the threshold. This effect, sometimes called halo effect, occurs even if all the charge is projected into a single pixel. It depends on the strength of the electrical field of the charge cloud, i.e., the deposited energy. Heavy charged particles tend to create a significantly larger halo with a width of several pixels, whereas light charged particles usually do not create a halo around their cluster [Kreisler et al., 2007]. Further properties of the track morphology will be discussed in Chapter 4.

Three new Timepix chips are available by now [Ballabriga et al., 2020]. The Timepix2 chip was released in 2019 and is the direct successor of the Timepix. The number of pixels and the pixel pitch size are the same as for Timepix. The ToT and ToA can now be recorded simultaneously in each pixel. It is also possible to completely switch off individual pixels to conserve power. An optional adaptive

gain circuit was added to the front-end as well. The Timepix3 was fabricated in 2014, chronologically before the Timepix2. The naming convention is due to the fact that Timepix3 was developed by the Medipix3 collaboration, whereas both Timepix and Timepix2 were products of the Medipix2 collaboration. Timepix3 is identical in the size and dimensions to the other two Timepix chips. The time resolution is improved to 1.56 ns compared to the 10 ns of Timepix and Timepix2. Timepix3 is the first chip with data-driven readout in addition to the frame-based readout. In this readout mode, only pixels that are hit are read out, while the rest of the pixels remain active. This significantly reduces the dead time of the detector from more than 11 ms for the entire matrix of the Timepix chip to 475 ns per pixel for the Timepix3. The latest chip is the Timepix4. It has a matrix of 448×512 pixels with an on-sensor pitch of 55 μm . ToT and ToA are measured simultaneously, and data-driven and frame-based readout are available. The time resolution is further improved to 200 ps.

3. Instrumentation

The data analysed in this thesis were measured by three different instruments: the Space Application of Timepix based Radiation Monitor (SATRAM) [Granja et al., 2016], the Energetic Particle Telescope (EPT) [Cyamukungu et al., 2014], and the Instrument for the Detection of Particle (IDP) [Sauvaud et al., 2006]. SATRAM and EPT are both operating on board the Proba-V (PRoject for On-Board Autonomy–Vegetation) satellite [Francois et al., 2014, Pro] of the European Space Agency (ESA), which makes it a grand opportunity to compare and cross-calibrate the results from both instruments. The IDP was one of the instruments operating onboard the Detection of Electro-Magnetic Emissions Transmitted from Earthquake Regions (DEMETER) satellite [Cussac et al., 2006]. Data from both the EPT and IDP instruments are used to investigate solar wind impacts on Earth’s radiation belts seen by Low Earth Orbit (LEO) satellites. All three instruments shall be introduced in this chapter with a slight focus on SATRAM.

3.1 Space Application of Timepix Based Radiation Monitor

The Proba-V satellite was launched on 7 May 2013 into a Sun-synchronous LEO orbit of 820 km altitude onboard the Vega launch vehicle. The orbit has an inclination of 98.7°. One circumnavigation of the Earth takes 101.21 min. The local time at the descending node is between 10:30 and 11:30, the local time at the ascending node is between 22:30 and 23:30. At the time of writing, both the satellite and the SATRAM instrument are still in operation after more than ten years. The satellite before the launch can be seen in Figure 3.1, with the SATRAM module attached to the bottom.

SATRAM is a technology demonstrator with the original purpose to show that the Timepix technology can be used as a compact dosimeter in open space. However, it is not the first Timepix detector outside Earth’s atmosphere. Timepix detectors were already used as personal dosimeters for astronauts onboard the International Space Station (ISS) [Stoffle et al., 2015]. Nevertheless, these detectors are in the shielded environment of the space station. SATRAM thus carries the first Timepix detector in open space that is directly exposed to the harsh radiation environment of the radiation belts. Over the years, it was shown that Timepix can do more than just survive in open space. The usage as a particle detector with flux measurement capabilities have been developed constituting a significant part of the work for this thesis.

The SATRAM module has the dimensions 107.1 mm × 62.1 mm × 55.5 mm, which corresponds to the volume of 369.1 cm³. The total weight is 380 g, including the shielding, supportive structures, mounting screws, electronics, and the Timepix detector itself. The nominal power consumption amounts to 2.5 W with a maximum peak consumption of 3 W. SATRAM is built as a single unit to be independent as much as possible from the spacecraft. The casing is made of aluminium and has a thinned area (0.5 mm) right above the sensor. The rest of the top panel has a thickness of 1 mm. The module is built with a Field Pro-

programmable Gate Array (FPGA) for control and readout of the Timepix detector, data compression and payload operation configuration, and for communication with the spacecraft. The radiation tolerance is 100krad for the electronics and 1000krad for the detector.

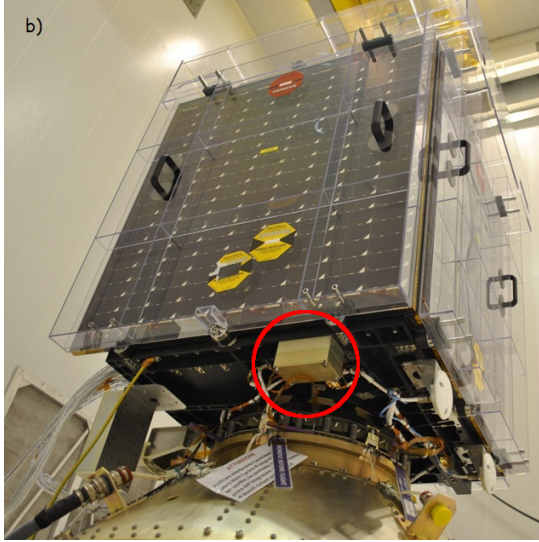


Figure 3.1: The SATRAM module (red circle) attached to the Proba-V satellite prior to launch. Adapted from Granja et al. [2016].

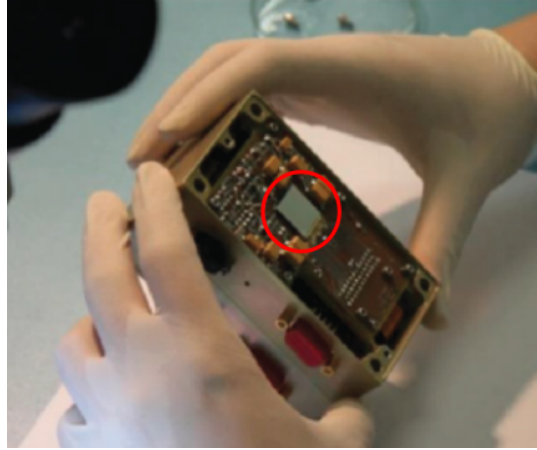


Figure 3.2: Inside view and scale of the SATRAM module with the Timepix sensor marked with the red circle. Photograph by Carlos Granja.

The Timepix detector in SATRAM features a $300\ \mu\text{m}$ thick silicon sensor, which can be seen in Figure 3.2. The threshold level is set globally to 8 keV. It is higher than the standard 3-5 keV threshold level, in order to account for the environment conditions in space. SATRAM is operated in ToT mode. The acquisition time for consecutive frames are set to 2 ms, 200 ms and 20 s, respectively. The various durations of the time frames are intended to cover various energetic particle flux levels that SATRAM encounters in space. The frame readout takes around 100 ms. An additional time is needed for data package compressing before the detector is set active again. SATRAM is not operated at its maximum capacity. At maximum capacity, it would produce a large amount of data, which cannot be stored in the 8 MB onboard memory allocated for SATRAM. The telemetry of the satellite is also limited. Additional idle time after each frame is thus added, so that a rather uniform operation over the entire orbit was assured. This results in average to two to three frames taken per minute, which amounts to 4000 frames per day and a data volume of about 6.5 MB. Some memory space is kept for times of increased radiation intensity, where data frames of larger size are generated. The data includes information about the data acquisition (DAC) parameters, sensor bias, time stamps, satellite position, magnetic field components measured elsewhere on the satellite, and the satellite attitude.

The lower end of the energy range is mainly defined by the thickness of the window above the Timepix sensor. Electrons need a minimum energy of 500 keV and protons an energy of 8.8 MeV to penetrate the aluminium cover. The minimum energy for helium and heavier particles has not been determined. The upper energy range is not so easily defined. A single pixel saturates at above $\approx 1.2\ \text{MeV}$

[Jakůbek, 2011]. However, the energy deposition takes place over several pixels, including to some degree also the charge sharing effect. The upper energy limit therefore depends on the number of hit pixels. Electrons and protons usually do not reach the saturation. The energy resolution is about $\approx 8\%$.

The overall Field of View (FoV) is 4π , but the presence of the satellite practically restricts the FoV from the back side of the sensor. Additionally, the thickness of the window above the sensor, the top panel, and the side panels (3 mm) restrict the FoV, in particular at lower energies. The angular resolution ranges from a few degrees for perpendicular incident angles to about 10^{-3} degrees for tilted incident angles.

As the satellite had to go through a commissioning phase, data was not available until 1 April 2014. The relatively low memory space was not considered at the time, and no time delay between frames was introduced. This caused the data to be concentrated in very short time periods on random parts of the orbit. With the introduction of the artificial delay, the data became equally spread across the orbit. The final setup of settings was achieved in August 2014.

3.1.1 Noisy Pixels

Noisy pixels are pixels that exceed the expected overall countrate in a statistically significant way. Such a malfunctioning pixel sends a signal even though no particle passes through it, and it does so repeatedly. Most of the time, the pixel is recoverable by resetting the detector configuration, but some pixels stay noisy permanently. The number of permanently and even temporarily noisy pixels rise with age and especially radiation induced damage. Consequently, the number of noisy pixels can provide an estimate of the health state of the detector. The quantity of noisy pixels appearing over the years are analysed and the results obtained are presented in this section.

The number of noisy pixels is determined by statistically evaluating the quantity of signals registered by each pixel of the pixel matrix. The used time period is rather arbitrary. It only has to be long enough to be statistically relevant. In this study, a period of one week is selected. Within this time period, the number of counts per pixel is registered in a histogram. This results in a distribution, which is then fitted by a Gaussian distribution. From that, the mean N_{mean} and the standard deviation σ are obtained. The threshold for a pixel to be considered as noisy, N_{thres} , is defined as

$$N_{\text{thres}} = N_{\text{mean}} + 5\sigma. \quad (3.1)$$

This method is repeated for every consecutive week for all data until the end of June 2023. Furthermore, the three different acquisition times had to be considered. Longer frames naturally have more pixels with a signal than shorter frames. This would skew the respective distributions. The analysis is therefore done separately for all three acquisition time lengths. Figure 3.3 shows the resulting relative numbers of noisy pixels.

It can be seen, the ratio of noisy pixels stays below 0.6% (≈ 400 pixels) until the end of 2021. In the year after, a significant increase is noted, culminating at the end of 2022, with as many as 22% ($\approx 14.4\text{k}$ pixels) of the pixels being

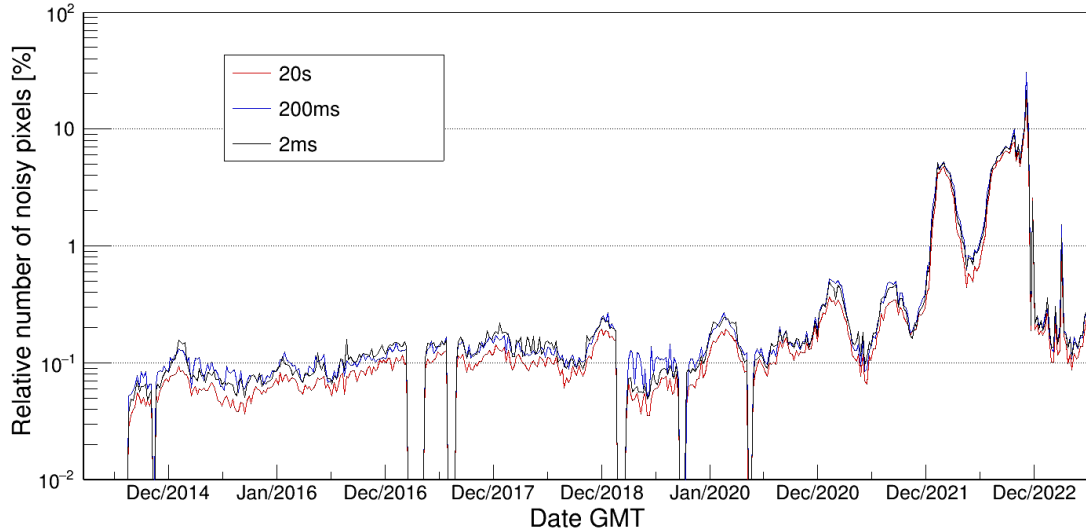


Figure 3.3: Relative number of noisy pixels on a weekly basis from August 2014 until June 2023. Until the end of 2021, the number of noisy pixels stays below 0.6%. In 2022, the number of noisy pixels rose quite significantly, up to a maximum of about 22%. The detector recovered in 2023.

noisy. In 2023, the detector seems to have recovered to low numbers of noisy pixels ($< 0.5\%$ most of the time). Furthermore, some periodicity can be seen in the years 2021 and 2022. The number of noisy pixels increases during spring, and autumn and it decreases during summer and winter. No explanation has been found for this behaviour. There is also no explanation for the subsequent recovery of the detector in the year 2023. A careful inspection shows that most of the time frames indeed look nearly normal. The results obtained for the three different acquisition time lengths are nearly identical.

Figure 3.4 shows how the noisy pixels are distributed over the pixel matrix for the years 2015, 2019, 2022, and 2023. The colour scale represents the number of times a pixel is considered noisy. In all four plots, there are a lot of noisy pixels in the lower left corner. This is a problem that appeared right after the launch of Proba-V. This is a well-known firmware issue of SATRAM and those pixels are always excluded from the analysis. Besides the corner, not many noisy pixels are visible in 2015 and even in 2019. However, a few more noisy pixels are seen, especially at the top and the right edge in 2019. The situation is significantly worse in 2022. Pixels, especially at the edge, are constantly noisy. Some pixels in the centre are occasionally noisy rendering the data completely useless. Nevertheless, the year after, in 2023, only pixels in the lower left corner and on the edges seem to be noisy. Note that for 2023, only six months are considered and, therefore, the counts are reduced.

Part of the data obtained in 2022, where noisy pixels appear across the whole pixel matrix, can not be used for analysis. However, most frames, even those with an increased number of noisy pixels, can still be salvaged. The position of the malfunctioning pixels at the edges makes it easy to mask them and exclude them from the analysis. Their elimination reduces the usable detector area by 21%.

Using the same method for noisy pixel detection, a follow up analysis has

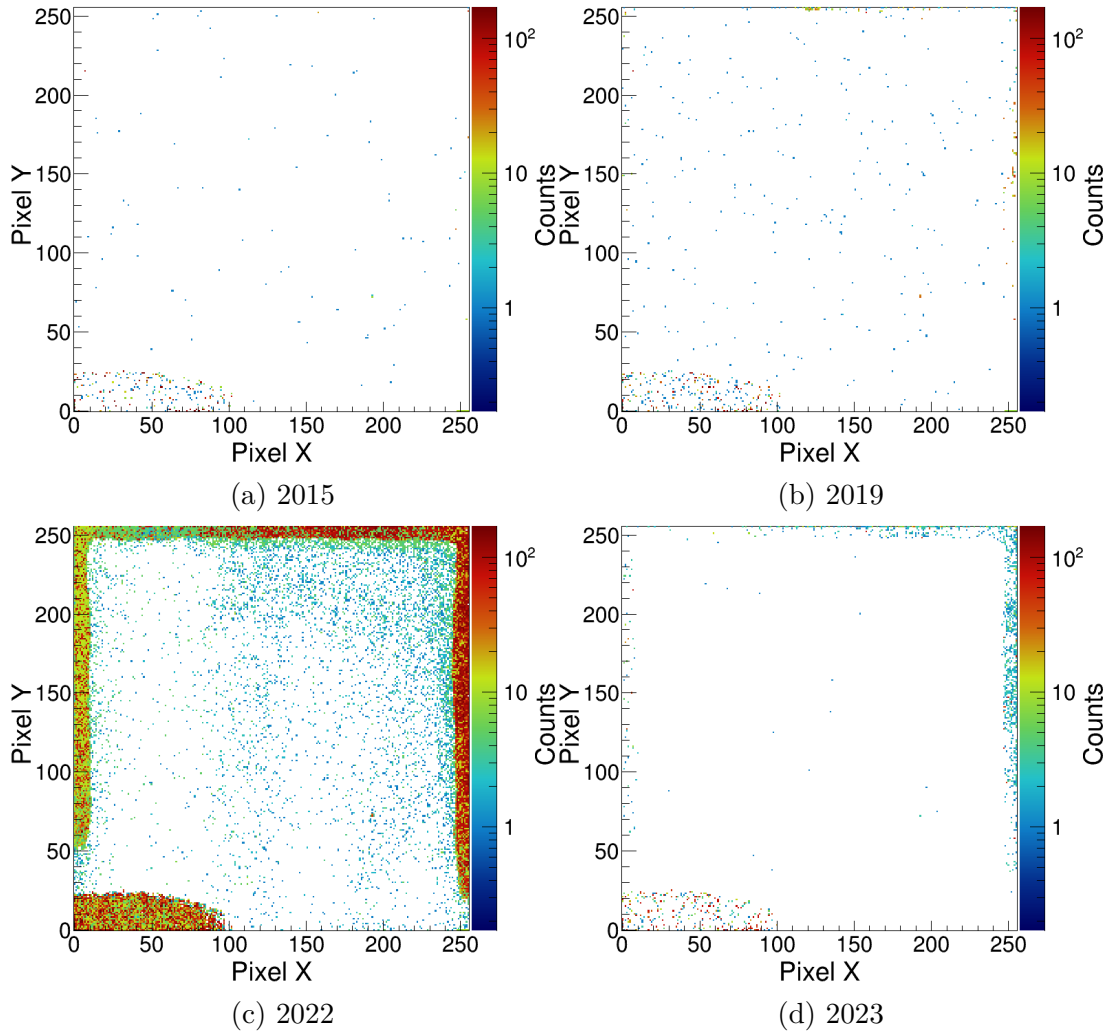


Figure 3.4: Noisy pixel distribution over the Timepix sensor for the years (a) 2015, (b) 2019, (c) 2022, and (d) 2023. The pixels in the lower left corner suffered damage during the launch of the Proba-V satellite. The colour scale represents the number of times a pixel is considered noisy. Note that for 2023, only six months are considered and, therefore, the counts are reduced.

been conducted, but with the reduced area. The noisy pixels in the lower left corner and the edge pixels seen in Figure 3.4c are excluded. The new results are presented in Figure 3.5. It shows the reduction of noisy pixels to below 0.2% (≈ 130 pixels), except for a short period near the end of 2022, where just above 11% of pixels were identified as noisy. It can be concluded that by masking the noisy areas, SATRAM provides reasonable data during its entire 10 years of operation.

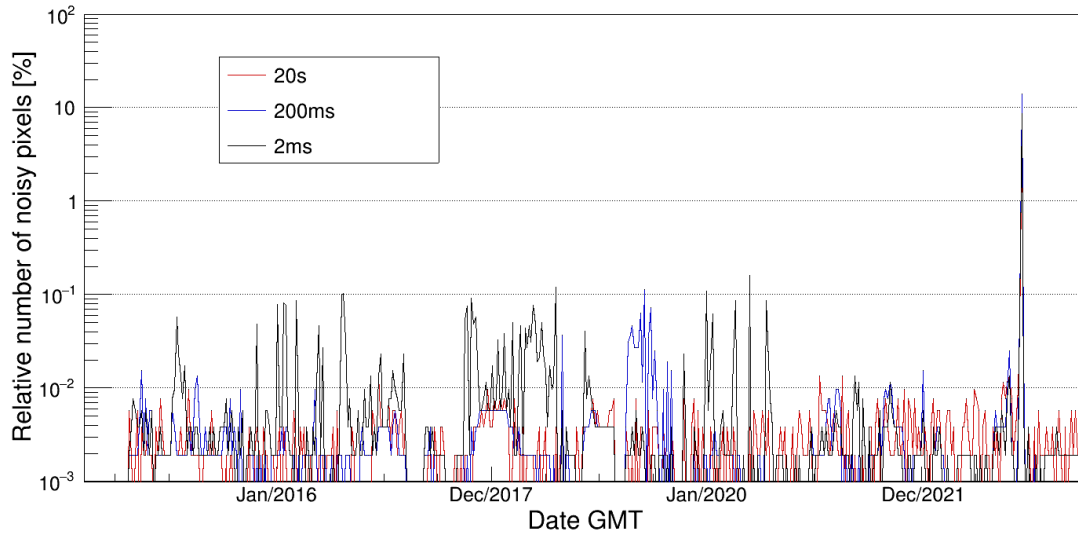


Figure 3.5: Same as Figure 3.4, but excluding noisy pixels from the edges and the lower left corner of the sensor as seen in Figure 3.4c. The relative number of noisy pixels is greatly reduced.

3.2 Energetic Particle Telescope

The EPT instrument is situated on the same satellite as SATRAM. It is a technology demonstrator for science-class type detectors, trying to accomplish measurements of contamination-free fluxes of particles over a relatively wide energy range, but requiring less resources than other detectors pursuing the same science goals. SATRAM and EPT are looking in the opposite direction. One instrument points eastward, while the other points westward. The pointing directions are reversed from dayside to nightside. EPT has the dimensions of $127.5 \text{ mm} \times 162 \text{ mm} \times 211.5 \text{ mm}$ ($= 4.37 \text{ dm}^3$), a mass of 4.6 kg and a power consumption of 5.6 W. The device without cover is shown in Figure 3.6.

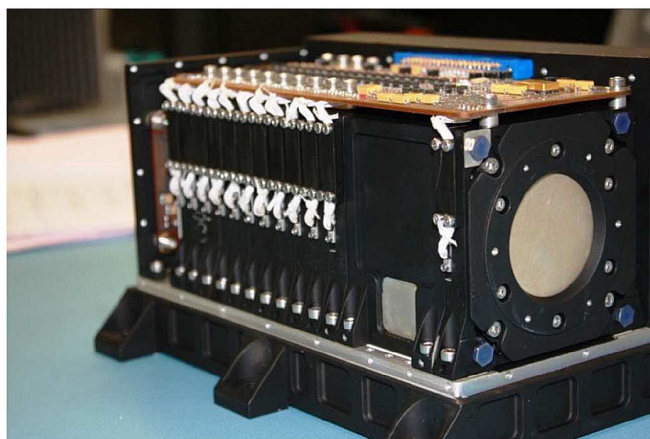


Figure 3.6: Photograph of the EPT instrument with cover removed. Taken from [Cyamukungu et al., 2014].

In total, there are twelve modules containing 23 Passivated Implanted Planar Silicon (PIPS) detectors mainly operating in digital mode, each having a thickness of $375 \text{ }\mu\text{m}$. In Figure 3.7, a cross section view is presented, where the twelve sensor

modules can be identified. On the right hand side of this figure, the opening aperture is visible. The front window is covered by a 200 μm thick aluminium foil. Right behind are the S1 and S3 detectors. S1 has a diameter of 3.5 mm and S3 measures 35 mm surrounding S1. A 50 mm long serrated collimator separates S1/S3 from S2, which has a diameter of 20 mm. S2 serves as trigger for all particle events recorded by the instrument and the threshold is 100 keV.

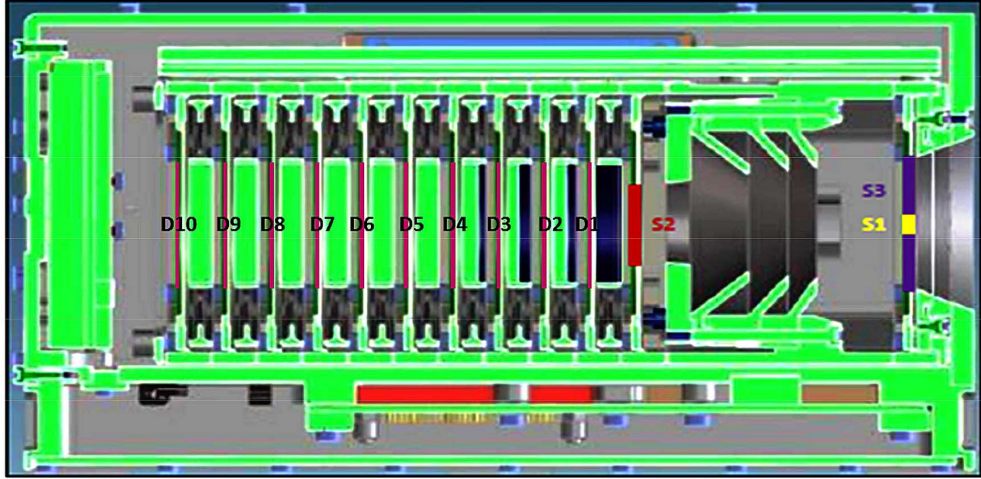


Figure 3.7: Cross section view of EPT with its twelve sensor modules: S1/S3, S2 and D1 to D10. S1/S3 and S2 define the Low Energy Section (LES) and D1 to D10 define the High Energy Section (HES). The LES defines the FoV of 52° . Taken from [Cyamukungu et al., 2014].

The combination of the sensors S1/S3 and S2 forms the Low Energy Section (LES) of the instrument. It operates like a ΔE - E telescope for the detection of low energy particles. The sensor provides an analogue signal that is amplified and digitised using a 12-bit Analogue-to-Digital Converter (ADC). A dedicated firmware stored in a FPGA extracts and records their pulse height. The LES enables the identification of electrons, protons, helium ions, and heavier ($Z > 2$) ions. It also defines the FoV of 52° .

The section behind S2 (to the left in Figure 3.7) is comprised of a stack of Digital and Absorber Modules (DAM). Together with the S2 sensor, the DAMs form the High Energy Section (HES) of the instrument. Each DAM consists of a 35 mm diameter sensor surrounded by an anticoincidence ring of 10 mm width. The absorber part is made of either tungsten or aluminium and is located in front of the central sensor. Each uninterrupted series of up to ten hits defines a HES channel. Only if the particles' identification by S2 is confirmed by S1/S3, the particle is recorded. All signals in all ten DAMs and S1-S3 are used for the energy measurement. The FoV angle decreases with each additional DAM hit, down to 24° for protons hitting up to the last DAM.

The minimum energy is determined by the aluminium foil at the entrance as well as by the thickness of S1/S3. For electrons, the threshold energy is 500 keV, for protons it is 9.5 MeV, and for helium it is 38 MeV. The particles are sorted into separate energy channels. There are six energy channels for electrons, with a maximum energy of 8.0 MeV, ten energy channels for protons, with a maximum energy of 248 MeV, and ten energy channels for helium up to 980 MeV.

Additionally, one overflow energy channel for each of the three particle types exists as well. The energy channels are listed in Table 3.1.

Table 3.1: Energy channels in MeV for each particle type.

Channel	Electrons	Protons	He-ions
1	0.5-0.6	9.5-13	38-51
2	0.6-0.7	13-29	51-116
3	0.7-0.8	29-61	116-245
4	0.8-1.0	61-92	245-365
5	1.0-2.4	92-126	365-500
6	2.4-8.0	126-155	500-615
7	8.0-20	155-182	615-720
8		182-205	720-815
9		205-227	815-900
10		227-248	900-980
11		> 248	> 980

Data is continuously measured and stored in the Proba-V memory until it is downloaded to the ground. EPT is active for > 96.5% of the time. The data can be accessed upon registration through the ESA Space Weather Service Network at <https://swe.ssa.esa.int/csr-ept-federated>¹. From there, the frequently updated particle fluxes determined every 2 seconds can be downloaded and used for scientific purposes.

3.3 Instrument for the Detection of Particle

The IDP was a payload onboard the DEMETER spacecraft. The satellite was devoted to an investigation of ionospheric disturbances due to seismic activity and volcanic activity. It was launched on 29 June 2004, into a Sun-synchronous circular orbit. The inclination was 98.23°, with local times either 10:30 on the dayside or 22:30 on the nightside. In the beginning, the altitude was at 710 km, but it was lowered to about 660 km in December 2005. Scientific operations ceased on 9 December 2010.

IDP has a mass of 535 g and a power consumption of 895 mW. The full IDP module with sensor head and electronic box is shown in Figure 3.8 and in Figure 3.9 a cross-sectional view is presented. The collimator is made of 2 mm thick aluminium. The design is particularly made to stop secondary particles created in the internal parts of the instrument. The opening angle is 32°, which corresponds to an energy dependent geometric factor with a maximum of 1.2 cm² sr, determined through GEANT3 simulations. An aluminium foil of 6 µm is mounted in front of the sensor to block out parasitic light. It also prevents protons below 500 keV from reaching the sensor. The sensor itself is made of 1 mm thick completely depleted silicon with a diameter of 25 mm.

The signal of the silicon diode is detected by a low-noise charge-sensitive preamplifier, and proceeds to a shaping amplifier. In parallel, the signal is applied to a low-level threshold discriminator. Then, the signal is digitised by an ADC

¹Last accessed: 24th of November, 2023

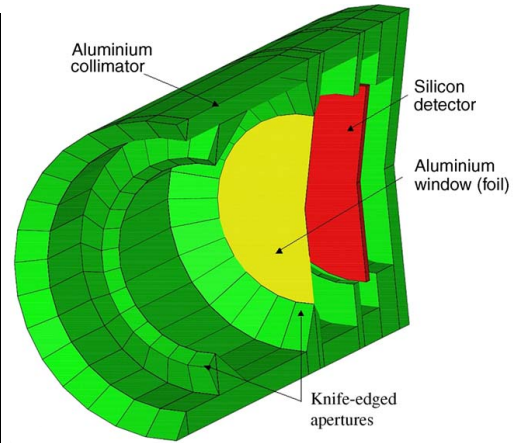
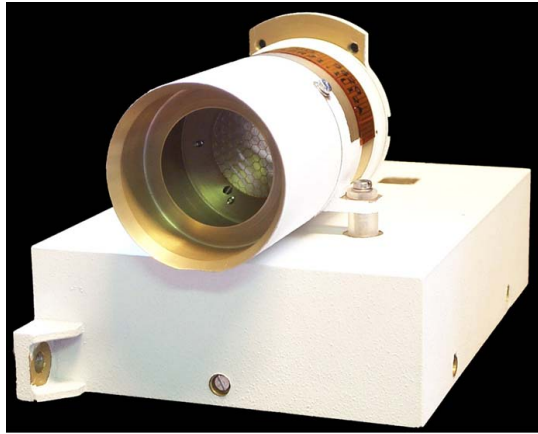


Figure 3.8: Photograph of the IDP instrument. Shown is the sensor head and the collimator made of aluminium is the electronic box below. Taken from [Sauvaud et al., 2006].

Figure 3.9: Cross-section view of IDP: shown in green, the thin aluminium foil for stopping photons and protons below 500 keV is presented in yellow, and the silicon sensor is in red. Taken from [Sauvaud et al., 2006].

before it is sent to an Application-Specific Integrated Circuit (ASIC). The signals are sorted into 256 energy channels. The first 255 channels contain electrons with energies in the range from 70 keV to 2.34 MeV. The last channel contains particles above 2.34 MeV. The energy resolution is below 8%.

IDP has two modes, a burst mode and a routine mode. In the burst mode, electron energy spectra are obtained from all 256 channels individually for every second. The energy resolution is better than 10 keV in this mode. In the routine mode, every two channels are merged and the spectra are taken every four seconds. The data are accessible from the <https://sipad-cdpp.cnes.fr/>² website.

²Last accessed: 25th of November, 2023

4. Particle Identification Methods

In Chapter 2, it is described that particles moving through the Timepix sensor create a pattern of adjacent pixels called track or cluster. Additionally, different particle species create different kinds of tracks with somewhat unique properties. To identify and assign these properties to specific particle species is a key task when working with Timepix data. This chapter deals with methods for particle identification that this work is focussed on. This work concentrates on particle identification specifically in the SATRAM data. At the end of the chapter, a particle identification method using a neural network is introduced.

4.1 Simulation

The detector response is often studied by measuring known radiation fields. However, available sources of particles are often limited in energy range or only monoenergetic. There might not even be available sources for all particle species, the detector will be exposed to. In space, detectors are measuring a mixed radiation field with several particle species and vast energy ranges. Compared to that, data sets created on Earth are rather limited and understanding the response to all encountered radiation might be challenging. To fill the gaps measurements left behind, simulations are used. They are a very useful tool to aid in the completion of the data set of known radiation. This will then help to measure and classify an unknown radiation field.

The simulation of the SATRAM module is crucial for the development of particle identification methods. Simulations are done using the GEANT4 simulation toolkit [Agostinelli et al., 2003]. The simplified model consists of the aluminium casing, the Timepix detector, and the three Printed Circuit Boards (PCBs) inside. The structure of the Timepix detector is well-known and adequately modelled. The aluminium casing has a window of only 0.5 mm thickness right above the sensor. The remainder of the top panel is 1 mm thick. Smaller electronic components are excluded, but given their small size and positioning, their impact on the measurement is rather negligible. The satellite, represented by a block of similar density as the actual satellite, at the back side of the SATRAM module provides strong shielding and is considered in the simulation.

Electrons and protons are simulated in the energy range of 100 keV to 7 MeV and 5 MeV to 400 MeV, respectively. The energy spectra for both particle species are derived from the AE-8-min [Vette, 1991] and AP-8-min [Sawyer and Vette, 1976] models averaged over the SATRAM orbit using the SPENVIS online tool¹ [SPE]. First simulations show that electrons require a minimum energy of about 500 keV to penetrate the aluminium window of the casing above the sensor, while protons need a minimum energy of about 8.8 MeV. The model energy spectra for electrons and protons are shown in Figure 4.1. The respective minimum energies are marked by the red vertical lines. Heavier ions are not simulated yet.

¹AE-9 and AP-9 [Johnston et al., 2014, 2015] were not available in SPENVIS at the time.

Considering the much higher abundance of electrons and protons in the radiation belts, preference is given to them. Validation of the simulation results against ion measurements is also pending.

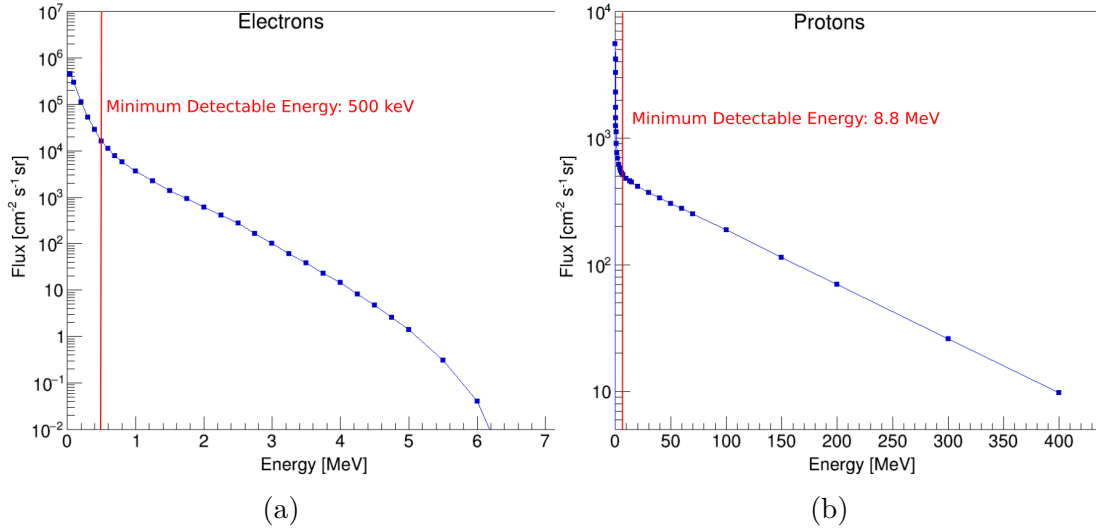


Figure 4.1: Model integrated energy spectrum averaged over the SATRAM orbit for (a) electrons and (b) protons obtained using the AE-8-min and AP-8-min models, respectively. The threshold energies of 500 keV for electrons and 8.8 MeV for protons are marked with red vertical lines.







During this work, various simulation runs with slight adjustments according to the respective requirements are performed. This section serves as an introduction to the basics of the simulation. Results are presented throughout this and the next chapter when needed. Every simulation mentioned hereinafter refers to this simulation, if not stated otherwise.

4.2 Decision Tree Method

The decision tree method is the first method developed to determine electron, proton, and ion fluxes in the SATRAM data. It is based on findings from the earlier days of Medipix/Timepix, that some particle categorisation can be performed on the basis of the shape of clusters [Holý et al., 2008]. Six categories are defined, each related to a group of particles that typically produce a given type of a track. These categories are summarised in Table 4.1.

Photons are detected through secondary electrons (or electrons and positrons if pair production occurs). However, the aluminium casing of SATRAM suppresses the lower energy photons. The presence of the remaining photons is largely neglected in the SATRAM data. Therefore, dots are only considered to be created by low energy electrons or to correspond to a noisy pixel. Small blobs are either electrons or high energy protons that pass the detector perpendicularly to its surface. For heavy blobs or heavy tracks, particles that deposit a large amount of energy are needed. The thickness of several pixels is caused by the charge sharing effect. The more energy is deposited, the larger the effect. Only protons and heavier ions are capable of causing such larger clusters. Electrons need to be highly relativistic to create straight tracks, otherwise they create curly

Table 4.1: Particle classification according to the shape of a corresponding track, after Holý et al. [2008].

Name	Shape	Potential particle species
Dot		electrons, low energy photons
Small blobs		electrons, X-rays, high energy protons
Heavy blobs		protons, heavier ions with short range
Heavy tracks		protons, heavier ions
Straight tracks		high energy protons or electrons, minimum ionising particles
Curly tracks		MeV electrons, gammas

tracks. The latter may only be produced by electrons. Besides highly relativistic electrons, minimum ionising particles or charged particles that are relatively light, such as muons, may create straight tracks.

Additionally to the shape, two more quantities are considered to distinguish the tracks caused by individual particle species: The cluster height and the stopping power. In clusters consisting of several pixels, some pixels have higher registered energies than others. The highest energy in a single pixel for each cluster defines the cluster height. The simulation reveals that electrons with energies up to 7 MeV do not deposit energies above 300 keV in a single pixel. However, the low cluster height is not unique to electrons. Energetic protons (> 100 MeV) approaching their minimum ionising potential do not deposit much energy in the sensor, and they can stay below the 300 keV limit. However, they still usually result in larger clusters than a single pixel only. Clusters consisting of single pixels with cluster heights above 300 keV are probably noisy pixels. Particles, which deposit more energy, more likely produce clusters with more than one pixel due to charge sharing effects.

The third quantity needed for the decision tree method, the stopping power $-dE/dx$, is obtainable through the following calculation:

$$-\frac{dE}{dx} = \frac{E_{\text{clstr}}}{l \cdot \rho_{\text{Si}}}, \quad (4.1)$$

where E_{clstr} is the deposited energy measured in a cluster, also often called cluster volume, l the length of the three dimensional particle trajectory within the sensor, and $\rho_{\text{Si}} = 2.336 \text{ g/cm}^3$ the density of silicon. The challenge lies in the determination of the length l . For some particles in the SATRAM data, this is not achievable. Electrons often produce curly tracks due to being scattered multiple times inside the sensor material. Depending on the energy, the mean free path of electrons can even be smaller than the dimensions of one pixel, which is not detectable at all. Additionally, a frame is only a 2D projection of the track. The information about the trajectory in the third dimension is lost for Timepix detec-

tors. Therefore, curly tracks are excluded from the determination of the stopping power. Another issue is that it cannot be determined if a particle is stopped or if it passes all the way through the sensor. Especially heavier particles are relatively easily stopped even in the small volume of the silicon material. The smaller the elevation angle between the particle trajectory and the sensor plane is, the longer is the path through the detector and even more energetic particles can be stopped.

For the calculation of l , the particle trajectory has to be sufficiently straight. It is further assumed that the particle passes through the whole sensor. Then, l can be estimated by measuring the projected length of the cluster in the frame and by estimating the elevation angle Θ . For dots and small blobs, the angle is estimated to be 90° (perpendicular to the surface), and l is thus determined to be $300\ \mu\text{m}$ – the thickness of the sensor. The length of heavy blobs is estimated by calculating the distance between the centre of mass (CM) with respect to the energy and the geometric centre (GC). For a perfectly round cluster, CM and GC are in the same spot ($|\text{GC}-\text{CM}| = 0$). This means that $\Theta = 90^\circ$ and $l = 300\ \mu\text{m}$. If the distance between CM and GC is larger than zero, the distance is assumed to be the projected length of the trajectory in the frame. Θ and l are then calculated using trigonometric functions.

For straight tracks, the calculation of l and Θ is straightforward as it resembles a line. The distance between the two pixels at the ends of each line is taken as the projected length of the cluster. The rest is trivial. Heavy tracks, on the other hand, are straight, but they are significantly thicker. The strategy here is to reduce the cluster to its core. This is done by removing pixels from the outer rim until only a straight line remains. Then, Θ and l are calculated as for straight tracks. This is explained in more detail in Gohl et al. [2016].

The calculation of the stopping power was first tested on simulated electrons and protons. The results are shown in Figure 4.2. Electrons show a maximum stopping power of $10\ \text{MeV cm}^2\ \text{g}^{-1}$. Given that electron fluxes are usually higher, data in this range is largely dominated by electrons. However, protons are still present in this subset of the data. Above the maximum stopping power of electrons, only protons can be found. The maximum stopping power for protons is about $100\ \text{MeV cm}^2\ \text{g}^{-1}$. The limit is not as strict as for electrons, as there are a few protons above that value.

Calculating the stopping power for the SATRAM data results in what is shown in Figure 4.3. Stopping powers far beyond $100\ \text{MeV cm}^2\ \text{g}^{-1}$ can be seen with values more than an order of magnitude higher. These values can be attributed to heavier ions ($Z > 1$). The plot is divided into three channels. Stopping powers below $10\ \text{MeV cm}^2\ \text{g}^{-1}$ are considered to be electron dominated. Particles with stopping powers between 10 and $100\ \text{MeV cm}^2\ \text{g}^{-1}$ are mostly protons, and particles with stopping powers above $100\ \text{MeV cm}^2\ \text{g}^{-1}$ are heavier ions. Tracks corresponding to each of these stopping power ranges are plotted in Figure 4.4. Figure 4.4a shows many small thin clusters that are not completely straight, as is common for electrons. A few thick tracks are visible, probably caused by protons. Figure 4.4b shows typical proton clusters and Figure 4.4c contains mostly very big clusters, that are common for heavy ions.

Having determined all the three quantities, the particle classification can be done. The cluster height is only used for clusters with a maximum of four pixels.

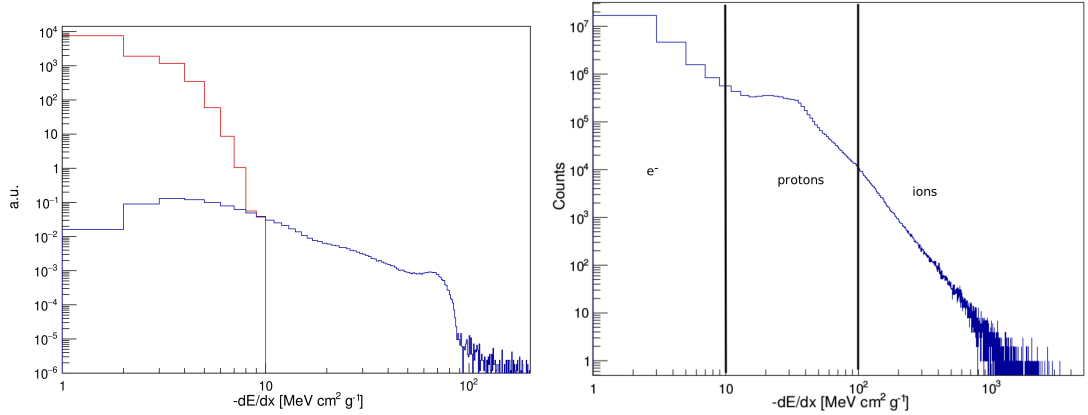


Figure 4.2: Stopping power calculated from simulated data. Electrons are presented in red and protons in blue.

Figure 4.3: Stopping power calculated from SATRAM data. Three stopping power intervals are marked (from left to right): Electrons, protons, and heavier ions.

Especially for longer frames, the chance for particle tracks to overlap is quite high and the cluster height would be the sum of the energy deposition by both particles. The quantity that is most relied on, is thus the shape of the track. The other two quantities are then used to differentiate between the particle species within each category shown in Table 4.1. The categorisation is presented in Figure 4.5. Besides the Θ angle, the Φ angle, which is the angle inside the detector plane to what is defined as the x-axis, is also calculated. Although this angle is not used for the identification of particle species, it could be useful to calculate pitch angles. For completeness, it is mentioned here.

The first category are dots, which are single pixel clusters. If the cluster height is below 300 keV, it is categorised as electron. Next are small blobs. The Θ -angle is set to 90° . The stopping power could be calculated, but it is not used here as it would not really help to distinguish particle species in this situation. The cluster energy would have to be at least 7 MeV to have stopping powers of at least $10 \text{ MeV cm}^2 \text{ g}^{-1}$. Clusters with this much energy are certainly larger than small blobs. Small blobs are categorised as protons if the cluster height is above 300 keV, otherwise they are categorised as electrons.

The next type of clusters are heavy blobs. The stopping power is used to distinguish, whether it is a proton or another ion. Particles with stopping power below $100 \text{ MeV cm}^2 \text{ g}^{-1}$ are categorised as protons, while particles with stopping power above that limit are categorised as other ions. The same is done for heavy tracks. The last two categories are straight tracks and curly tracks. A track is considered straight if at least 90% of its pixels lie on a line between the two end pixels. For straight tracks, the stopping power is calculated to decide whether it is a proton or an electron. Electrons cannot have a stopping power above $10 \text{ MeV cm}^2 \text{ g}^{-1}$ as determined by the simulation. Properties of curly tracks are not computed, as the length and the angles cannot be easily figured out, if at all. However, curly tracks are only created by electrons, and the calculation is thus not even necessary.

This method was published in Gohl et al. [2019]. However, it still has some

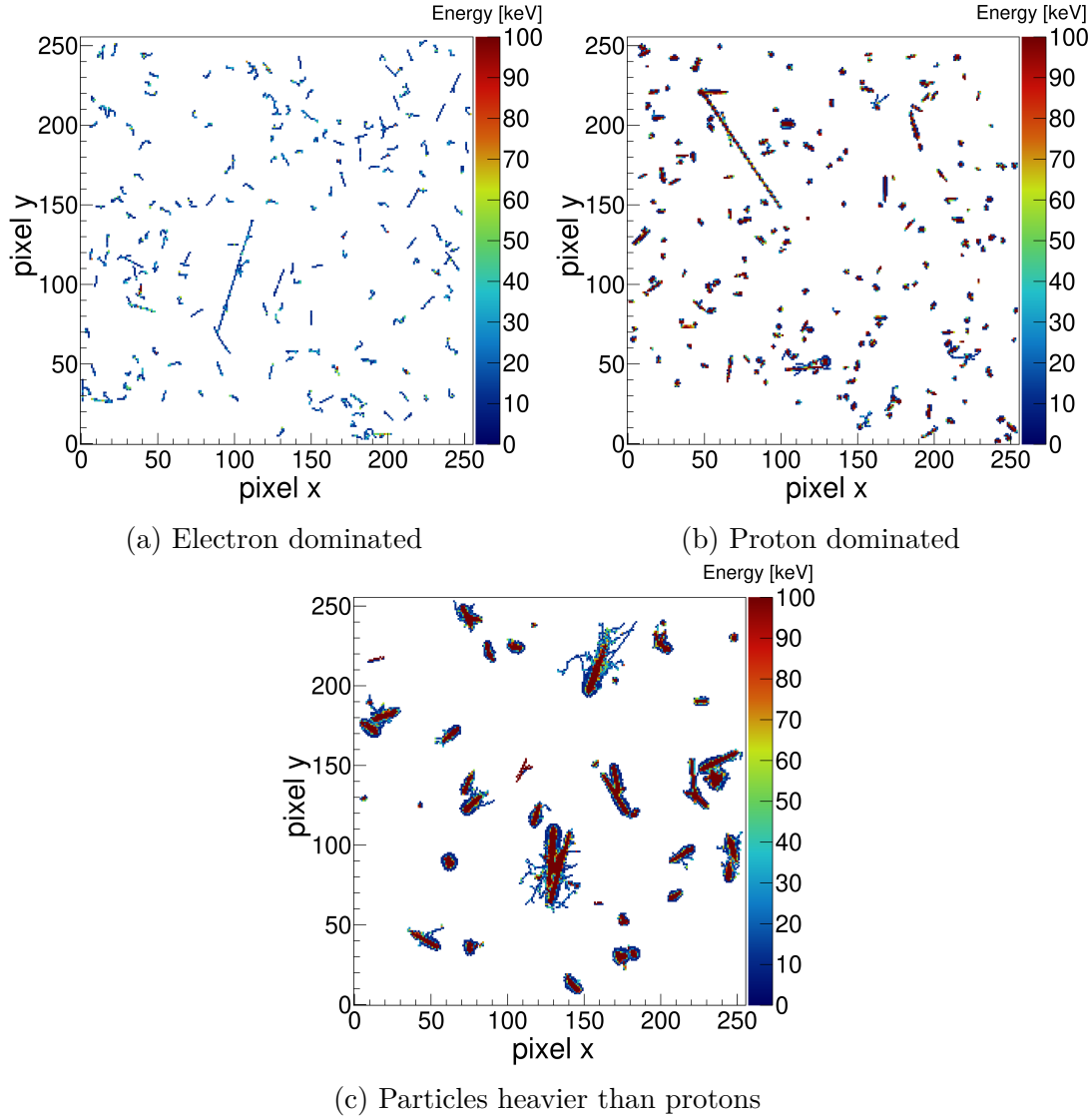


Figure 4.4: Particles sorted according to their stopping power into three channels: (a) low stopping power ($\leq 10 \text{ MeV cm}^2 \text{ g}^{-1}$), (b) intermediate stopping power ($10 \text{ MeV cm}^2 \text{ g}^{-1} < \leq 100 \text{ MeV cm}^2 \text{ g}^{-1}$), and (c) high stopping power ($> 100 \text{ MeV cm}^2 \text{ g}^{-1}$).

obvious weaknesses. First, there are some misclassifications. For example protons that produce small blobs with cluster heights below 300 keV or protons that create straight tracks with stopping powers below $10 \text{ MeV cm}^2 \text{ g}^{-1}$. This is typical for high energy protons ($> 100 \text{ MeV}$) and their tracks are often very similar to electrons. Looking at Figure 4.1, one can see, that these protons make up only a very small portion of the particles that are detected by SATRAM, and their contribution to the electron fluxes can be neglected. Another misclassification can occur between protons and heavier ions. Some ions might have stopping powers below $100 \text{ MeV cm}^2 \text{ g}^{-1}$ and some protons might have higher stopping powers.

However, the biggest issue for this method is overlapping tracks. Clusters need to be caused by single particles that are isolated in the frames. This cannot be guaranteed, especially not in the SAA and in the polar horns. Long frames (20 s) of the SATRAM data are not considered for this method for this reason. Even for

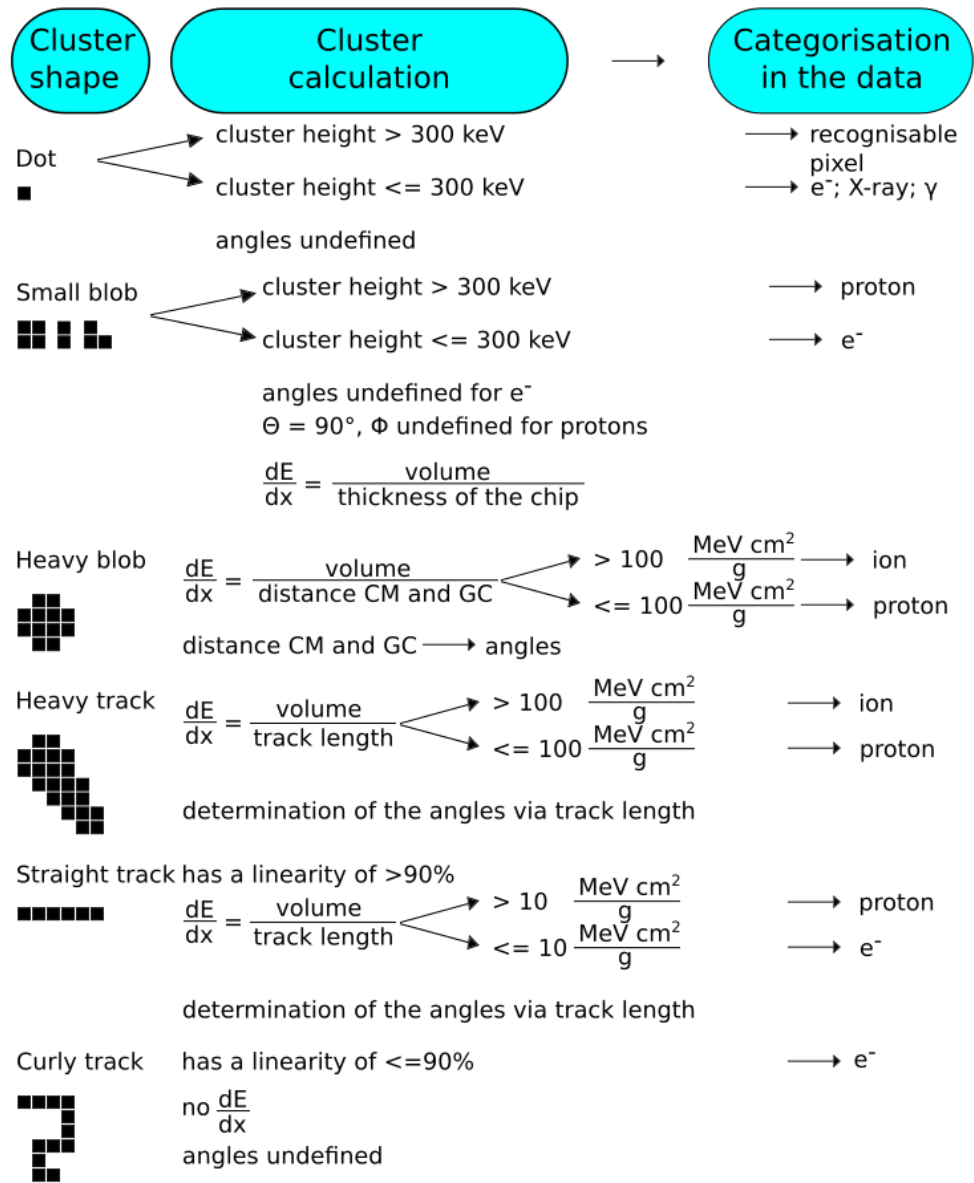


Figure 4.5: Particle identification via decision tree using the shape, cluster height, and stopping power. It is denoted whether the stopping power and the angles relative to the sensor can be calculated. CM stands for the centre of mass related to the energy deposition and GC means geometrical centre. See text for details.

shorter frames, the number of detected particles is systematically underestimated in the SAA.

4.3 Energy per Pixel Method

Satellites have limited capacities in many regards. Mass, power, size, and data memory are often properties that are preferred to be kept as small as possible. There are efforts in the development of instrumentation to design these in ever decreasing size and mass, and with lower power consumption. Timepix detectors are easily an order of magnitude lighter and smaller than common radiation monitors like NGRM [Desorgher et al., 2013] or ICARE [Ruffenach et al., 2019]. Also in terms of power consumption, detectors of the Timepix family offer lower values. The issue for Timepix space applications comes in the amount of data that these detectors produce. A satellite typically cannot provide the telemetry to handle all the data and send it to Earth, as is the case for SATRAM. To address this, the option of onboard processing is explored, which, on the other hand, increases the power consumption. A balance will have to be found.

A recent development was the MIniaturized RAdiation Monitor (MIRAM). Besides the simulation of this device, my task was to find a simple and resource-efficient method to estimate electron and proton fluxes. A method that can be run on a micro processor onboard the MIRAM module itself. The result of this effort is the energy per pixel method, which provides an estimation of the number of electrons and protons in a high flux environment. For low fluxes, another method was developed by colleagues, and it will not be presented here. The MIRAM device, together with both methods, is published in Gohl et al. [2022]. The energy per pixel method is dubbed Method A in the paper.

The method is developed for a Timepix3 detector, which offers more functionalities. While Timepix3 can still measure with a frame based readout, it can also be switched to the data driven readout. Instead of accumulating data over a fixed amount of time, hit pixels are read out immediately. This makes the Timepix3 detector almost dead time free and eliminates the issue of overlapping tracks. However, the energy per pixel method is developed for high fluxes and low power consumption. Therefore, for this method, the detector is running in the frame mode, measuring frames. Consequently, this method can also be used on SATRAM data. In fact, SATRAM data was used to develop this method.

The general idea is to calculate the total deposited energy in the entire frame (by summing up the energy deposited in each pixel of the frame) and divide it by the number of pixel hits in that frame. This provides a value of the average energy per pixel measured in the frame. Considering only electrons and protons, this value will be lowest for only electrons and highest for only protons, as protons tend to deposit significantly more energy than electrons. The value of the energy per pixel is then compared with a look-up table providing the information on the composition of electrons and protons. This table can be created using the SATRAM simulation.

To get an extensive look-up table, a large number of simulations are performed. To start with, a small number of electrons with a random energy in the range of 500 keV up to 7 MeV is simulated to hit the detector to create an artificial frame. In the next simulation, 5% of the electrons are exchanged for

protons with a random energy in the range of 9 to 400 MeV. In this way, another artificial frame is created with the same total number of particles as before, but with 5% protons and 95% electrons. Consecutive simulations are performed with the number of electrons decreased by 5% in each subsequent run, and the number of protons increased by the same number, keeping the total number of particles constant. Once these simulation runs are finished, the total number of particles is slightly increased and the procedure begins anew. The total number of particles is increased until it is ensured that the whole detector is covered and every pixel is hit. The resulting dependence is shown in Figure 4.6.

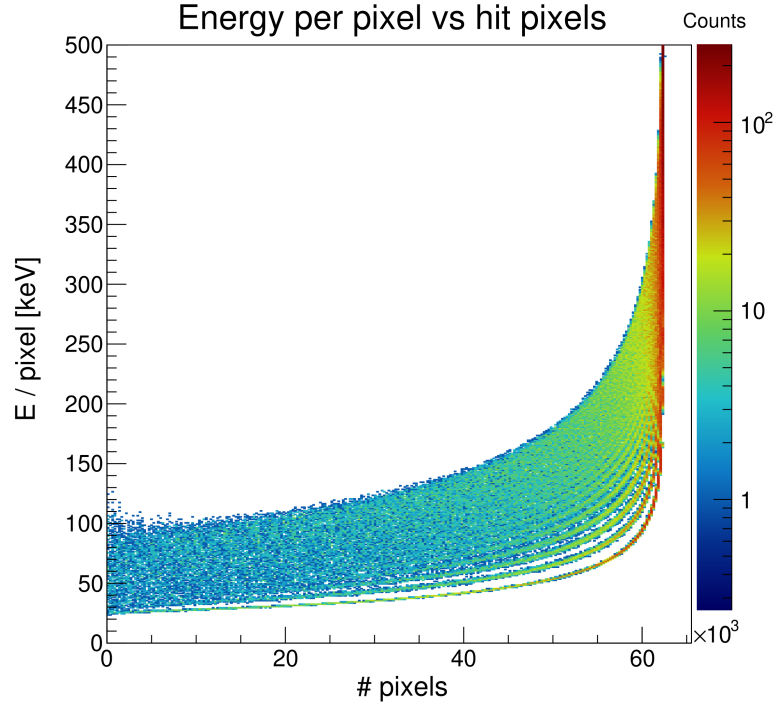


Figure 4.6: Simulation of energy per pixel compared to the number of hit pixels for SATRAM. The bottom edge of the distribution corresponds to 100% electrons, while the top edge resembles 100% protons. The visible lines between $\approx 40\text{k}$ and 60k are unique to a specific particle composition of electrons and protons.

In Timepix3, the number of pixel hits can be counted simultaneously to the ToT. This cannot be done in SATRAM. The limit is the number of pixels available – that is the total number of pixels minus the number of masked pixels. This method fails if all pixels are hit, as it is not distinguishable which energy per pixel value belongs to which particle composition. However, as visible in Figure 4.6, between $\approx 40\text{k}$ and 60k pixel hits, the values of the energy per pixel follow a curve that is unique to a specific particle composition. In a detector, where it is possible to count the individual hits (like Timepix3), these curves are actually constant. The rise in the energy per pixel towards higher pixel hit count is only artificial due the inability to evaluate the actual number of hits. Below $\approx 40\text{k}$ pixel hits, the curves somewhat merge, and the composition is not distinguishable anymore.

Having the look-up table ready, the energy per pixel for each frame of the SATRAM data is then calculated. Only 200 ms long frames are used. 20 s long frames are often completely filled and thus not usable. The shorter frames often

have not enough pixel hits, as 40k to 60k pixel hits are optimal. Putting together all 200 ms frames, this results in the blue-dot dependence depicted in Figure 4.7. Beyond about 30k pixel hits, the data splits into two rather narrow branches, which are eventually merging at the maximum number of available pixels. These branches are overlaid with various simulations of different electron/proton compositions. The best fit is found for 100% electrons for the lower branch and for 85% to 15% electron/proton composition for the upper branch. The data points from the lower branch can be traced almost exclusively to the polar horns, while the upper branch is associated with the SAA. This corresponds to the expected situation of the polar horns being comprised almost exclusively of electrons, while protons make up a significant portion of the SAA. Note that this corresponds to an average situation and that, additionally, the real average percentage can easily be different by one or two percent as the compositions are only simulated in 5% steps and heavier ions are not considered in the simulation.

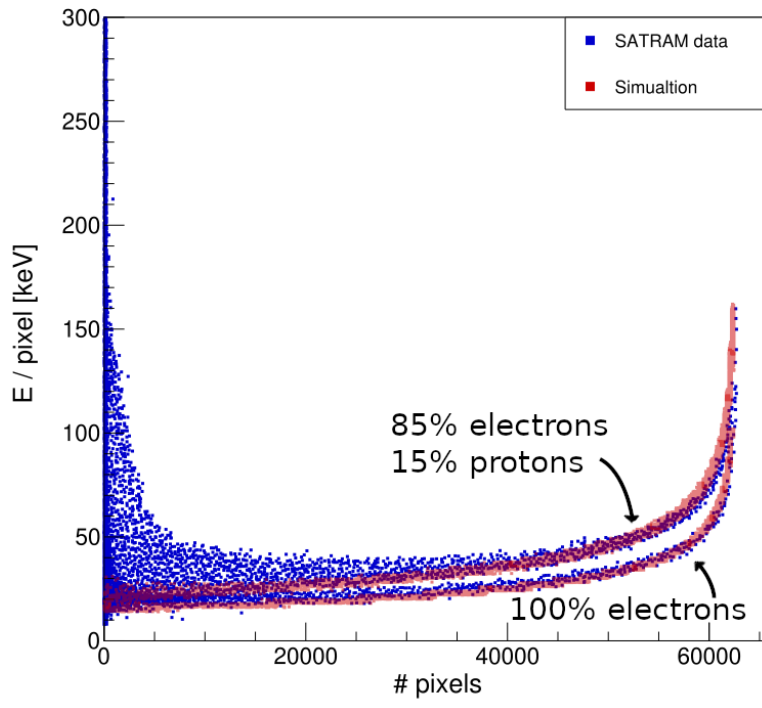


Figure 4.7: Energy per pixel as a function of the number of pixel hits for SATRAM matching measurement (blue) and simulation (red). The best match for higher number of pixel hits ($> 40k$) is found for 100% electrons for the lower branch and a 85/15% electron/proton composition for the upper branch.

At low numbers of pixel hits in Figure 4.7, the energies per pixel show a very broad range of values, which are not observed in the simulation. This is believed to be due to the presence of heavier ions in the data, which is not considered in the simulation. The heavier ions tend to deposit significantly more energy than even protons. A single heavier ion can thus increase the energy per pixel immensely, if there are only a few clusters in the frame. In a frame that has hundreds of particle hits in it, however, a single ion does not significantly change the average energy per pixel.

With this method, the composition of particle species in a mixed radiation field can be estimated. However, it does not directly provide the number of

particles measured. For example, in SATRAM data, it was determined, that there is essentially 100% of electrons in the polar horns, but how many electrons are actually measured can not be determined this way. Particle counting has to be done using another approach. A possible approach is later presented in Section 5.1.1. Additionally, the aforementioned method is based on the knowledge of the particle energy spectra, which are needed in order to create the look-up table.

4.4 Neural Network

The neural network (NN) was developed as a group effort. It is based on experiences with the SATRAM data and the work presented in Section 4.2. The determination of electron fluxes in Chapter 5 makes use of this NN to count the number of detected electrons. The NN is developed in the TensorFlow framework², and it serves as a binary classifier. Only protons and electrons are considered. Just like the decision tree method from Section 4.2, the NN requires that the clusters caused by individual particles do not overlap.

To achieve a better result than before, the occupancy *occ* was introduced. It is calculated for each frame in the following way:

$$occ = \frac{\text{number of hit pixels}}{\text{total number of pixels}} \cdot 100. \quad (4.2)$$

The occupancy is given in percent. The NN is only used for frames with *occ* < 20%. These frames are dubbed low occupancy frames. Frames with *occ* ≥ 20% are called high occupancy frames. This is done to decrease the chances of overlapping tracks, which would result in counting two or more clusters as a single one. The NN is trained with electrons and protons from the simulation in Section 4.1. An omnidirectional flux was simulated.

Table 4.2: List of features used in the NN for particle identification.

#	Feature	Remark
1	deposited energy	energy measured in the detector
2	cluster size	number of pixels in the cluster
3	cluster height	highest energy per pixel per cluster
4	linearity	number between 0 and 1; 1 for perfectly linear
5	roundness	number between 0 and 1; 1 for perfectly round
6	neighbours	average number of neighbouring pixels with a signal
7	fit values	sum of absolute values of cubic and quadratic terms of a third order polynomial fit of the cluster

For the classification of a cluster, seven features are utilised. These features are listed in Table 4.2. One input layer, two hidden layers with seven neurons each, and one output layer compose the architecture of the NN. This is schematically presented in Figure 4.8. An overall testing accuracy of 90.2% is achieved.

²<https://www.tensorflow.org/>, last visited: 3rd of December, 2023

Figure 4.9 shows the confusion matrix for the network. It can be seen that 91% of input electrons are classified as electrons (true electrons) and 9% as protons (false protons). In the case of protons, the result is slightly worse with 89% correctly identified protons (true protons) and 11% protons falsely identified as electrons (false electrons).

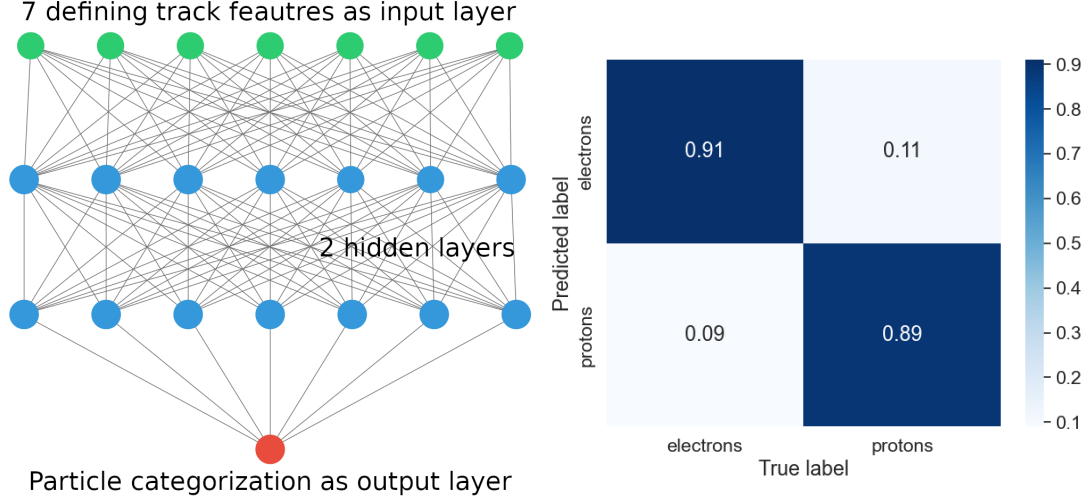


Figure 4.8: Scheme of the NN with one input layer with seven features from Table 4.2, two hidden layers with seven neurons each, and one output layer.

Figure 4.9: Confusion matrix for the NN between truly and falsely identified protons and electrons.

The number of measured (evaluated by the NN) electrons N'_e and protons N'_p can thus be written as:

$$N'_e = 0.91N_e + 0.11N_p, \quad (4.3)$$

$$N'_p = 0.89N_p + 0.09N_e, \quad (4.4)$$

where N_e and N_p are the true numbers of electrons and protons. N_e and N_p are two unknowns in a system of two linear equations. This can be solved to obtain:

$$N_e = \frac{89 \cdot N'_e - 11 \cdot N'_p}{80}, \quad (4.5)$$

$$N_p = \frac{91 \cdot N'_p - 9 \cdot N'_e}{80}. \quad (4.6)$$

Equations 4.5 and 4.6 can be used to calculate the true numbers of electrons and protons from the NN output, accounting for its imperfect classification. Electron fluxes in the SATRAM orbit tend to reach values of the order of $10^6 \text{ cm}^{-2} \text{ s}^{-1}$. Proton flux peak values are of the order of $10^4 \text{ cm}^{-2} \text{ s}^{-1}$. The 11% protons that are misidentified as electrons are thus negligible compared to the total number of electrons. On the other hand, 9% of $\approx 10^6$ electrons are of the order of 10^5 . That is larger than the number of protons. The electron misclassification as protons thus results in a huge error in number of protons. It is therefore not advisable to determine proton fluxes with this method.

While giving reasonable results for electron numbers in SATRAM data, this method gives poor results for protons. In order to achieve a reasonable performance in determining the true proton counts, the method would need to be more accurate. Using additional features for the NN like the stopping power could help with this goal. Furthermore, ions are currently identified as protons. An additional classification of heavy particles should be possible. The latter is work in progress.

4.5 Discussion of Methods

Three methods for particle identification in the SATRAM data are presented in this chapter. The first one, the decision tree method, requires a cluster to be detected without overlapping with the track of another particle to work properly. Some misclassification is tolerated in cases, where protons creating small blobs have a cluster height lower than 300 keV or protons creating straight tracks have a smaller stopping power than $10 \text{ MeV cm}^2 \text{ g}^{-1}$. Additionally, the limit for the stopping power of $100 \text{ MeV cm}^2 \text{ g}^{-1}$ between protons and other ions is not a strict threshold. Some protons have stopping powers higher than that, and some ions have stopping powers less than that. High energy protons ($> 100 \text{ MeV}$) are often not distinguishable from electron tracks, especially when penetrating the sensor perpendicularly to the sensor surface. For the electron fluxes, the misclassified protons are somewhat negligible, as electron fluxes are about two orders of magnitude higher than proton fluxes in the SAA. In the regions of the polar horns, almost no protons are expected, so the difference between electron and proton fluxes is even larger. The fluxes of heavy ions ($Z \geq 2$) are significantly smaller than proton fluxes, and the misclassification of heavier ions as protons can be also neglected.

However, apparent significant proton fluxes are found in the polar horns. This was later understood as misclassified electrons. The situation is similar to the case of the NN, where 11% of false electrons are not significant, but the 9% false protons are. The drastically higher electron fluxes have a larger impact on the determination of proton fluxes than vice versa. Despite the relatively high accuracy of 90.2% for the NN, proton fluxes remain an issue for both methods. Performance of the NN is slightly better than the performance of the decision tree, but it needs an expansion to heavier ions.

Same as the decision tree method, the NN needs non-overlapping clusters to function. Overlapping tracks are the main problem for both methods when applied to the SATRAM data. Even frames with the occupancy as low as 20% already show some overlap. In SATRAM, this problem can not be effectively solved. The low equatorial fluxes outside the SAA require long frame times. Inside the SAA and in the polar horns, fluxes are so high that even short frames can contain a large number of overlapping tracks. In MIRAM, an attempt is made to solve this via duty cycles. If the detector count rate increases beyond a specified threshold, the energy per pixel method is used by utilising the frame readout mode of the Timepix3 detector. When the count rate falls below the threshold again, the method applied is switched back to the method explained in Gohl et al. [2022].

The energy per pixel method is the first attempt to estimate fluxes with a

statistical approach. This is viable for high occupancy frames, where the analysis of individual particles is impossible. It is a relatively simple, and effective approach to estimate the composition of electrons and protons in a radiation field comprised of these two particle species. The low content of heavier ions seems to be negligible in the range of $\approx 40\text{k}$ to 60k pixel hits. However, the method requires the knowledge of the particle species involved in the radiation field, as well as their energy spectra, in order to create the look-up table for comparison with the measured energy per pixel values. Furthermore, in SATRAM, absolute numbers of particles can not be determined with this method. It would require the ability to count particle hits parallel to the measurement of the deposited energy, like Timepix3 has.

The availability of Timepix3 for space – which was only achieved in the last two or so years – enables to achieve better capabilities for particle identification. Timepix3 offers a data driven readout that can eliminate the problem of overlapping tracks. Particles would have to hit the same pixels within a few hundred nanoseconds to be indistinguishable, which is rather unlikely. This would allow methods like the NN to work at peak efficiency. Furthermore, Timepix3 allows the ToT and ToA modes to run simultaneously. With this information, it is possible to reconstruct tracks in 3D [Bergmann et al., 2017, 2019b] instead of just having their 2D projections. This provides more accurate information about the track and can be used to further improve the identification ability.

Additional improvements to the NN can be made by including heavier ions. New track features can be added, e.g., the stopping power. In another research, a convolutional neural network (CNN) was used to identify the energy of protons [Ruffenach et al., 2021]. The CNN was successfully tested on SATRAM data for protons below 50 MeV, providing spectral information about protons in the low energy range. For electrons, this is not possible to achieve in case of SATRAM.

A more recent work uses dE/dx spectrum unfolding to decompose a complex signal into its contributing spectrum components to get spectral information for the particles in a mixed radiation field [Bergmann et al., 2024]. It uses improved algorithms for the angle determination, and thus also an improved calculation of the stopping power. It is also being tested on SATRAM data. Other ideas for improving particle identification worth mentioning here are the development of more complex detectors. The simplest instrument would have two Timepix detectors separated by an electron stopper, which would allow the separation of electrons and high energy protons.

5. Comparison of Electron Fluxes Measured by SATRAM and EPT

This chapter presents the comparison of electron fluxes measured by SATRAM and by EPT. As mentioned before, both instruments are situated on the same satellite. It provides a rare opportunity to compare the results, as measurements of this kind are often taken within large distances both in space and time. The fluxes measured by EPT are available for download at the ESA Space Weather Service Network via log-in¹. They are provided as differential fluxes in energy bins according to Table 3.1. The data includes, among other details, information on the corresponding time and L-shell. Fortunately, the energy ranges of both instruments for electrons coincide perfectly, and no further adjustments have to be made. However, SATRAM fluxes have to be calculated before the comparison can be done.

5.1 SATRAM Data Determination of Electron Fluxes

It was already mentioned in Section 4.4, when the NN was introduced, that it is utilised to calculate electron fluxes for SATRAM data. It is indeed used to determine the number of measured electrons N_e in each low occupancy frame ($occ < 20\%$). For high occupancy frames, a different method needs to be used to determine the number of electrons in each frame. Otherwise, a large portion of the data would be unusable for measuring the fluxes, and, moreover, a systematic bias toward lower electron fluxes would be introduced.

Additionally, the geometry of the detector system has to be considered. In general, a Timepix detector has a FoV of 4π . However, depending on the direction of the particle trajectory relative to the SATRAM module, the detection efficiency is modified by the amount of material that the particle has to pass through in order to reach the sensor. Above the sensor, particles have to pass only through 0.5 mm aluminium, whereas at 90° to the detector normal, they have to pass through about 3 mm aluminium and maybe various electronic components. On the backside of SATRAM is the satellite, which essentially prevents all but the most energetic particles (protons with > 200 MeV) from reaching the detector. The flat sensor ($300\mu\text{m} \times 1.4\text{ cm} \times 1.4\text{ cm}$) results in a geometrical dependence on the impact angle $\propto \cos(\Theta)$. Unfortunately, the impact angle cannot be reliably reconstructed for all particles, certainly not in the case of high occupancy frames. Moreover, the production of secondary particles and particle scattering may play a role as well. Simulations have to be performed to determine overall efficiencies and corrections for all of these aspects. The framework of the simulation described in Section 4.1, with slight modifications, is used for this purpose.

EPT data is taken every 2 s, whereas the sampling of the SATRAM data is more variable. To be able to compare the fluxes, data are averaged over a given time window for both data sets. The time window is chosen to be 60 s long. This

¹<https://swe.ssa.esa.int/csr-ept-federated>

accounts for 30 data points of the EPT data, but only for one to five frames of the SATRAM data in each time interval. The reasons for the low number of frames were already discussed in Section 3.1. The number of electrons is determined for each frame and then summed up to calculate the total number of electrons measured in a given time window (tw) N_e^{tw} . The electron flux Φ_e^{SATRAM} is then calculated according to:

$$\Phi_e^{SATRAM} = \frac{N_e^{tw}}{A_e t g_f c_{sec} 4\pi}, \quad (5.1)$$

where A_e is the effective area, taking into account shielding effects of surrounding material; t is the sum of the acquisition times within the time window; g_f is the geometrical factor defined as the relation between a spherical and the actual flat sensor; c_{sec} is the correction factor for secondary particle production, track interruption, and backscattering; and 4π the general FoV of the Timepix sensor. The fluxes are then given in units of particles per ($cm^2 sr$). What these factors indicate and how they are obtained is explained in the following sections.

5.1.1 Particle Counting

A distinction has to be made between low occupancy frames ($occ < 20\%$) and high occupancy frames ($occ \geq 20\%$). For low occupancy frames, the number of electrons is determined using the NN and Equation 4.5 from Section 4.4. In high occupancy frames, the increasing number of overlapping tracks prevents the identification of individual particles. The method from Section 4.3 could only be partially applied, as it is only valid for frames with 40k to 60k pixel hits. That would only cover frames with about 60 to 90% occupancy.

As a preparation for this method, the mean energy per cluster at each satellite position needs to be determined. This mean energy is obtained by utilising exclusively the frames with low occupancy. The meta data of each frame contains the information on the satellite position in terms of geographical longitude and latitude. The world map is divided into bins as seen in Figure 5.1. The average deposited energy of all tracks found in low occupancy frames is then calculated for each bin. The energy in each bin of Figure 5.1 thus corresponds to the local mean energy of all particles detected in the area. Such a map is created separately for each year in order to account for potential variations in the detector response as well as for long term variation in the spectral composition of the radiation belt particles. The map shown is from the year 2015. The average-energy maps obtained for other years are very similar (not shown).

To count the number of electrons in a high occupancy frame, an estimation of the fraction of electrons in that frame is needed. This is obtained from the last low occupancy frame before the given high occupancy frame, where the fraction of electrons is determined using the NN. The frames are usually reasonably close to each other, so that the composition of electrons and protons can be assumed not to change significantly. The number of electrons N_e in high occupancy frames is then calculated as:

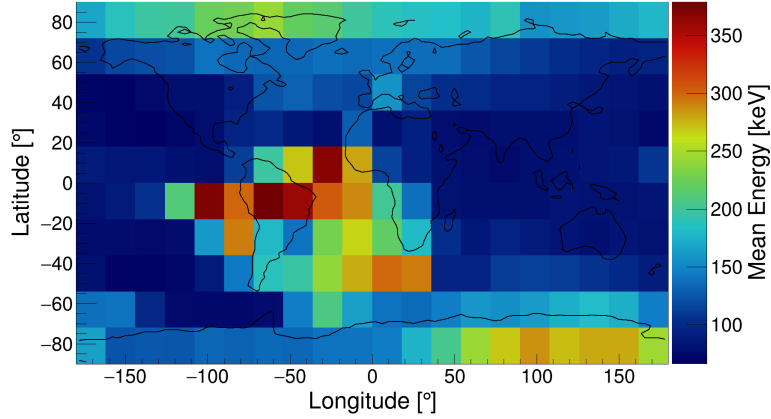


Figure 5.1: Geographical map of the local mean energy of particles identified in low occupancy frames measured in 2015.

$$N_e = \frac{E_{\text{tot}}}{E_{\text{mean}}^{\text{loc}}} \cdot \frac{N_e^{\text{last}}}{N_e^{\text{last}} + N_p^{\text{last}}}, \quad (5.2)$$

where E_{tot} is the total deposited energy in a frame, $E_{\text{mean}}^{\text{loc}}$ the local mean energy according to the position of the measurement in Figure 5.1, N_e^{last} and N_p^{last} the number of electrons and protons, respectively, determined in the last low occupancy frame before the high occupancy frame under consideration.

5.1.2 Effective Area

The influence of the material surrounding the sensor, including the satellite itself, is estimated using a dedicated simulation. The simulation from Section 4.1 is modified to only shoot particles from a spherical source encapsulating the sensor towards the centre of the sensor, instead of simulating an omnidirectional flux. Four additional simulations are performed, where the centre of the spherical source was moved, so it would fall onto each of the four corners of the sensor.

From the simulation, the number of electrons reaching the sensor N_{det} can be determined. Normalising by the total number of simulated electrons N_{sim} and accounting for the detector surface area A_s , an effective area A_e can be estimated:

$$A_e = \frac{N_{\text{det}}}{N_{\text{sim}}} \cdot A_s = 0.19 \text{ mm}^2. \quad (5.3)$$

5.1.3 Geometric Factor

The flat shape of the sensor causes the detection efficiency to be angle dependent. Not being able to measure the incident angle, a geometrical factor g_f is defined to account for this. Two more simulations are performed. In both simulations, the surrounding material is removed, with only the sensor remaining. The particle source is scaled-down, so that the flat sensor would fit just inside. An omnidirectional flux is simulated and the number of detected particles N_{sensor} counted. Then the same simulation is performed again, but with the flat sensor replaced

with a spherical sensor of the same surface area. Again, the number of detected electrons N_{sphere} is counted. The geometric factor is then obtained as:

$$g_f = \frac{N_{\text{sensor}}}{N_{\text{sphere}}} = 1.11. \quad (5.4)$$

5.1.4 Secondary Particles, Track Interruption and Back-scattering

Three simulations are conducted to investigate the production of secondary particles. Knock-out electrons, Bremsstrahlung or photons emitted by excited atoms are potential candidates for secondary radiation. Those can be produced in the surrounding material or in the sensor itself. The original setup from Section 4.1 with an omnidirectional flux is used again. In the first simulation, both primary and secondary particles are tracked. The second simulation is modified to only track primary particles, and the last simulation only tracked secondary particles. It is possible in GEANT4 to simulate the exact same particles over and over by fixing the so-called seeds of the random particle generator. Comparing these simulations gave a sense of the secondary particle production in the SATRAM module.

On top of the analysis of secondary particles, the phenomena of track interruption and backscattering could be investigated with the same simulation setup. Backscattering refers to particles that pass through the sensor, leave it on the other side, are reflected from the electronics situated right behind the sensor, and move back to the sensor. The reflected particles create a secondary signal, which is spatially separated from the first signal, when it passes through the sensor. In the data, these two clusters would be identified as two events, i.e., a single particle would be counted twice. Track interruption occurs when particles with low stopping power pass through the sensor. If such a particle does not deposit enough energy in a pixel to reach the threshold of 8 keV, the pixel will not register a signal. Consequently, if a particle deposits energy above the threshold energy in the first few pixels, then passes through one or more pixels without depositing enough energy to surpass the threshold, but then again deposits enough energy to create a signal, an interrupted track is registered. Here again, two clusters will be counted instead of one.

These effects are most often seen with electrons, at least in the SATRAM data. An example from the simulation is shown in Figure 5.2 featuring all three of these phenomena. Figure 5.2a shows the full event. Two clusters can be observed: a long, slightly winding track typical for electrons, and a short track with only two pixels. Since it is a simulated event, one can be sure that both tracks belong to the same primary particle, as only one event at a time is simulated. Figure 5.2b shows only the primary particle track. Now, three separate clusters can be seen. The long track is missing a few pixels, and it is effectively split in two. The fact that the small cluster is still there strongly suggests that the electron depicted here is indeed scattered back into the sensor. Figure 5.2c shows only secondary particles for this event. There are two clusters visible at the original location of the long track. Given the proximity to the primary track, these clusters probably correspond to secondary particles created within the sensor.

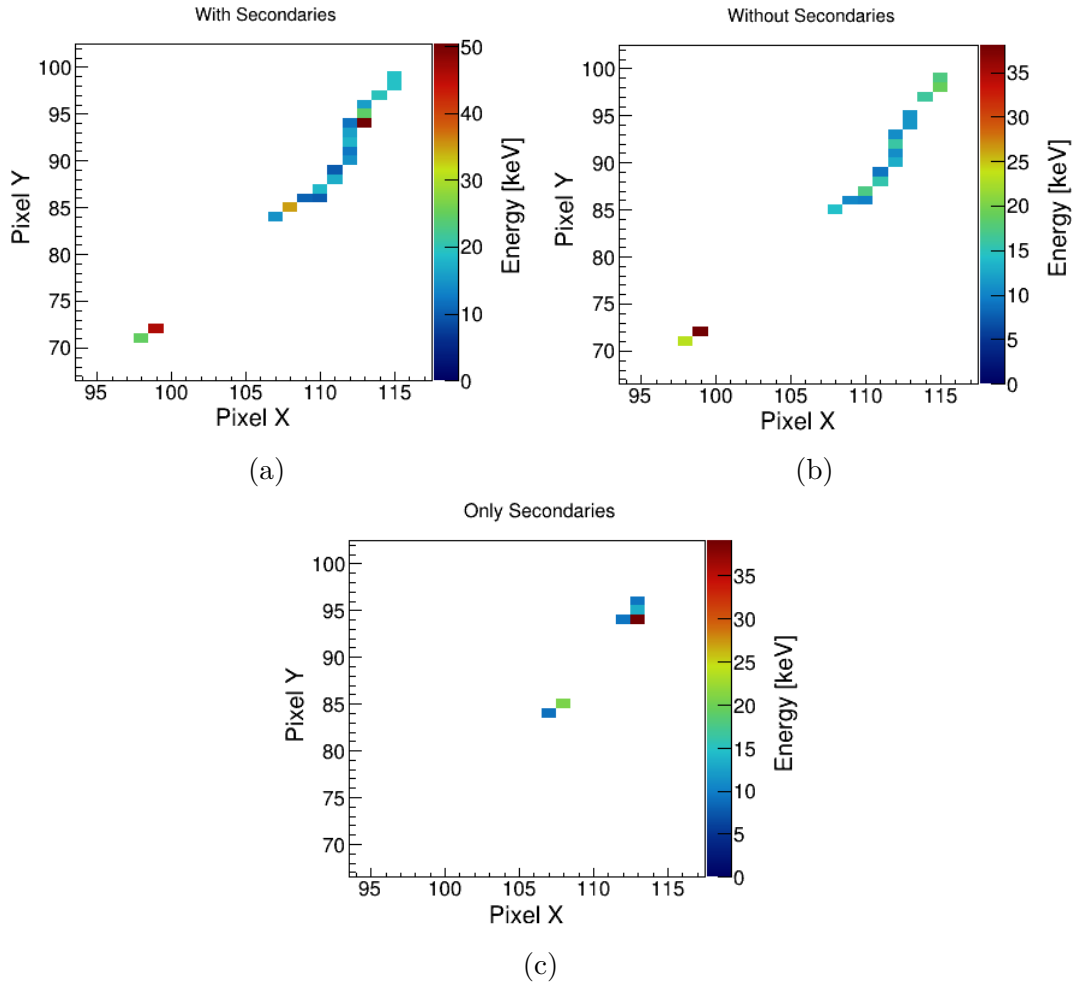


Figure 5.2: An example of a simulated electron event showcasing track interruption, backscattering, and production of secondary particles. (a) The complete event. (b) Only primary tracks. (c) Only tracks corresponding to secondary particles. See text for explanation.

In this case, the secondary particles mitigate the issue of the track interruption, and they are not counted separately. Only due to the backscattering would this event still be regarded as involving two separate particles. However, this is a selected example to showcase backscattering and track interruption, and it cannot be considered a general case. Secondary particles can be produced anywhere in the casing and detected separately from the primary event. Moreover, the primary particle could be scattered and not detected at all.

Interrupted tracks are a relatively common sight created by electrons or minimum ionising particles. Usually, only one or two intermediate pixels are missing and one can guess by the alignment of the two (or more) clusters that they belong to the same particle, as is the situation with the long track in Figure 5.2b. However, there is no guarantee of that. Especially in frames with a long acquisition time, the alignment can be a mere coincidence of several particles hitting the sensor in the right way.

To account for these three effects, the number of detected clusters N_{count} in the simulation, where both primary and secondary particles are registered, are

counted. This number is then divided by the number of primary particles N_{prime} to obtain the correction factor c_{sec} :

$$c_{\text{sec}} = \frac{N_{\text{count}}}{N_{\text{prime}}} = 1.22. \quad (5.5)$$

5.2 SATRAM Comparison with EPT

Having calculated the SATRAM fluxes, their comparison with the fluxes measured EPT can be done. As mentioned before, data from both instruments is arranged and average fluxes are computed in 60s long time intervals EPT energetic electron data is available as differential fluxes in six energy bins shown in Table 3.1 (excluding the overflow energy channel). Due to the inability of SATRAM to measure differential fluxes, EPT fluxes are integrated over all energy bins for the comparison.

Electron fluxes from the year 2015 are shown in Figure 5.3 as a function of time and L-shell. The top panel presents the results from EPT and the bottom panel shows the SATRAM fluxes. The L-shell for SATRAM data is computed using the IRBEM library². The results look very similar. Variations in the fluxes at a given L-shell appear in both plots at the same time. The results thus seem to generally agree. However, the EPT plot is a lot smoother than the SATRAM plot. This can possibly be caused by the limited amount of SATRAM data that is sent to Earth. Only one to five SATRAM frames are available per minute. The amount of data measured in a given one minute time window may be thus rather small, and subsequently statistical variations can contribute a lot to the results.

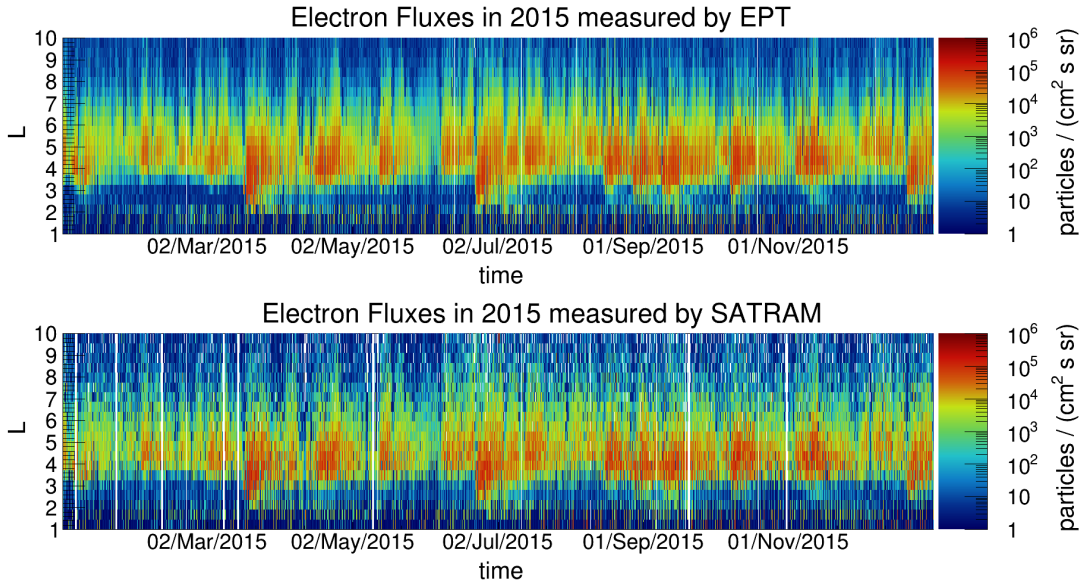


Figure 5.3: Electron fluxes as a function of time (60 s bins) and L-shell (0.5 bins) for EPT (top) and SATRAM (bottom) for the year 2015. The fluxes generally agree, with the EPT results being smoother than the SATRAM results.

²<https://github.com/PRBEM/IRBEM>

Another factor possibly contributing to the coarseness of the SATRAM data is the much smaller active area of the SATRAM detector. While SATRAM has an effective area of 0.19 mm^2 (Equation 5.3), the entrance window of EPT is three orders of magnitude larger. This makes EPT more sensitive in terms of minimal registered fluxes than SATRAM. However, this should be irrelevant at high fluxes, where there are hundreds of thousand of particles per $(\text{cm}^2 \text{ s})$. If the size of the detector played indeed a role in this matter, SATRAM data should be smoother at high fluxes. This is not observed. Nevertheless, some contribution to the coarseness of the SATRAM data at lower fluxes is possible.

Other years show very similar results, with both instruments largely in agreement. Since the middle of 2020, the amount of SATRAM data is even more limited, as seen in Figure 5.4. This can probably be ascribed to the increase in noisy pixels. The low data density remains until the end of 2022. Nonetheless, the remaining data continues to agree with the EPT data. Plots for the rest of the years are not shown in this chapter. They are presented in the Attachment A.1.

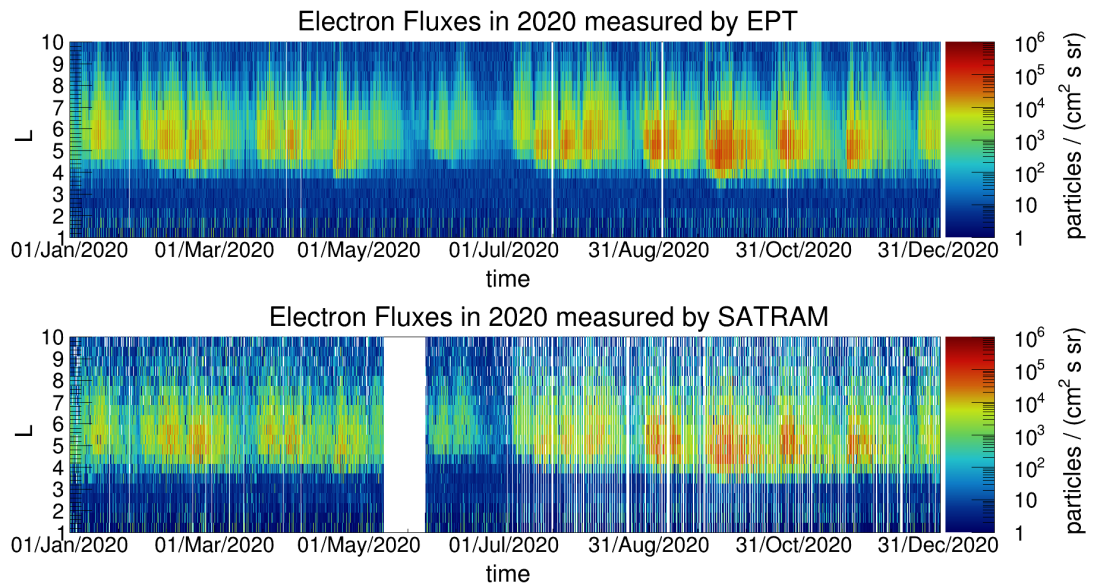


Figure 5.4: Same as Figure 5.3, but for the year 2020. From around July, SATRAM data starts to thin out, potentially due to the increased number of noisy pixels.

The fluxes can also be compared directly by plotting them in a 2D-histogram, with the SATRAM fluxes on one axis and the EPT fluxes on the other. This is shown in Figure 5.5 for the years 2015 and 2021. The black line represents the unity line, where all points would be if fluxes from both instruments agreed perfectly. It can be seen that the majority of data points do not deviate from this line by more than an order of magnitude, marked by the magenta lines. Only relatively few points lie farther away from the unity line. This is true for both years presented here. The correlation factor between SATRAM and EPT fluxes was determined to be 0.83 for the year 2015 and 0.85 for the year 2020. Results for other years are comparable and can be viewed in Attachment A.1.

A large accumulation of data points can be seen at fluxes below 10 particles per $(\text{cm}^2 \text{ s sr})$, where EPT fluxes are slightly higher than SATRAM fluxes. A slight narrowing can be seen at around 50 particles per $(\text{cm}^2 \text{ s sr})$. This might

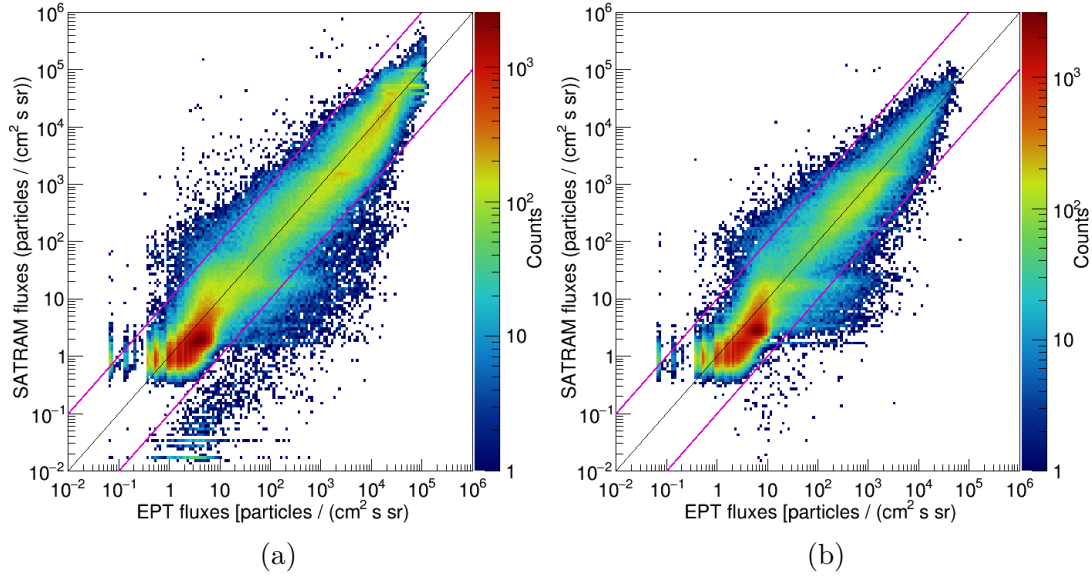


Figure 5.5: The SATRAM fluxes directly compared with the EPT fluxes for the years (a) 2015 and (b) 2020. The corresponding correlation coefficients are 0.83 and 0.85, respectively. The majority of the data points are concentrated close to the unity line (black) and lie within a deviation of one order of magnitude, marked by the magenta lines.

be a consequence of applying the two different methods for the determination of fluxes in SATRAM. Fluxes above that are again slightly higher for EPT. Only above 10k particles per $(\text{cm}^2 \text{ s sr})$, the majority of data points lie on the unity line. Some vertical and horizontal lines can be seen in the lower left corners of the plot. These are most likely artefacts of the integration time of both instruments.

The last comparison is done by plotting the fluxes measured at their respective satellite positions across the globe. Figure 5.6 shows average electron fluxes for 2015 for both instruments. The fluxes measured by EPT seem, in agreement with former results, a bit higher than the fluxes measured by SATRAM. However, they overall agree well. The highest fluxes are measured in the SAA and in the polar horns, as might be expected. The white area over Europe in the EPT map corresponds to the region, where the satellite communicates with its ground station in Belgium. Many instruments cannot operate during this time including EPT. SATRAM operates mostly autonomously, and it can therefore continue to measure even during the time of communication with the ground station.

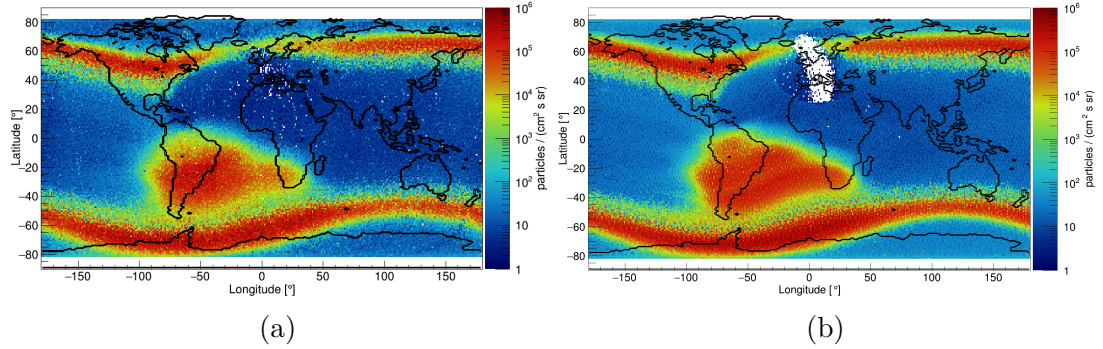


Figure 5.6: Flux distribution over the world measured by (a) SATRAM and (b) EPT during the year 2015.

5.3 Discussion of Electrons Flux Comparison

The results presented here are published in Gohl et al. [2023]. The paper contains results from 2015 to 2019. Since then, data from the years 2020 to 2022 are analysed. Moreover, the figures shown here are slightly updated versions of the ones published in the paper. The L-shells were provided by the EPT group. However, the exact position and time for each SATRAM frame are not available to them. Additionally, the local mean energy is originally calculated only once for the whole measurement period, not for the individual years, ignoring potential changes in the energy deposition sensitivity of the Timepix detector. And last, the investigation of noisy pixels has not been performed at the time the paper was written. Given the low amount of noisy pixels until the end of 2019, consideration of the effect of noisy pixels was not necessary. For the sake of completeness, however, noisy pixels are now considered for every year separately. Note that the noisy pixels in the lower left corner of the sensor have always been excluded from the analysis. The differences between the older plots from the paper and the new plots presented here, are marginally small and may not even be visible. Only a slight improvement in the correlation factors is achieved. However, the analysis of the data from 2020 to 2022 would not have been possible without these steps.

Electron fluxes measured by SATRAM and EPT are in satisfactory agreement for the most part. Both instruments show the same pattern in the variations of fluxes at different L-shells. The direct comparison reveals that most data points are within one order of magnitude deviation from the unity line. SATRAM fluxes are often slightly lower than EPT fluxes. Which detector provides values closer to the real flux, cannot be deduced from this analysis. [Pierrard et al., 2021] conducted a comparison with electron fluxes from the Van Allen Probes at Medium Earth Orbit (MEO). Despite the differences in the orbits, the conditions should be comparable for the same L-shell at same times. Good agreement between the two data sets is demonstrated, which is beneficial for electron fluxes measured by SATRAM as well.

A major issue for SATRAM has been mentioned several times already. Many frames are lost due to the limited telemetry of the satellite. The relatively small amount of data that reaches Earth is prone to statistical variations, which ultimately results in different electron fluxes than EPT measures. Additionally, note that the instruments point in opposite directions at all times. This can contribute

to the observed spread of the data, along with an anisotropic electron distribution in the lower layers of Earth's magnetosphere [Dudnik et al., 2022]. Furthermore, some SATRAM frames are observed to saturate. This is particularly true for 20 s long frames measured in the SAA. Saturation in the energy measurement has been found to underestimate the electron fluxes by a factor of up to five.

The calculation of fluxes can be improved by improving particle identification methods and design changes in the SATRAM device. Arguments and suggestions for these have already been presented in Section 4.5 and they shall not be repeated here. An additional suggestion to be made here is maybe a design that has a better defined FoV. A telescope-like arrangement with sufficient shielding at the thin sides of the sensor could simplify the simulations of the detection efficiency and allow for reliable pitch angle measurements. The device would still be small, allowing the deployment of several Timepix detectors with a telescopic shielding. This would be at the cost of power consumption and an increased need for onboard processing.

6. Electron Flux Variations During Geomagnetic Storms and Interplanetary Shock Arrivals

In the final chapter, investigations of variations of electron fluxes seen by low-altitude spacecraft during geomagnetic storms and interplanetary shock arrival are conducted. First, data from the IDP instrument, introduced in Section 3.3, is used to investigate significant geomagnetic storms during DEMETER's operation period and their impact on the radiation belts. Furthermore, the variations in the particle fluxes are put into relation to selected solar wind parameters. The goal of this study, is to understand the evolution of energetic particle fluxes during the geomagnetic storms and to see, if they behave in a similar manner or if there are some considerable differences between them [Gohl et al., 2021].

The second study is conducted in a similar way to the aforementioned analysis, but this time IP arrivals and their impact on the radiation belts are investigated. Originally, SATRAM data was considered for this, but, as shown in the previous chapter, EPT data offers slightly more dense coverage of particle fluxes and also provides some information about the electron energy spectra. Hence, EPT data was eventually used. Similar to the DEMETER analysis, electron flux changes are investigated and related to selected solar wind parameters. The aim is to identify parameters governing the radiation belt response to the IP shock passage and understand different responses to seemingly similar solar wind variations.

For both studies, LEO satellites have been chosen. The advantage is the high sampling rate, due to their relatively short orbiting periods in the range of one to two hours. Additionally, these satellites are on near-polar orbits. This allows to measure particle fluxes several times a day across all L-shells.

6.1 Energetic Particle Flux Variations Around Significant Geomagnetic Storms

The idea here is to do a superposed epoch analysis. For each storm, a reference point in time is chosen, corresponding to the time of the minimum Dst index. The particle flux variations are then investigated as a function of time relative to the reference time and L-shell. This would reveal potential patterns in the radiation belt behaviour related to geomagnetic storms. Additionally, the flux variations are compared to selected solar wind parameters during the same period of time, again evaluated relative to the reference time. This way, any alleged pattern could be associated with certain solar wind conditions. Finally, it is studied whether the so-called impenetrable barrier at L-shell of about 2.8 for ultra-relativistic electrons [Baker et al., 2014a, Ozeke et al., 2018] also holds in extreme geomagnetic conditions.

6.1.1 Selection of Geomagnetic Storms and Data

For this study, the IDP data from the survey mode is chosen, as it provides larger coverage in space and time. Data obtained at geomagnetic longitudes between -30° and 120° is excluded with the aim to suppress the effects of the SAA. These longitudes are selected according to Figure 2 from Sauvaud et al. [2008]. A geomagnetic storm is considered significant and included in the analysis only if the Dst index reached below -100 nT. The time period of interest is chosen to be seven days long, starting one day before the Dst minimum and ending six days after it. Furthermore, the events are required to be isolated, i.e., only a single significant Dst minimum is allowed to occur in the seven day period, in order to avoid interference from other events. This finally led to the selection of five storms. Four of these storms occurred between May and September 2005 and the fifth storm occurred in December 2006. Table 6.1 summarises the storms displaying their date, Dst minimum, and their reported source according to Jian [2021a] and Jian [2021b], i.e., whether an ICME or CIR was responsible for the storm occurrence. It also contains the information of a type that is associated with the findings in this study, which will be explained later.

Table 6.1: A list of five strong, isolated geomagnetic storms identified during the DEMETER mission. Selection criteria are: i) Dst index below -100 nT, and ii) no other events in a seven-day period around the storm starting one day before the Dst minimum. The date of each storm type (see text), and the storm source (ICME or CIR) are displayed. Adapted from Gohl et al. [2021].

#	Date	Dst Minimum [nT]	Type	Source
1	15 May 2005	-247	1	ICME
2	13 June 2005	-106	2	ICME
3	24 August 2005	-184	1	ICME/CIR
4	31 August 2005	-122	2	CIR
5	15 December 2006	-162	-	ICME

Considering the Sun-synchronous DEMETER orbit, we first focused on the comparison of the energetic particle fluxes measured during the day- and nighttime. The calculated average daytime/nighttime particle fluxes as a function of energy (ordinate) and L-shell (abscissa) are shown separately in Figure 6.1. The fluxes do not differ significantly below $L \simeq 6$. At energies around and below 500 keV, a slight drop in the fluxes between the L-shells of 2.5 and 3.5 can be observed. This drop can be associated with the slot region separating the inner and outer radiation belt. At higher L-shells, some differences between the day- and nightside fluxes are observed. These may be related to considerably different magnetic field distortion at different local times, leading to a more complicated L-shell definition [Roederer and Lejosne, 2018] and to drift-shell splitting [Fok and Moore, 1998]. The subsequent analysis is thus limited to L-shells lower than six, where the possible differences between the day- and nightside can be neglected.

6.1.2 Evolution of the Energetic Particle Fluxes

In the following, the five selected storms are analysed in two ways. First, the energetic particle flux variations during the five storms are superposed. The

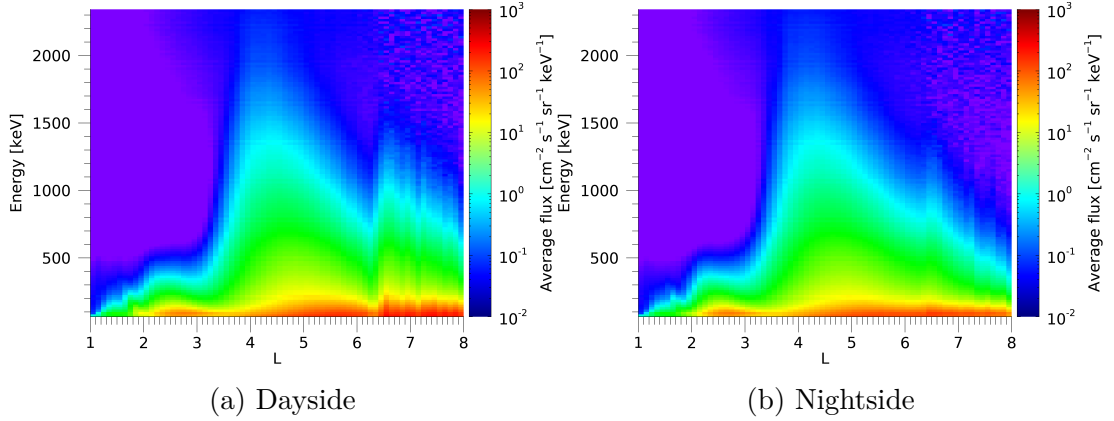


Figure 6.1: Average energetic particle fluxes are colour-coded as a function of energy (ordinate) and L-shell (abscissa) separately for the (a) daytime and (b) nighttime. Adapted from Gohl et al. [2021].

average fluxes are colour-coded in a logarithmic scale as a function of L-shell (ordinate) and time (abscissa). The time evolution is plotted relative to the Dst minimum. The fluxes are averaged over the entire energy range (70 keV to 2.34 MeV). The average Dst index over the course of the seven days is shown as well. After that, the individual storms are investigated in the same format to identify possible systematic differences between them.

The superposed epoch analysis is presented in Figure 6.2. As the Dst index drops, fluxes above $L \simeq 2.2$ rise significantly and stay well above the pre-storm level, only slowly decreasing towards the end of the analysed time window. Higher fluxes can also occur below $L \simeq 2.2$ for about the first half of a day. No other significant feature can be seen in this plot. Four subintervals were selected for a subsequent more detailed analysis. These are marked by the vertical blue lines. Each interval is two hours long. The time interval labelled “Before” starts one hour before the beginning of the plot and is therefore not completely visible.

The investigation of the individual storms revealed significant differences between some of them. It was eventually possible to split the events into two categories, which are labelled “Type 1” and “Type 2”. For each type, two storms are identified. The fifth storm resembled a somewhat intermediate type with an additional feature unique to it. It will be treated independently later in this section. Figure 6.3 shows the superposed epoch analysis for each storm type separately, using the same format as Figure 6.2.

Type 1 storms already show increased fluxes at $L \geq 3.7$ before the Dst minimum, essentially right after the time when the IP shock arrived at the magnetosphere. At the time of the Dst minimum, the particle fluxes at these L-shells suddenly drop to about pre-storm levels, while fluxes at L-shells between 2 and 3.7 increase significantly. After about half a day, fluxes above $L \simeq 2.2$ reach uniformly high levels followed by a typically slow recovery. Type 2 storm only reach high fluxes near the Dst minimum above $L \simeq 2.2$. Type 1 storms also show increased fluxes below $L \simeq 2.2$, which is not observed for Type 2 storms. Furthermore, Type 1 storms demonstrate a clear upturn in the Dst index just before the Dst index drop, in agreement with a SSC. This can be barely seen in Type 2 storms. Additionally, Type 1 storms are stronger and display lower values

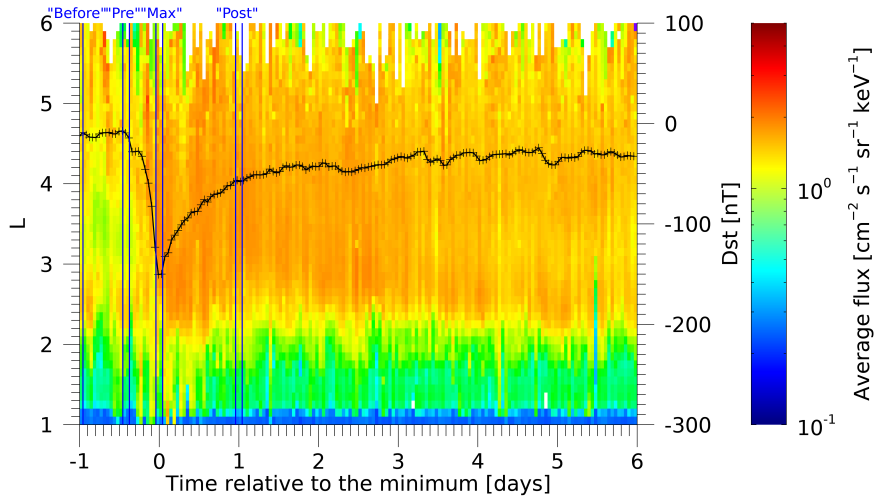


Figure 6.2: Superposed epoch analysis of all five geomagnetic storms in a seven-day window starting one day before the Dst minimum. The average energetic particle flux in the energy range between 70 keV and 2.34 MeV is colour-coded as a function of the L-shell (ordinate) and time relative to the Dst minimum (abscissa). The average Dst index time dependence is overplotted by the thick black curve. There are four time intervals marked by vertical blue lines: one day “Before” the Dst minimum, at the Dst maximum preceding the storm onset (“Pre”), at the Dst minimum (“Max”), and one day after the Dst minimum (“Post”). Adapted from Gohl et al. [2021].

of the Dst index.

Figure 6.4 presents average energetic particle fluxes in L-shell range between 1 and 6 as a function of time and energy. Type 1 storms show increased fluxes of particles with energies above about 1.4 MeV. The high energy particles start to appear at the time, when the (energy-averaged) fluxes at L-shells larger than 3.7 are severely depleted, and they disappear, when fluxes rise again. There is no evidence of enhanced energetic particle fluxes at higher energies for Type 2 storms.

Figures 6.5 and 6.6 display the average particle fluxes as a function of energy (ordinate) and L-shell (abscissa) for the four subintervals in Figure 6.2 for Type

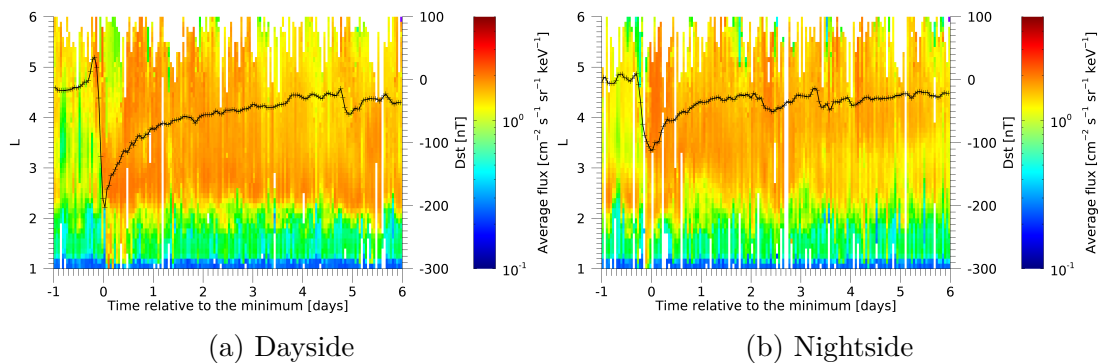


Figure 6.3: The same as Figure 6.2 but separated according to (a) Type 1 storms and (b) Type 2 storms. Adapted from Gohl et al. [2021].

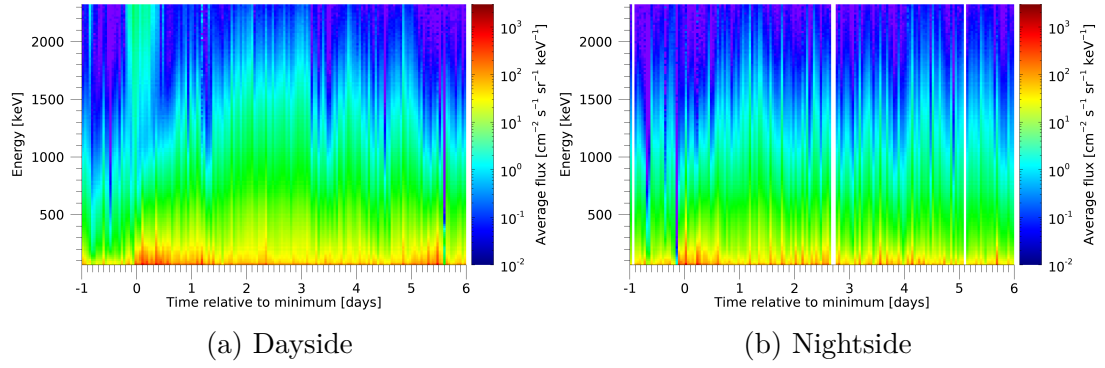


Figure 6.4: Average energetic particle fluxes in L-shell range between 1 and 6 as a function of energy (ordinate) and time relative to the Dst minimum (abscissa) for (a) Type 1 storms and (b) Type 2 storms. Adapted from Gohl et al. [2021].

1 and 2 storms, respectively. The first interval “Before”, corresponding to the period one day before the Dst minimum, is marked in Figures 6.5a and 6.6a. It is followed by a time interval just before the drop of the Dst index, where it reaches its maximum (“Pre”, Figures 6.5b and 6.6b). Figures 6.5c and 6.6c correspond to the time interval around the Dst minimum (“Max”). The last interval, shown in Figures 6.5d and 6.6d, corresponds to the period one day after the Dst minimum (“Post”).

The period one day before the storm serves primarily for comparison purposes only. During the pre-storm period, increased fluxes at high energies for the highest L-shells ($L > 5.5$) are visible for Type 1 storms, but not for Type 2 storms. The largest difference between the two types can be seen during the storm maximum. Energetic particles with energy above ≈ 1.4 MeV appear across L-shells larger than $L \simeq 2.8$. Additionally, higher fluxes of particles with energies between 600 keV and 1.4 MeV on L-shells between 2.8 and 3.7 can be seen, while fluxes of these energies for $L > 3.7$ slightly decrease. Some remnants of high energy particles at high L-shells ($E > 1.4$ MeV and $L > 5.5$) can still be seen a day after the Dst minimum, which are not visible for Type 2 storms.

The fifth storm (also labelled “special case”) is a somewhat intermediate case in the sense that the minimum Dst value lies between the Dst minima of Type 1 and 2 storms. The features in the variations of the energetic particle fluxes are a mix of features that are unique to the two storm types. The corresponding energetic particle flux variations depicted in Figure 6.7a have the same format as Figure 6.3, showing particle fluxes as a function of time and L-shell. The particle fluxes as a function of time and energy, as in Figure 6.4, are depicted in Figure 6.7b. Increased fluxes above $L \simeq 4$ can be seen before the Dst minimum like in Type 1 storms, but they appear about 16 h before the Dst minimum, which is significantly earlier than for the Type 1 storms. However, the depletion at higher L-shells around the Dst minimum is not observed. The flux variations after the Dst minimum are more comparable to Type 2 storms. Energetic particles above 1.4 MeV are seen in this storm as well. They coincide with the increased fluxes 16 h before the Dst minimum, but are significantly less prevalent at the minimum. The data obtained for the selected subintervals are not shown here, but they show large resemblance with Type 1 plots. The only difference is, that the increase of energetic particle fluxes already happened in the pre-storm phase.

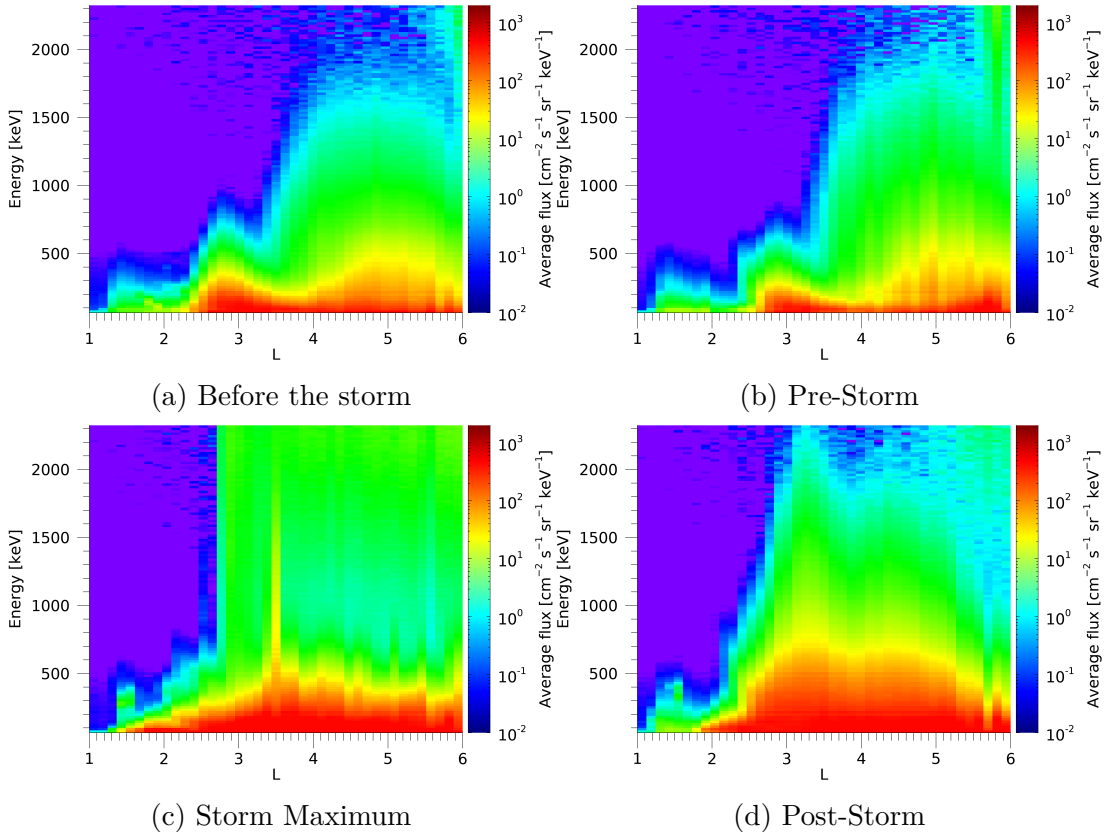


Figure 6.5: Average energetic particle fluxes during Type 1 storms are colour-coded as a function of energy (ordinate) and L-shell (abscissa) during four selected two-hour-long time subintervals. (a) One day before the Dst minimum. (b) Around the Dst maximum just before the storm onset. (c) Around the Dst minimum. (d) One day after the Dst minimum. Adapted from Gohl et al. [2021].

6.1.3 Evolution of Solar Wind Parameters

Having studied the evolution of energetic particle fluxes around significant geomagnetic storms, it is of interest whether and how these variations relate to solar wind variations. Therefore, several solar wind parameters are chosen and presented in Figure 6.8. The selected parameters are the solar wind flow speed v , the plasma number density n , the IMF magnitude B , the IMF B_z component and the plasma beta β . Additionally, the Dst index and the AE index are plotted alongside. The solar wind parameter data are taken from the OMNI data set [King and Papitashvili, 2005] with 5 min time resolution. The two storms of each storm type are plotted together.

In the case of Type 1 storms, an IP shock seems to arrive only shortly before the storm onset. The respective solar wind variations are sudden and tend to be very strong. Already after a few hours, the plasma number density and the IMF magnitude return to pre-storm levels, while the solar wind flow speed takes about two to three days to relax. The IMF B_z component exhibits a bipolar change in both cases, with a very short period, where it is southward. In particular, both these events are south-to-north (SN) type. On the other hand, the solar wind parameter around the times of the Type 2 storms evolve more slowly. The maximum solar wind flow speed is only reached after about four days. Together

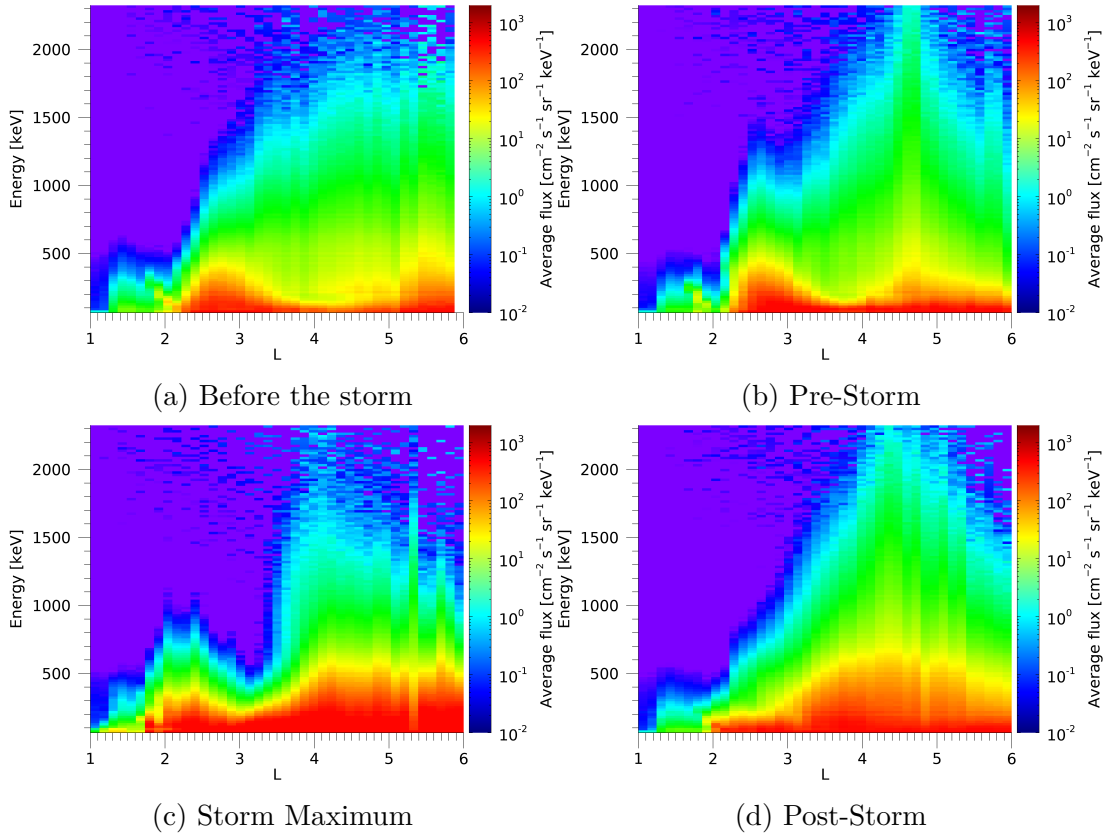


Figure 6.6: The same as Figure 6.5, but for Type 2 storms. Adapted from Gohl et al. [2021].

with the plasma density and the IMF magnitude, some variations already occur up to a day before the onset of the storm. Both cases are south (S) type storms, as the IMF B_z component turns southward at the onset of the storm and stays southward for a couple of hours, before returning to pre-storm levels. The plasma beta does not show any strikingly characteristic variations regarding Type 1 or 2 storms.

The main difference in solar wind parameters between the special case and Type 2 storms seems to be the solar wind flow speed. Instead of a gradual rise, there is a sudden rise more than half a day before the Dst minimum. Furthermore, a spike in the AE index appears before the drop of the Dst index, which is not visible for Type 1 and 2 storms. This peak appears to be coincident with an IP shock arrival and with the increased energetic particle fluxes observed at $L \geq 4$ at about the same time.

6.1.4 Observed L Barrier

In Baker et al. [2014a], an impenetrable barrier for ultra-relativistic particles was reported using the Van Allen Probes spacecraft data. This barrier effectively limits high-energy particle fluxes to L-shells larger than about 2.8. In this section, it shall be investigated whether this L-shell barrier also holds under the extreme geomagnetic conditions around the time of the storm maximum. To suppress statistical fluctuations and to make the analysis more feasible, the number of

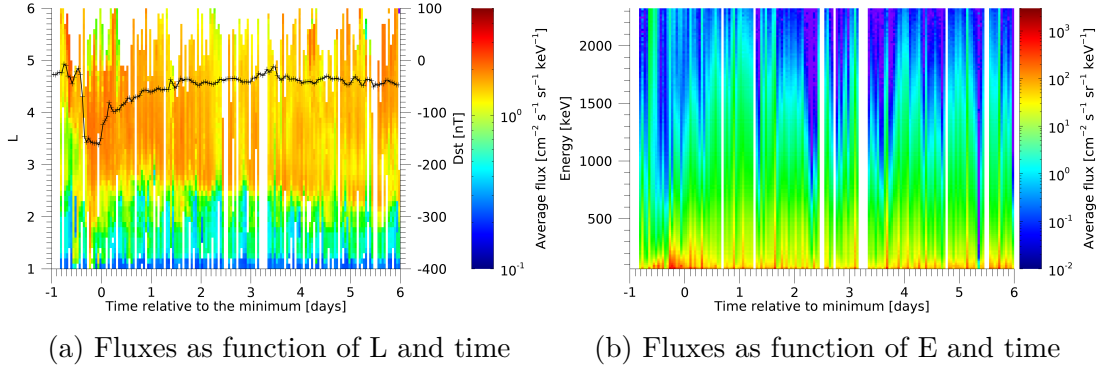


Figure 6.7: Dependences obtained for the fifth storm that fits neither Type 1 nor Type 2 classification. (a) Energetic particle fluxes colour-coded as a function of L-shell (ordinate) and time from the Dst minimum (abscissa). The Dst index is overplotted by the thick black curve. (b) Average energetic particle fluxes at L-shells between 1 and 6 colour-coded as a function of energy (ordinate) and time relative to the Dst minimum (abscissa). Adapted from Gohl et al. [2021].

energy bins is reduced to eight, while still covering the entire energy range.

To determine at which L-shell the drop of energetic particle flux occurs, the average particle flux in a twelve-hour-long interval starting at the Dst minimum is plotted as a function of L-shell. An example of such a plot for the highest energy bin (2057.6–2342.4 keV) on 15 December 2006 is shown in Figure 6.9. Fluxes at low L-shells are generally very low, around zero. At a certain L-shell, fluxes suddenly rise, forming a steep flank. This steep increase is fitted with a hyperbolic tangent. The L-shell, where the particle fluxes reach half of the local maximum just after the increase, is defined as the L barrier. It is marked by the black line in Figure 6.9. This procedure is done for all five storms and for all energy bins.

Figure 6.10 presents the results. The different storm types are colour-coded – blue for Type 1 storms, green for Type 2 storms and red for the special case. No significant difference between the storm types can be identified. In all cases, the L barrier at 100 keV lies between L-values of 2.2 and 2.4. With increasing energies, the barrier rises more or less significantly. Above 1 MeV, it stays at a somewhat constant L-shell between $2.5 \leq L \leq 3.7$. For the highest energy analysed, the obtained barrier L-shells are generally above about 2.6, which is quite consistent with former findings [Baker et al., 2014a].

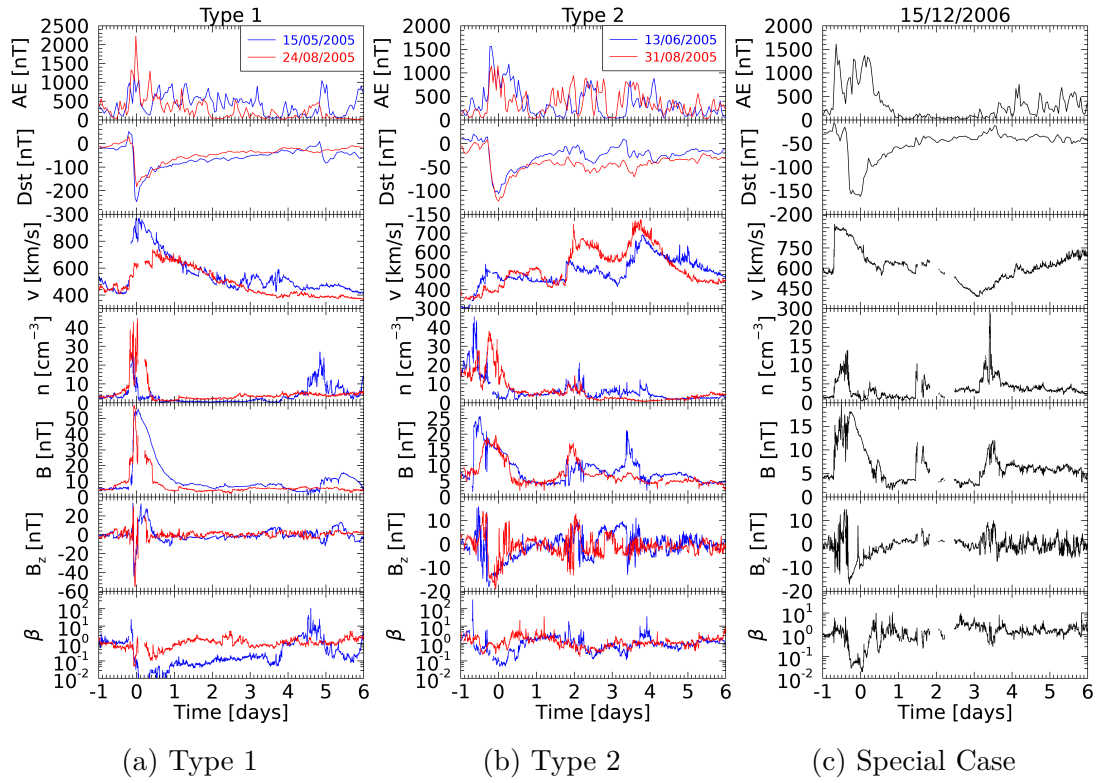


Figure 6.8: Time dependences of the AE and Dst indices, solar wind flow speed v , solar wind plasma number density n , IMF magnitude B , IMF B_z component, and the plasma beta β for (a) Type 1 storms, (b) Type 2 storms, and (c) the special case. Adapted from Gohl et al. [2021].

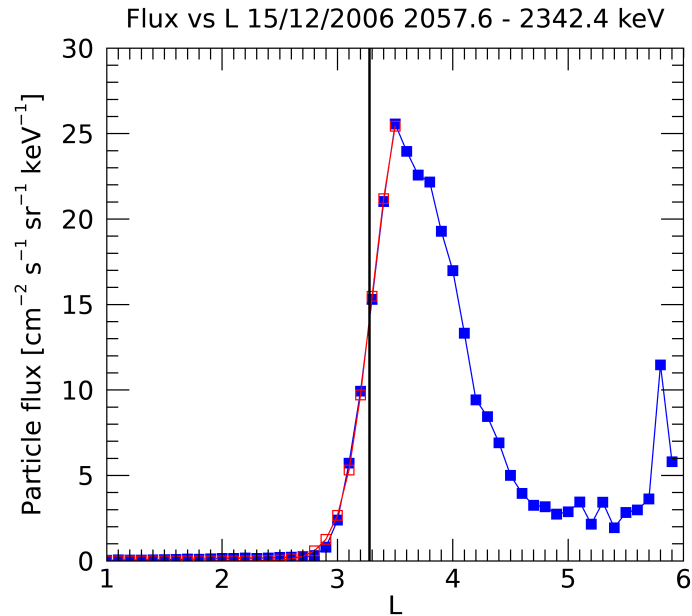


Figure 6.9: The particle flux measured during the storm on 15 December 2006 in the energy range 2057.6–2342.4 keV (blue). The leftmost flank is fitted with a hyperbolic tangent (red). The position of the L barrier is defined as the point, where the flank reaches half of its height. This position is marked by the vertical black line. Adapted from Gohl et al. [2021].

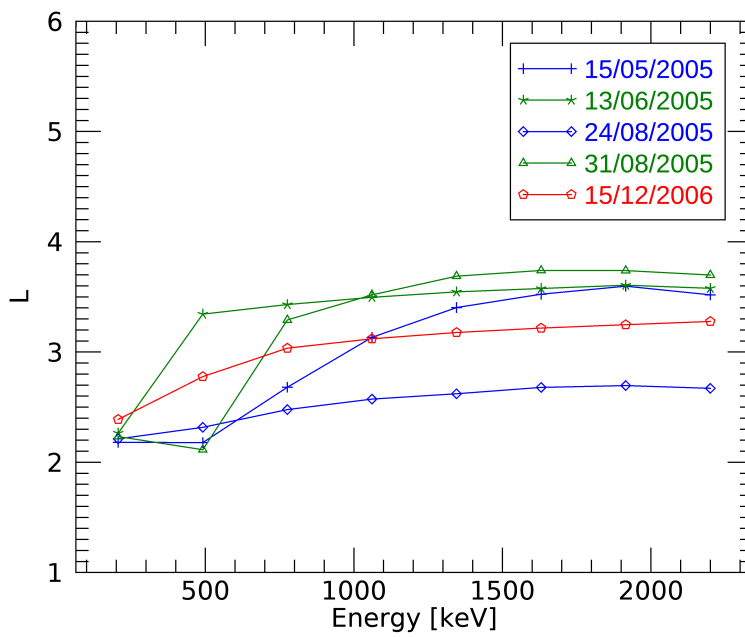


Figure 6.10: The impenetrable barrier L-shells as a function of energy for all five storms. The colours represent the different storm types, blue being Type 1 storms, green Type 2 storms, and red corresponds to the special case. Adapted from Gohl et al. [2021].

6.2 Impact of Interplanetary Shocks on the Radiation Belt Environment

In this analysis, 31 interplanetary shocks from the OMNI data set [King and Papitashvili, 2005] are selected from the years 2013 to 2018. All of these shocks are fast forward shocks. Data for the radiation belt electron fluxes are provided by EPT (see Section 3.2). At first, a superposed epoch analysis like in the previous section is performed. It did not reveal any significant systematic global change in the radiation belt fluxes around the shock arrival times. However, detailed investigation of individual events revealed that while some radiation belt fluxes are nearly unaffected by some of the IP shocks, other IP shock arrivals resulted in sudden drops of energetic electron fluxes over a broad range of L-shells. This is demonstrated in Figure 6.11, where four examples of IP shocks are shown. The times of the shock arrivals correspond to the OMNI data and are used as the reference points in time. Each figure features the dynamic pressure in the top plot, the electron fluxes averaged over all energies as a function of L-shell and time together with the subsolar magnetopause distance in the middle plot, and the IMF B_z component of the IMF in the bottom plot. Note that the data measured in the region of the SAA was again excluded from the analysis.

The first shock (Figure 6.11a) shows relatively weak changes in the solar wind parameters. The dynamic pressure only increases by about 3 nPa, the subsolar magnetopause position moves closer to Earth by about $2 R_E$, and IMF B_z has a southward component of -8 nT at the lowest. However, electron fluxes at $L \geq 6$ got significantly depleted. Figure 6.11b depicts an event with significantly stronger variations in the solar wind parameters. As a result, electron fluxes at L-shells above ≈ 4 are substantially decreased. The third shock in Figure 6.11c shows comparable variations in the solar wind parameters across the shock front. The exception here is the IMF B_z , which is only slightly negative right after the shock arrival. The electron fluxes in the observed L range are barely affected at first. After a few hours, however, the IMF B_z drops drastically to about -20 nT, which coincides with a strong suppression of the electron fluxes across almost all observed L-shells. The last example (Figure 6.11d) displays an event featuring intermediate changes in the solar wind parameters compared to the other events presented here. Nevertheless, the electron fluxes show very little alteration in this case.

The subsequent analysis is aimed to identify parameters governing the radiation belt response to the IP shock passage and to understand the strikingly different responses to seemingly similar solar wind variations. For this purpose, the change of electron fluxes around the shock arrival at different energies is compared to the solar wind dynamic pressure change across the shock front, IMF B_z component, subsolar magnetopause distance and the energy input into the magnetosphere after the shock arrival.

6.2.1 Methodology

To investigate the impact of the IP shock passage, two short time windows are selected just before the shock arrival and just after the shock arrival. The length of the time windows is chosen to be ten hours. Additionally, in order to avoid

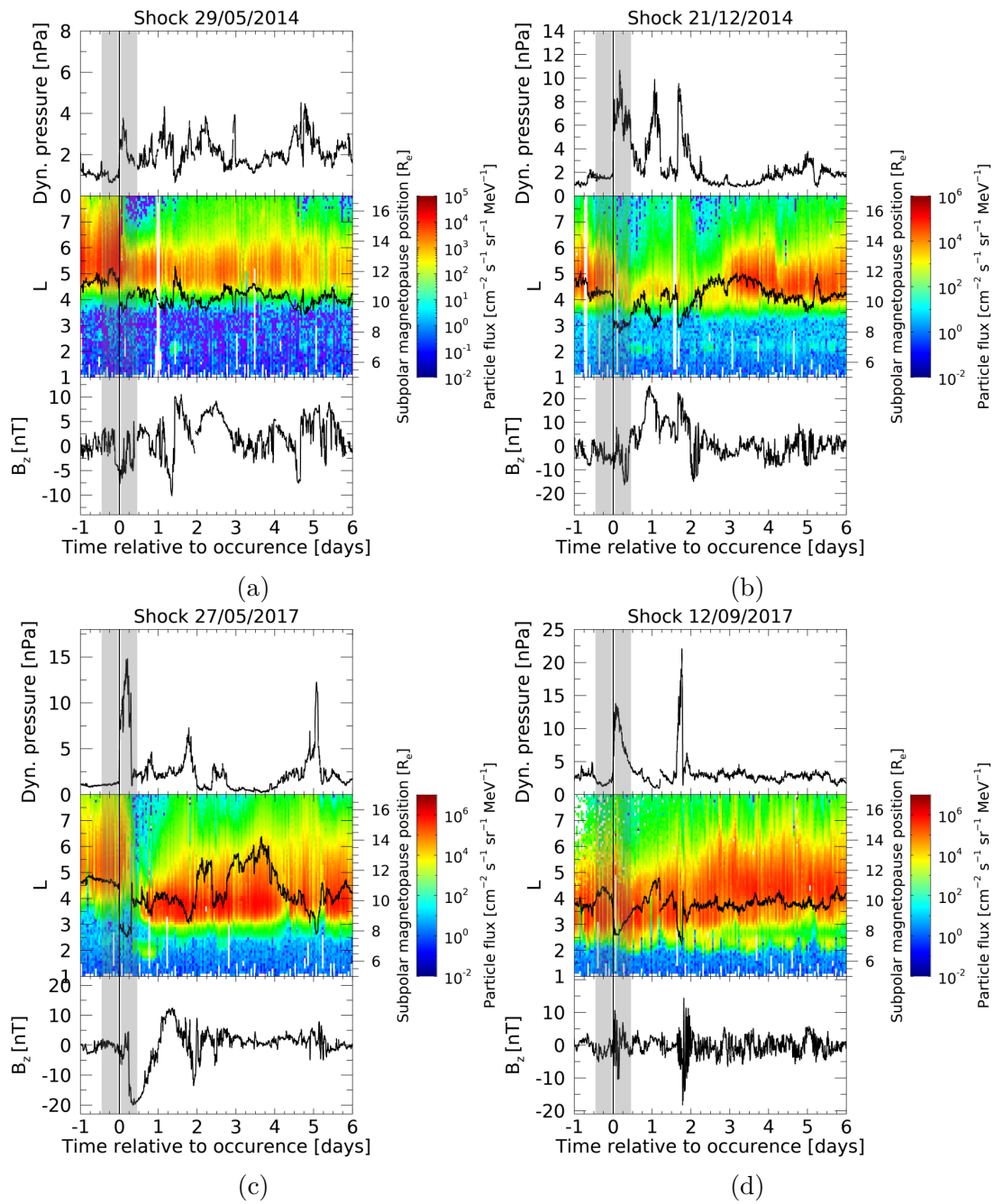


Figure 6.11: Examples of IP shock arrival events showing the solar wind dynamic pressure (top), subsolar magnetopause distance (middle), and IMF B_z (bottom), as well as electron fluxes (colour-coded) as a function of L-shell (middle ordinate) and time relative to the shock arrival in a seven day window starting one day before the shock arrival. The grey boxes mark the time periods used for the subsequent analysis.

possible issues in an exact shock arrival timing, the time intervals are chosen in such a way that they exclude the very time of the shock arrival. Specifically, the pre-shock interval ended one hour before the shock arrival and the post-shock time interval started one hour after the shock arrival. The time window before the shock thus lasted from -11 h to -1 h from the reference point, and the time window after the shock lasted from $+1$ h to $+11$ h from the reference point. These periods are marked with the grey areas in Figure 6.11.

The subsolar magnetopause distance r_0 was calculated according to Equation (2) in Shue et al. [1998]:

$$r_0 = \begin{cases} (11.4 + 0.013B_z)(p)^{-\frac{1}{6.6}}, & \text{for } B_z \geq 0 \\ (11.4 + 0.14B_z)(p)^{-\frac{1}{6.6}}, & \text{for } B_z < 0 \end{cases}, \quad (6.1)$$

where p is the solar wind dynamic pressure in nPa, r_0 is given in Earth radii, and B_z in nT.

The energy input into the magnetosphere E_{in} is calculated according to Equation (13) in Wang et al. [2014]:

$$E_{\text{in}} = 3.78 \cdot 10^7 n_{\text{sw}}^{0.24} v_{\text{sw}}^{1.47} B_{\text{T}}^{0.86} \left[\sin^{2.7} \left(\frac{\Theta}{2} \right) + 0.25 \right], \quad (6.2)$$

where n_{sw} is the solar wind number density in cm^{-3} , v_{sw} the solar wind velocity in km/s, and $B_{\text{T}} = \sqrt{B_x^2 + B_y^2}$ the transverse magnetic field in nT. This equation gives the energy in Watts.

The electron fluxes are averaged in the time windows before (Φ_{b}) and after (Φ_{a}) the shock arrival. The ratio of the fluxes $\Phi_{\text{a}}/\Phi_{\text{b}}$ is then compared to the averaged IMF B_z after the shock, the averaged energy input E_{in} after the shock, the averaged pressure ratio from after and before the shock arrival $p_{\text{a}}/p_{\text{b}}$, and the averaged subsolar magnetopause distance r_0 . This is done separately for all six energy bins and for all L-shells in $0.5 R_{\text{E}}$ bins. An example of the dependences obtained can be viewed in Figure 6.12.

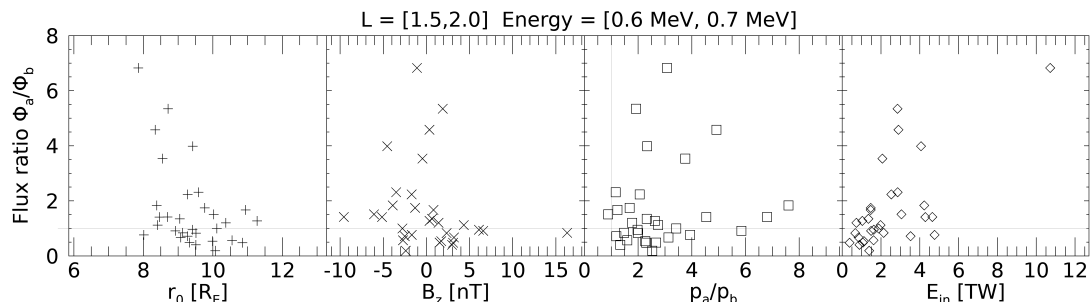


Figure 6.12: An example of the dependences of the electron flux ratio $\Phi_{\text{a}}/\Phi_{\text{b}}$ on (from left to right) the subsolar magnetopause distance r_0 , IMF B_z , the solar wind dynamic pressure ratio $p_{\text{a}}/p_{\text{b}}$, and the energy input E_{in} for L-shells between 1.5 and 2.0, and the energy between 0.6 and 0.7 MeV.

Furthermore, the electron flux ratio is compared to the distance between the subsolar magnetopause r_0 and the McIlwain L-shell, $\text{Dist} = r_0 - L$, and, additionally, split into two subsets depending on the sign of IMF B_z . This is done for

all six energy bins. Figure 6.13 presents two examples, one for negative and one for positive IMF B_z .

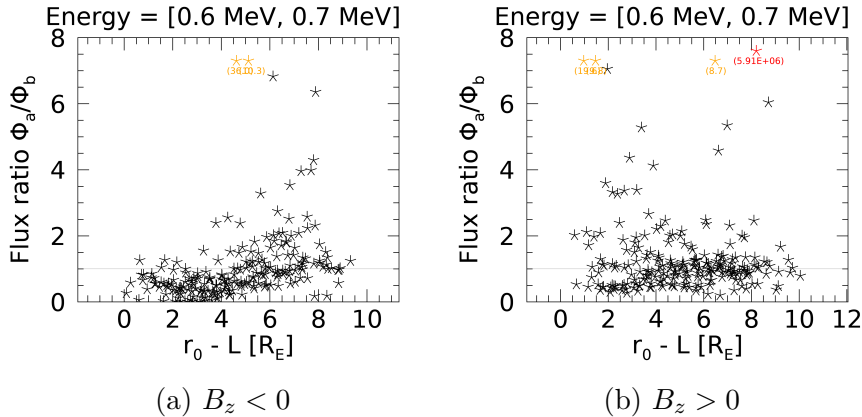


Figure 6.13: Ratio of electron fluxes Φ_a/Φ_b as a function of the distance between the subsolar magnetopause position and the L-shell, $\text{Dist} = r_0 - L$ for (a) negative average IMF B_z after the shock arrival and (b) positive average IMF B_z after the shock arrival. Points that are out of range for this plot are displayed at lower flux ratios, with their actual flux ratio value shown in orange or red. The red colour means that the measured flux before the shock arrival is zero, and it is changed to 10^{-7} particles per ($\text{cm}^2 \text{sr MeV}$) to avoid division by zero.

The last step is to determine the Spearman correlation ρ [Spearman, 1904] for each plot. This provides a non-parametric measure of the rank correlation relationship between two variables. The Spearman correlations are calculated for all four dependences from Figure 6.12 and the two dependences from Figure 6.13, with the addition of the combined data sets for all IMF B_z . The results are presented in the next section.

6.2.2 Results

The Spearman correlation between the IMF B_z after the shock and the ratio of electron fluxes after and before the shock arrival is presented in Figure 6.14. It can be seen that for $L < 4$ there is an anti-correlation, but it is not very strong. For $L > 5$, there is a positive correlation with correlation values $\rho \approx 0.5$, except for the highest energy bin. Figure 6.15 shows the same but for the energy input into the magnetosphere instead of the IMF B_z . There is a moderate positive correlation for $L < 4$ and an anti-correlation (≈ -0.5) for $L > 4$ with a maximum at around $L = 5.5$, except for the highest energy bin. The electron flux ratio shows nearly no correlation with the dynamic pressure ratio, as documented in Figure 6.16. The correlation between the flux ratio and the subsolar magnetopause distance depicted in Figure 6.17 shows only a moderate correlation for $4 < L < 7$.

Figure 6.18 displays the Spearman correlation between the distance Dist between the magnetopause location r_0 and the measurement L-shell, and the ratio of electron fluxes as a function of the EPT instrument data subsets. The correlation is shown for the whole data set as well as for the data subset, where IMF B_z is negative and positive, respectively. It can clearly be seen that, when IMF B_z is positive, there is no correlation between the distance to the magnetopause and

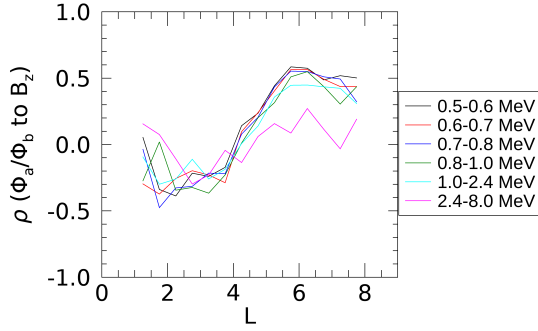


Figure 6.14: Spearman correlation between IMF B_z after the shock and the ratio of electron fluxes as a function of L-shell.

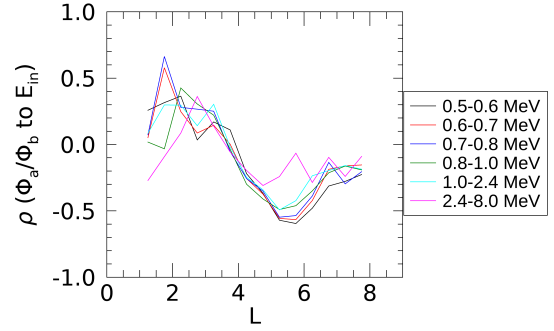


Figure 6.15: Spearman correlation between the energy input into the magnetosphere after the shock and the ratio of electron fluxes as a function of L-shell.

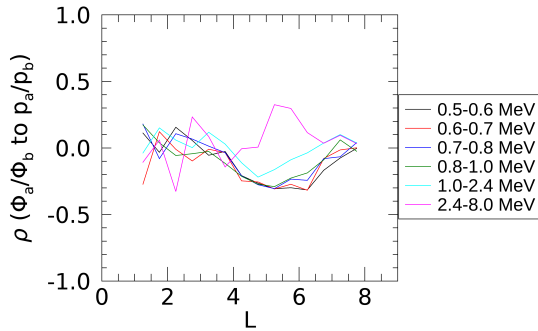


Figure 6.16: Spearman correlation between the ratio of the solar wind dynamic pressure after the shock and the ratio of electron fluxes as a function of L-shell.

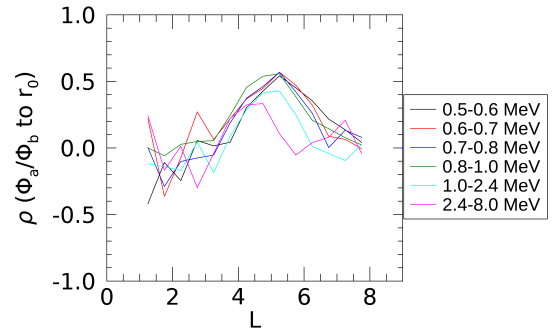


Figure 6.17: Spearman correlation between the subsolar magnetopause distance after the shock and the ratio of electron fluxes as a function of L-shell.

the electron flux ratio. On the other hand, a moderate correlation is obtained for negative IMF B_z . The correlation is weaker for the highest energies measured.

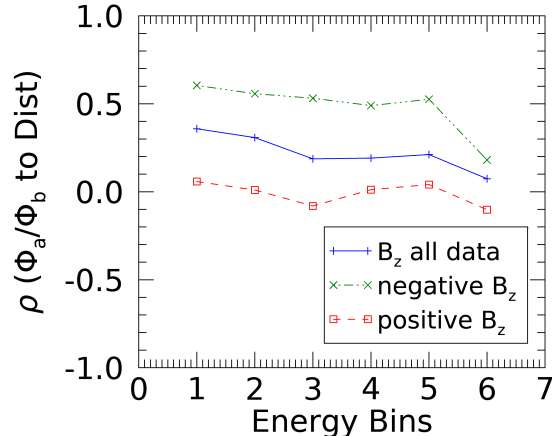


Figure 6.18: Spearman correlation between the distance Dist between the magnetopause location r_0 and the measurement L-shell, and the ratio of electron fluxes as a function of the energy bin (see Table 3.1). The results obtained for the whole data set (blue), for events with average negative IMF B_z after the shock arrival (green), and for events with average positive IMF B_z after the shock arrival (red).

6.3 Discussion of Electron Flux Variations During Geomagnetic Storms and Interplanetary Shock Arrivals

The analysis of the DEMETER data in Section 6.1 is published in Gohl et al. [2021]. Only five storms are found with a Dst minimum below -100 nT and fulfilling the requirement of no other such event in a seven day window starting one day before the Dst minimum. Four of the storms could be sorted into two categories, denoted Type 1 and Type 2 storms. The first type are SN-type storms with high geoeffectiveness. The storms of this type are characterised by rapid changes in selected solar wind parameters, particularly the solar wind speed, number density, and IMF B_z component, shortly before the Dst minimum. The solar wind parameter values tend to return to pre-storm levels relatively quickly. Energy-averaged particle fluxes at $L \geq 3.7$ rise significantly during the SSC phase of the storm, only to drop drastically during the Dst minimum for about half a day before rising again. At this time, energy-averaged fluxes between $2.2 \leq L \leq 4$ increase significantly, while the energy-resolved fluxes reveal an increase at energies above 600 keV in the L-shell range of 2.8 to 3.7. At higher L-shells, the particle fluxes at energies between 600 keV and ≈ 1.4 MeV decrease slightly, while fluxes at higher energies increase. Concurrently, the energy-averaged fluxes decrease overall at this L-range.

The second type of storms only shows increased fluxes during the Dst minimum, with no drop-out of the energy averaged-particle fluxes over the analysed L-shell range. The storms of this type are generally weaker and happen to be S-type storms. Unlike the first storm type, they also do not display a distinct increase in energetic particle fluxes. The variations in the solar wind parameters for these storms are less strong and generally longer lasting. The IMF B_z does not become as negative as for Type 1 storms, but it stays negative for a longer

time.

The fifth storm is interfered by another event only visible in the AE index, which makes it difficult to categorise it in one or the other class. The solar wind parameters are more comparable with the parameters during Type 2 storms, but increased energetic particle fluxes above 1.4 MeV are found about 16 h before the Dst minimum. Given the relatively early appearance of these high energy particles, this might not be directly associated with the geomagnetic storm itself, but potentially with a substorm occurring just before.

Type 1 storms are somewhat comparable with prompt responses to strong IP shock arrivals reported by Foster et al. [2016] and Kanekal and Miyoshi [2021]. In both studies, enhancements of particle energies in the range of L-shells between 3 and 5 have been reported, similar to our results. However, a definite comparison cannot be conducted as measurements of the electric field and/or magnetopause compression are absent.

Other studies were looking at a significantly larger number of several tens of geomagnetic storms with Dst minima below -50 nT. They found the energetic electron fluxes around the Dst minimum to increase for low energy electrons (< 1 MeV), but not for higher energy electrons (e.g., Murphy et al. [2018], Turner et al. [2019]). At high energies, they observed a drop-out rather than an increase. However, they also mentioned that electron fluxes with energies above ≈ 1 MeV are rather unpredictable. Additionally, the enhancement of relativistic electrons only occurs for the strongest storms with a Dst minimum below -180 nT. Given that such storms are relatively rare compared to weaker storms, these cases might average out within a collection of a large number of storms. Further differences can arise from different analysis methods.

Another study was investigating the influence of S-type, SN-type and NS-type (north-to-south type) on the geoeffectiveness [Teh et al., 2015]. They concluded that the type has no significant impact, which is seemingly in contradiction with this work. However, only five storms were investigated in the present study and more storms would need to be investigated to verify this.

Generally, the low number of investigated geomagnetic storms makes it difficult to draw distinct conclusions. Only the investigation of the impenetrable barrier for energetic particles is holistically consistent with former findings [Baker et al., 2014a]. This apparent barrier further tends to shift toward larger L-shells for higher energies, although not by much.

The analysis of how the IP shock passing across the magnetosphere influences electron fluxes in the radiation belts reveal no significant relation to the dynamic pressure changes in the solar wind. Moderate correlations are found for the energy coupling function between the solar wind and Earth's magnetosphere, the subsolar magnetopause distance, and the IMF B_z component. In Figures 6.14 to 6.17, a turning point-like feature can be seen around $L = 4$. This could possibly be interpreted as a difference of the balance between particle gains and losses for $L > 4$ and for $L < 4$. Additionally, all properties seem to have either a maximum or minimum between the L-shells 5 and 6. Furthermore, there are mostly no notable differences between the different energies, with possible exception of the highest energy channel (above 2.4 MeV).

Figure 6.14 shows that, for $L > 4$, IMF B_z has a positive correlation to the flux ratio. In Figure 6.13a, it can be seen that fluxes closest to the magnetopause

tend to decrease, as the fluxes after the shock arrival are often lower than before, while flux ratios are larger and fluxes after are partially larger than before the shock arrival closer to Earth. Figure 6.18 confirms that this is true for all but the highest energy bins for IMF $B_z < 0$. For a positive IMF B_z , no correlation was found. This shows that, for a shock arrival featuring a negative IMF B_z , fluxes above $L \approx 4$ tend to decrease. For $2 < L < 4$, IMF B_z exhibits a weak negative correlation in Figure 6.14, indicating that fluxes in more or less the slot region increase. There is no correlation at the lowest L-shells, indicating that the inner belt is largely unaffected by the IMF B_z .

The energy input (Figure 6.15) below $L \approx 4$ has a mostly positive correlation, indicating an energy increase which goes in line with the aforementioned flux increase. For $L > 4$, the energy input has a negative correlation with the after/before flux ratio, which is the reversed situation, corresponding to the particle losses from the outer L-shells. The subsolar magnetopause distance displays a moderate positive correlation between $4 < L < 7$ in Figure 6.16. This could mean that the fluxes decrease when the magnetopause moves closer to Earth in agreement with the interpretation of the other results presented here. This decrease of particle fluxes at the outer L-shells can be attributed to the magnetopause shadowing.

The correlation between electron flux variations and the negative IMF B_z component has been reported many times already (e.g., Fairfield and Cahill Jr. [1966], Choi et al. [2017], Zhang and Moldwin [2014]). The overall moderate correlations indicate a complex relationship between the solar wind and the radiation belt fluctuations. Links between the sources of faster solar wind [Borovsky and Denton, 2006, Zhang et al., 2007] and the source regions of CMEs [Yurchyshyn et al., 2003] have been found. Differences in the geoeffectiveness of bipolar magnetic clouds were seen between south-to-north or north-to-south orientations. However, the geoeffectiveness was reported to be controlled by the ambient solar wind structure rather than by the polarisation [Kilpua et al., 2012].

Jaynes et al. [2015] showed that the existence of two populations of electrons can be crucial for the energisation of electrons. The source population (tens of keV) gives rise to very low frequency (VLF) waves that, in turn, accelerate the seed population (hundreds of keV) to higher energies. The absence of one of the populations can be a cause for the absence of highly relativistic electrons in the outer belt. The point here is that not only the solar wind conditions are responsible for strong variations in the radiation belt environment, but also the conditions inside the magnetosphere are important at the time of disturbance.

Furthermore, the analysis would benefit from resolving the pitch angle effects and calculating the Roederer L^* instead of the McIlwain L . Particle movements can be tracked more precisely by the proper consideration of the drift shells, which can deviate considerably from the McIlwain L-shells especially for larger L .

Conclusion

This thesis can be split into two parts. The first part (Chapters 4 and 5) is showing the potential of the Timepix device as a particle and flux measurement tool for space applications. The second part (Chapter 6) is about using measurements from low altitude satellites to investigate the variations of radiation belt fluxes during selected space weather phenomena (geomagnetic storms and IP shocks).

A Timepix detector has been successfully operated in space for more than ten years now with the SATRAM module onboard the Proba-V satellite in a LEO orbit. Timepix has the capability to measure charged particles individually. The granularity of the Timepix sensor allows it to register the path of each particle through the sensor. These have to a large extent unique features depending on the particle species allowing their identification.

In this work, methodologies for data analysis have been developed and improved. Based on a basic categorisation of particle species according to their respective recorded track morphology [Holý et al., 2008], a decision tree method (Section 4.2) was developed using the stopping power and cluster height to identify electrons, protons, and heavier ions. Based on this, a NN (Section 4.4) was developed using seven different features of the track morphology to identify electrons and protons. An accuracy of 90.2% was achieved. Electron fluxes can be reproduced quite reasonably, but proton fluxes continue to be an issue. The main reason is that the number of misidentified electrons is of the same order of magnitude as the proton flux itself. Additionally, high energy protons do not deposit much energy and resemble electron tracks for steep impact angles. Ions are, so far, not considered in the NN and they are counted as protons. The extension of the NN by adding a third category is work in progress.

The main advantage of Timepix detectors over the more commonly used radiation monitors and scientific instruments for space is its small size, mass and power consumption. Its largest disadvantages are the lack of spectral information and the large amount of data produced. The latter does not allow SATRAM to work at its full capacity, creating only one to five frames per minute. This is an even bigger problem for the predecessor of Timepix, Timepix3, when operating in data-driven mode. This mode allows to read out every individual particle hit. Registering individual particles is a requirement for more sophisticated particle identification methods, such as the decision tree and the NN. Especially at high fluxes, SATRAM fails to provide sufficiently separated particle tracks rendering both methods unusable. The possibility to use the data-driven mode of Timepix3 would eliminate this issue, albeit at the cost of higher power consumption and the need for more memory onboard the spacecraft.

Another approach to circumvent this problem is the application of onboard processing. At low fluxes, the power and memory space requirements for the aforementioned methods would still be manageable, but at high fluxes, current satellites cannot provide the necessary resources. Therefore, it requires the development of simpler identification methods that sacrifice some of the precision for faster and less power-consuming algorithms. The energy per pixel method (Section 4.3) is a first attempt at that using a more statistical approach. It is a method of estimating the composition of a mixed radiation field, when the

contributing particle species are known. It is using the fact that electrons and protons usually deposit different amounts of energy per pixel. For this method to work efficiently, a high pixel count is required. It is demonstrated that the method is able to identify the proton and electron composition in the SAA and the polar horns in the SATRAM data.

In Section 5.1, the NN is used to determine the number of particles measured in low occupancy frames. For high occupancy frames, a different, more statistical method has to be applied. This method used the average deposited energy of particles depending on the geographical position to estimate the amount of measured particles. With the knowledge of the particle composition of electrons and protons from a nearby low occupancy frame, the number of electrons can be estimated. Using extensive simulations of the detector response, effects of the surrounding shielding, and other correction factors, the electron fluxes are calculated. A comparison with the other particle instrument on the Proba-V satellite (Section 5.2) shows satisfactory results.

Originally, the idea was to use SATRAM data, along with other LEO satellite data, to investigate the variations of particle fluxes in the radiation belts due to geomagnetic and/or solar wind activities after validating the capability of SATRAM to measure these. The capability of SATRAM to measure energetic electron fluxes in space is demonstrated. However, other instruments are still better suited for the task, primarily due to the lack of spectral information and the lower data coverage of SATRAM measurements. Consequently, data from the DEMETER and the EPT instrument are used to study the space weather events.

The first investigation focused on geomagnetic storms during the lifetime of DEMETER (Section 6.1). Five storms are studied, demonstrating that very intense storms (Type 1) ($Dst < -180$ nT) can produce high fluxes with particle energies above 1.4 MeV at $L \geq 3.7$ at the time of the Dst minimum. A similar response can be found in some studies related to shock-induced prompt acceleration of relativistic electrons (e.g., Foster et al. [2016], Kanekal and Miyoshi [2021]), albeit a direct comparison cannot be conducted due to the lack of information on the electric field and the magnetopause distance in our work. Observations of a large number of storms do not show such increase of particle energies over the range of L-shells analysed here (e.g., Murphy et al. [2018], Turner et al. [2019]). The less intense storms (Type 2) do not show such energetic particle fluxes at these L-shells. Additionally, differences in the evolution of fluxes are found. More intense storms would show an increase in fluxes at $L \geq 3.7$ during the SSC phase and then drop during the Dst minimum for half a day before increasing again. At lower L-shell, fluxes increase only around the Dst minimum, not before, and they show no drop-out. This is also the case for less intense storms. However, in this case, fluxes rise around the Dst minimum across all analysed L-shells.

In terms of the solar wind conditions, intense storms are caused by large, sudden changes that relax relatively quickly. Less intense storms resulted from smoother and longer lasting variations in the solar wind. The IMF B_z component shows S-type storms with negative IMF B_z for less intense storms, while intense storms are characterised as SN-type storms with very short periods of negative B_z . This seems to be contradictory to previous findings [Teh et al., 2015], where the type does not determine the geoeffectiveness. However, the number of storms

in this study is too low to draw definite conclusions. The fact that the intense storms are of the SN-type and the less intense storms are of the S-type could be merely a coincidence. Similarly, the occurrence of energetic particle fluxes at higher L-shells could be a rare event. The seemingly conflicting results do not have to be contradictory, as additional solar wind properties may influence the geoeffectiveness. Further research is needed in this case. The impenetrable barrier for ultra-relativistic electrons reported by Baker et al. [2014a] can be confirmed without inconsistency.

The investigation of the influence of IP shocks on the radiation belt electron fluxes (Section 6.2) reveal moderate correlations between the electron flux ratios from before and after the shock arrival and the subsolar magnetopause position, the energy coupling function between the solar wind and the magnetosphere, and the IMF B_z component. Electron fluxes tend to decrease for $L > 4$, roughly corresponding to the outer radiation belt, when the IMF B_z is negative, the energy input increases, and the magnetopause moves closer to Earth. This can be attributed to the effect of magnetopause shadowing.

At L-shells between about 2 to 4, the correlation of the flux ratio to IMF B_z and the energy input is reversed and slightly weaker. This could be interpreted in the way that fluxes increase in the slot region together with an increase of the energy transferred there. The inner belt seems to be largely unaffected by the IP shock arrivals. The correlation between electron flux variations and a negative IMF B_z has been reported before (e.g., Fairfield and Cahill Jr. [1966], Choi et al. [2017], Zhang and Moldwin [2014]).

The variations in the electron fluxes observed in this study, with only moderate correlations revealed, indicate a complex relationship between the solar wind parameter and the radiation belt changes. In addition to the solar wind parameters, the pre-event state of the magnetosphere may have to be favourable to result in significant enhancements of the radiation belt fluxes. Pre-existing electron populations are necessary for the acceleration to highly relativistic energies [Jaynes et al., 2015]. The analysis would further benefit from the calculation of L^* instead of the McIlwain L .

For more conclusive research in this matter, more measurements are necessary. The recent development of the instrumentation for space favours smaller detectors that can operate at smaller satellites, e.g., cubesats. This role can be conveniently fulfilled by detectors of the Timepix family. The successors of Timepix, Timepix2, 3, and 4, have higher resolution and more features. Timepix3 is already space qualified, and new radiation monitors using Timepix3 have been developed. One module, called Hardpix, utilising Timepix3 is already in space onboard the Space Weather Instrumentation, Measurement, Modelling and Risk (SWIMMR) satellite¹. Several other flight opportunities are planned within the following years, including two Hardpix modules onboard the Lunar Gateway station. Another instrument incorporating Timepix3 as a part of a more complex detector, is the Penetrating Particle Analyser (PAN) [Bergmann et al., 2024]. PAN is aimed for measurements of galactic cosmic rays.

Better resolution and more features also mean that more precise methods for particle identification can be developed. Simultaneous measurements of ToT and ToA allow to reconstruct the particle trajectory in 3D [Bergmann et al., 2017,

¹<https://www.ralspace.stfc.ac.uk/Pages/SWIMMR.aspx>

2019b]. A change of the module configuration can also help. The simplest idea would be to put two Timepix detectors in front of each other with an electron filter in between them to easily separate high energy protons from electrons. Low energy protons are distinct from electrons anyway. Proton energies below 50 MeV can be identified in a single layer Timepix by usage of a convolutional neural network [Ruffenach et al., 2019]. The evaluation of proton energies was recently taken further by the method of spectrum deconvolution, which is the decomposition of a complex signal into its contributing spectrum components. In this case, the stopping power spectrum was unfolded. To the best of our knowledge, a proton energy spectrum was measured for the first time with a single layer device in LEO [Bergmann et al., 2024].

Acknowledgements

The author acknowledges the use of the IRBEM library (version 5.0.0b), the latest version of which can be found at <https://doi.org/10.5281/zenodo.6867552>. The author thanks the engineers from CNES and scientific laboratories (CBK, IRAP, LPC2E, LPP, and SSD of ESTEC) who largely contributed to the success of the DEMETER mission. DEMETER data are accessible from the <https://sipad-cdpp.cnes.fr> website (last accessed: 21.07.2021). Furthermore, the OMNI data were obtained from the GSFC/SPDF OMNIWeb interface at <https://omniweb.gsfc.nasa.gov> (last accessed: 21.07.2021).

Bibliography

- ESA Mission overview. https://www.esa.int/Enabling_Support/Space_Engineering_Technology/Proba_Missions/Proba-V_carrying_radiation_detector_from_CERN_to_space. Last Accessed 21 November 2023.
- Belgian Institute for Space Aeronomy - Space Environment Information System (SPENVIS). <https://www.spennis.oma.be/>. Ver.4.6.9, Last Accessed 13 May 2022.
- Timepix picture. https://www.esa.int/ESA_Multimedia/Images/2019/02/Timepix, 2019. Last Accessed 16 October 2023.
- S. Agostinelli, J. Allison, K. Amako, J. Apostolakis, H. Araujo, P. Arce, M. Asai, D. Axen, S. Banerjee, G. Barrand, F. Behner, L. Bellagamba, J. Boudreau, L. Broglia, A. Brunengo, H. Burkhardt, S. Chauvie, J. Chuma, R. Chytracze, G. Cooperman, G. Cosmo, P. Degtyarenko, A. Dell'Acqua, G. Depaola, D. Dietrich, R. Enami, A. Feliciello, C. Ferguson, H. Fesefeldt, G. Folger, F. Foppiano, A. Forti, S. Garelli, S. Giani, R. Giannitrapani, D. Gibin, J.J. Gómez Cadenas, I. González, G. Gracia Abril, G. Greeniaus, W. Greiner, V. Grichine, A. Grossheim, S. Guatelli, P. Gumplinger, R. Hamatsu, K. Hashimoto, H. Hasui, A. Heikkinen, A. Howard, V. Ivanchenko, A. Johnson, F.W. Jones, J. Kallenbach, N. Kanaya, M. Kawabata, Y. Kawabata, M. Kawaguti, S. Kellner, P. Kent, A. Kimura, T. Kodama, R. Kokoulin, M. Kossov, H. Kurashige, E. Lamanna, T. Lampén, V. Lara, V. Lefebvre, F. Lei, M. Liendl, W. Lockman, F. Longo, S. Magni, M. Maire, E. Medernach, K. Minamimoto, P. Mora de Freitas, Y. Morita, K. Murakami, M. Nagamatu, R. Nartallo, P. Nieminen, T. Nishimura, K. Ohtsubo, M. Okamura, S. O'Neale, Y. Oohata, K. Paech, J. Perl, A. Pfeiffer, M.G. Pia, F. Ranjard, A. Rybin, S. Sadilov, E. Di Salvo, G. Santin, T. Sasaki, N. Savvas, Y. Sawada, S. Scherer, S. Sei, V. Sirotenko, D. Smith, N. Starkov, H. Stoecker, J. Sulkimo, M. Takahata, S. Tanaka, E. Tcherniaev, E. Safai Tehrani, M. Tropeano, P. Truscott, H. Uno, L. Urban, P. Urban, M. Verderi, A. Walkden, W. Wander, H. Weber, J.P. Wellisch, T. Wenaus, D.C. Williams, D. Wright, T. Yamada, H. Yoshida, and D. Zschesche. Geant4—a simulation toolkit. *Nucl. Instrum. Methods Phys. Res.*, 506(3): 250–303, 2003. ISSN 0168-9002. doi: [https://doi.org/10.1016/S0168-9002\(03\)01368-8](https://doi.org/10.1016/S0168-9002(03)01368-8).
- S.-I. Akasofu and S. Chapman. The ring current, geomagnetic disturbance, and the Van Allen radiation belts. *J. Geophys. Res.*, 66(5):1321–1350, 1961. doi: <https://doi.org/10.1029/JZ066i005p01321>.
- J. M. Albert, G. P. Ginet, and M. S. Gussenhoven. CRRES observations of radiation belt protons: 1. Data overview and steady state radial diffusion. *J. Geophys. Res.*, 103(A5):9261–9273, 1998. doi: <https://doi.org/10.1029/97JA02869>.
- H. Alfvén. Discussion of the Origin of the Terrestrial and Solar Magnetic Fields. *Tellus*, 2(2):74–82, 1950. doi: <https://doi.org/10.1111/j.2153-3490.1950.tb00315.x>.

- D. N. Baker. Wave-particle interaction effects in the Van Allen belts. *Earth, Planets and Space*, 73(1):189, 2021. doi: <https://doi.org/10.1186/s40623-021-01508-y>.
- D. N. Baker, T. I. Pulkkinen, V. Angelopoulos, W. Baumjohann, and R. L. McPherron. Neutral line model of substorms: Past results and present view. *J. Geophys. Res.*, 101(A6):12975–13010, 1996. doi: <https://doi.org/10.1029/95JA03753>.
- D. N. Baker, S. G. Kanekal, X. Li, S. P. Monk, J. Goldstein, and J. L. Burch. An extreme distortion of the van allen belt arising from the ‘hallowe’en’ solar storm in 2003. *Nat.*, 432(7019):878–818, 2004. doi: <https://doi.org/10.1038/nature03116>.
- D. N. Baker, S. G. Kanekal, V. C. Hoxie, M. G. Henderson, X. Li, H. E. Spence, S. R. Elkington, R. H. W. Friedel, J. Goldstein, M. K. Hudson, G. D. Reeves, R. M. Thorne, C. A. Kletzing, and S. G. Claudepierre. A Long-Lived Relativistic Electron Storage Ring Embedded in Earth’s Outer Van Allen Belt. *Science*, 340(6129):186–190, 2013. doi: <https://doi.org/10.1126/science.1233518>.
- D. N. Baker, A. N. Jaynes, V. C. Hoxie, R. M. Thorne, J. C. Foster, X. Li, J. F. Fennell, J. R. Wygant, S. G. Kanekal, P. J. Erickson, W. Kurth, W. Li, Q. Ma, Q. Schiller, L. Blum, D. M. Malaspina, A. Gerrard, and L. J. Lanzerotti. An impenetrable barrier to ultrarelativistic electrons in the Van Allen radiation belts. *Nat.*, 515:531–534, 2014a. doi: <https://doi.org/10.1038/nature13956>.
- D. N. Baker, A. N. Jaynes, X. Li, M. G. Henderson, S. G. Kanekal, G. D. Reeves, H. E. Spence, S. G. Claudepierre, J. F. Fennell, M. K. Hudson, R. M. Thorne, J. C. Foster, P. J. Erickson, D. M. Malaspina, J. R. Wygant, A. Boyd, C. A. Kletzing, A. Drozdov, and Y. Y. Shprits. Gradual diffusion and punctuated phase space density enhancements of highly relativistic electrons: Van Allen Probes observations. *Geophys. Res. Lett.*, 41(5):1351–1358, 2014b. doi: <https://doi.org/10.1002/2013GL058942>.
- R. Ballabriga, J. Alozy, G. Blaj, M. Campbell, M. Fiederle, E. Frojdh, E. H. M. Heijne, X. Llopart, M. Pichotka, S. Procz, L. Tlustos, and W. Wong. The Medipix3RX: a high resolution, zero dead-time pixel detector readout chip allowing spectroscopic imaging. *J. Instrum.*, 8(02):C02016, 2013. doi: <https://dx.doi.org/10.1088/1748-0221/8/02/C02016>.
- R. Ballabriga, M. Campbell, and X. Llopart. An introduction to the Medipix family ASICs. *Radiat. Meas.*, 136:106271, 2020. ISSN 1350-4487. doi: <https://doi.org/10.1016/j.radmeas.2020.106271>.
- A. Balogh, J. T. Gosling, J. R. Jokipii, R. Kallenbach, and H. Kunow. *Corotating Interaction Region*. Springer Dordrecht, 2000. doi: <https://doi.org/10.1007/978-94-017-1179-1>.
- D. B. Berdichevsky, A. Szabo, R. P. Lepping, A. F. Vi nas, and F. Mariani. Interplanetary fast shocks and associated drivers observed through the 23rd solar minimum by Wind over its first 2.5 years. *J. Geophys. Res.*, 105(A12):27289–27314, 2000. doi: <https://doi.org/10.1029/1999JA000367>.

- B. Bergmann, I. Caicedo, C. Leroy, S. Pospíšil, and Z. Vykydal. ATLAS-TPX: a two-layer pixel detector setup for neutron detection and radiation field characterization. *J. Instrum.*, 11(10):P10002–P10002, 2016. doi: <https://dx.doi.org/10.1088/1748-0221/11/10/P10002>.
- B. Bergmann, M. Pichotka, S. Pospíšil, J. Vycpálek, P. Burian, P. Broulim, and J. Jakůbek. 3D track reconstruction capability of a silicon hybrid active pixel detector. *Eur. Phys. J. C*, 77(6):421, 2017. doi: <https://doi.org/10.1140/epjc/s10052-017-4993-4>.
- B. Bergmann, T. Billoud, C. Leroy, and S. Pospíšil. Characterization of the Radiation Field in the ATLAS Experiment With Timepix Detectors. *IEEE Trans. Nucl. Sci.*, 66(7):1861–1869, 2019a. doi: <https://doi.org/10.1109/TNS.2019.2918365>.
- B. Bergmann, P. Burian, P. Mánek, and S. Pospíšil. 3D reconstruction of particle tracks in a 2 mm thick CdTe hybrid pixel detector. *Eur. Phys. J. C*, 79(2):165, 2019b. doi: <https://doi.org/10.1140/epjc/s10052-019-6673-z>.
- B. Bergmann, B. Acharya, J. Alexandre, P. Beneš, A. Bevan, T. Billoud, H. Branza, P. Burian, M. Campbell, S. Cecchini, Y. M. Cho, M. de Montigny, A. De Roeck, J. R. Ellis, M. M. H. El Sawy, M. Fairbairn, D. Felea, M. Frank, D. Garvey, J. Hays, A. M. Hirt, J. Janeček, M. Kalliokoski, A. Korzenev, D. H. Lacarrère, C. Leroy, G. Levi, A. Lioni, P. Mánek, A. Maulik, A. Margiotta, N. Mauri, N. Mavromatos, L. Meduna, P. Mermod, L. Millward, V. A. Mitsou, I. Ostrovskiy, P.-P. Ouimet, J. Papavassiliou, B. Parker, L. Patrizii, G. Pavalas, J. Pinfold, L. A. Popa, V. Popa, M. Pozzato, S. Pospíšil, A. Rajantie, R. Ruiz de Austri, Z. Sahnoun, M. Sakellariadou, A. Santra, S. Sarkar, G. W. Semenoff, A. Shaa, G. Sirri, K. Sliwa, P. Smolyanskiy, R. Soluk, M. Spurio, M. Staelens, M. Suk, M. Tenti, V. Togo, J. A. Tuszyński, A. Upreti, V. Vento, O. M. Vives García, A. Wall, and E. White. Timepix3 as solid-state time-projection chamber in particle and nuclear physics. *PoS, ICHEP2020*:720. 8 p, 2021. doi: <https://doi.org/10.22323/1.390.0720>.
- B. Bergmann, St. Gohl, D. Garvey, J. Jelínek, and P. Smolyanskiy. Results and Perspectives of Timepix Detectors in Space—From Radiation Monitoring in Low Earth Orbit to Astroparticle Physics. *Instruments*, 8(1), 2024. ISSN 2410-390X. doi: <https://doi.org/10.3390/instruments8010017>.
- L. Biermann. Kometenschweife und solare Korpuskularstrahlung. *Z. Astrophys.*, 29(3):274–286, 1951.
- L. Biermann. Über den Schweif des Kometen Halley im Jahre 1910. *Z. Naturforsch.*, 7(1):127–136, 1952. doi: <https://doi.org/10.1515/zna-1952-0122>.
- K. Birkeland and J. Muir. *On the Cause of Magnetic Storms and the Origin of Terrestrial Magnetism*. Number dıl 2 in *On the Cause of Magnetic Storms and the Origin of Terrestrial Magnetism*. H. Aschehoug & Company, 1908.

- L. W. Blum, A. Koval, I. G. Richardson, L. B. Wilson, D. Malaspina, A. Greeley, and A. N. Jaynes. Prompt Response of the Dayside Magnetosphere to Discrete Structures Within the Sheath Region of a Coronal Mass Ejection. *Geophys. Res. Lett.*, 48(11):e2021GL092700, 2021. doi: <https://doi.org/10.1029/2021GL092700>.
- L.W. Blum, A. Artemyev, O. Agapitov, D. Mourenas, S. Boardsen, and Q. Schiller. EMIC Wave-Driven Bounce Resonance Scattering of Energetic Electrons in the Inner Magnetosphere. *J. Geophys. Res.*, 124(4):2484–2496, 2019. doi: <https://doi.org/10.1029/2018JA026427>.
- R.N. Borojev and M.S. Vasiliev. Relationship of the ASY-H index with interplanetary medium parameters and auroral activity in magnetic storm main phases during CIR and ICME events. *Sol.-Terr. Phys.*, 6:35–40, 2020. doi: <https://doi.org/10.12737/stp-61202004>.
- J. E. Borovsky and M. H. Denton. Differences between CME-driven storms and CIR-driven storms. *J. Geophys. Res.*, 111(A7), 2006. doi: <https://doi.org/10.1029/2005JA011447>.
- J. Bortnik, R. M. Thorne, and N. P. Meredith. Plasmaspheric hiss overview and relation to chorus. *J. Atmos. Sol.-Terr. Phys.*, 71(16):1636–1646, 2009. ISSN 1364-6826. doi: <https://doi.org/10.1016/j.jastp.2009.03.023>.
- J. Bouchami, A. Gutiérrez, A. Houdayer, J. Idárraga, J. Jakubek, C. Lebel, C. Leroy, J.-P. Martin, M. Platkevič, and S. Pospíšil. Study of charge sharing in a silicon pixel detector with heavy ionizing particles interacting with a Medipix2 device. *Nucl. Instrum. Methods Phys. Res.*, 607(1):196–198, 2009. ISSN 0168-9002. doi: <https://doi.org/10.1016/j.nima.2009.03.147>. Radiation Imaging Detectors 2008.
- L. F. Burlaga. *Interplanetary Magnetohydrodynamics*, volume 3. Oxford University Press, 1995.
- R. K. Burton, R. L. McPherron, and C. T. Russell. An empirical relationship between interplanetary conditions and Dst. *J. Geophys. Res.*, 80(31):4204–4214, 1975. doi: <https://doi.org/10.1029/JA080i031p04204>.
- A. P. H. Butler, N. G. Anderson, R. Tipples, N. Cook, R. Watts, J. Meyer, A. J. Bell, T. R. Melzer, and P. H. Butler. Bio-medical X-ray imaging with spectroscopic pixel detectors. *Nucl. Instr. Methods Phys. Res.*, 591(1):141–146, 2008. ISSN 0168-9002. doi: <https://doi.org/10.1016/j.nima.2008.03.039>.
- M. Campbell, E.H.M. Heijne, G. Meddeler, E. Pernigotti, and W. Snoeys. A readout chip for a 64×64 pixel matrix with 15-bit single photon counting. *IEEE Trans. Nucl. Sci.*, 45(3):751–753, 1998. doi: <https://doi.org/10.1109/23.682629>.
- M. Campbell, E. Heijne, T. Holý, J. Idárraga, J. Jakubek, C. Lebel, C. Leroy, X. Llopart, S. S. Pospíšil, L. Tlustos, and Z. Vykydal. Study of the charge sharing in a silicon pixel detector by means of α -particles interacting with a Medipix2 device. *Nucl. Instrum. Methods Phys. Res.*, 591(1):38–41, 2008.

ISSN 0168-9002. doi: <https://doi.org/10.1016/j.nima.2008.03.096>. Radiation Imaging Detectors 2007.

- C. Cattell, A. Breneman, C. Colpitts, J. Dombek, S. Thaller, S. Tian, J. Wygant, J. Fennell, M. K. Hudson, R. Ergun, C. T. Russell, R. Torbert, P.-A. Lindqvist, and J. Burch. Dayside response of the magnetosphere to a small shock compression: Van Allen Probes, Magnetospheric MultiScale, and GOES-13. *Geophys. Res. Lett.*, 44(17):8712–8720, 2017. doi: <https://doi.org/10.1002/2017GL074895>.
- S. Chapman and V. C. A. Ferraro. A new theory of magnetic storms. *Terr. Magn. Atmos. Electr.*, 36(3):171–186, 1931. doi: <https://doi.org/10.1029/TE036i003p00171>.
- P. F. Chen. Coronal Mass Ejections: Models and Their Observational Basis. *Living Rev. Sol. Phys.*, 8, 2011. doi: <https://doi.org/10.12942/lrsp-2011-1>.
- K.-E. Choi, D.-Y. Lee, K.-C. Choi, and J. Kim. Statistical properties and geoeffectiveness of southward interplanetary magnetic field with emphasis on weakly southward Bz events. *J. Geophys. Res.*, 122(5):4921–4934, 2017. doi: <https://doi.org/10.1002/2016JA023836>.
- S. G. Claudepierre, Q. Ma, J. Bortnik, T. P. O’Brien, J. F. Fennell, and J. B. Blake. Empirically Estimated Electron Lifetimes in the Earth’s Radiation Belts: Van Allen Probe Observations. *Geophys. Res. Lett.*, 47(3):e2019GL086053, 2020. doi: <https://doi.org/10.1029/2019GL086053>.
- S. R. Cranmer, S. E. Gibson, and P. Riley. Origins of the Ambient Solar Wind: Implications for Space Weather. *Space Sci. Rev.*, 212:1345–1384, 2017. doi: <https://doi.org/10.1007/s11214-017-0416-y>.
- T. Cussac, M.-A. Clair, P. Ultré-Guerard, F. Buisson, G. Lassalle-Balier, M. Ledu, C. Elisabelar, X. Passot, and N. Rey. The Demeter microsatellite and ground segment. *Planet. Space Sci.*, 54(5):413–427, 2006. ISSN 0032-0633. doi: <https://doi.org/10.1016/j.pss.2005.10.013>.
- M. Cyamukungu, S. Benck, S. Borisov, G. Grégoire, J. Cabrera, J.-L. Bonnet, B. Desoete, F. Preud’homme, C. Semaille, G. Creve, J. De Saedeleer, S. Ilse, L. De Busser, V. Pierrard, S. Bonnewijn, J. Maes, E. Van Ransbeeck, E. Neefs, J. Lemaire, E. Valtonen, R. Punkkinen, M. Anciaux, K. Litefti, N. Brun, D. Pauwels, C. Quevrin, D. Moreau, A. Helderweirt, W. Hajdas, and P. Nieminen. The Energetic Particle Telescope (EPT) on Board PROBA-V: Description of a New Science-Class Instrument for Particle Detection in Space. *IEEE Trans. Nucl. Sci.*, 61(6):3667–3681, 2014. doi: <https://doi.org/10.1109/TNS.2014.2361955>.
- N. T. Davis and M. Sugiura. Auroral electrojet activity index AE and its universal time variation. *J. Geophys. Res.*, 71(3):785–801, 1966. doi: <https://doi.org/10.1029/JZ071i003p00785>.

- P. De Michelis, I. A. Daglis, and G. Consolini. An average image of proton plasma pressure and of current systems in the equatorial plane derived from AMPTE/CCE-CHEM measurements. *J. Geophys. Res.*, 104(A12):28615–28624, 1999. doi: <https://doi.org/10.1029/1999JA900310>.
- L. Desorgher, W. Hajdas, I. Britvitch, K. Egli, X. Guo, Y. Luo, F. Chastellain, C. Pereira, R. Muff, D. Boscher, G. Maehlum, and D. Meier. The Next Generation Radiation Monitor – NGRM. In *2013 IEEE Nuclear Science Symposium and Medical Imaging Conference (2013 NSS/MIC)*, pages 1–6, 2013. doi: <https://doi.org/10.1109/NSSMIC.2013.6829497>.
- A. Y. Drozdov, N. Aseev, F. Effenberger, D. L. Turner, A. Saikin, and Y. Y. Shprits. Storm Time Depletions of Multi-MeV Radiation Belt Electrons Observed at Different Pitch Angles. *J. Geophys. Res.*, 124(11):8943–8953, 2019. doi: <https://doi.org/10.1029/2019JA027332>.
- O. V. Dudnik, J. Sylwester, M. Kowaliński, P. Podgórski, and K. J. H. Phillips. Detection of the third innermost radiation belt on LEO CORONAS-Photon satellite around 2009 solar minimum. *Adv. Space Res.*, 70(5):1441–1452, 2022. ISSN 0273-1177. doi: <https://doi.org/10.1016/j.asr.2022.06.031>.
- J. W. Dungey. Interplanetary Magnetic Field and the Auroral Zones. *Phys. Rev. Lett.*, 6:47–48, 1961. doi: <https://doi.org/10.1103/PhysRevLett.6.47>.
- J. W. Dungey. The structure of the exosphere, or Adventures in velocity space. *Geophysics, The Earth's Environment*, 1963.
- M. W. Dunlop and A. Balogh. Magnetopause current as seen by Cluster. *Ann. Geophys.*, 23(3):901–907, 2005. doi: <https://doi.org/10.5194/angeo-23-901-2005>.
- T. E. Eastman, E. W. Hones Jr., S. J. Bame, and J. R. Asbridge. The magnetospheric boundary layer: Site of plasma, momentum and energy transfer from the magnetosheath into the magnetosphere. *Geophys. Res. Lett.*, 3(11):685–688, 1976. doi: <https://doi.org/10.1029/GL003i011p00685>.
- A. Egeland and W. J. Burke. The ring current: a short biography. *History of Geo- and Space Sciences*, 3(2):131–142, 2012. doi: <https://doi.org/10.5194/hgss-3-131-2012>.
- S. R. Elkington, M. K. Hudson, and A. A. Chan. Acceleration of relativistic electrons via drift-resonant interaction with toroidal-mode Pc-5 ULF oscillations. *Geophys. Res. Lett.*, 26(21):3273–3276, 1999. doi: <https://doi.org/10.1029/1999GL003659>.
- D. H. Fairfield and L. J. Cahill Jr. Transition region magnetic field and polar magnetic disturbances. *J. Geophys. Res.*, 71(1):155–169, 1966. doi: <https://doi.org/10.1029/JZ071i001p00155>.
- C.-G. Fälthammar. Effects of time-dependent electric fields on geomagnetically trapped radiation. *J. Geophys. Res.*, 70(11):2503–2516, 1965. doi: <https://doi.org/10.1029/JZ070i011p02503>.

- C.-G. Fälthammar. On the transport of trapped particles in the outer magnetosphere. *J. Geophys. Res.*, 71(5):1487–1491, 1966. doi: <https://doi.org/10.1029/JZ071i005p01487>.
- J. F. Fennell, J. L. Roeder, W. S. Kurth, M. G. Henderson, B. A. Larsen, G. Hospodarsky, J. R. Wygant, J. S. G. Claudepierre, J. B. Blake, H. E. Spence, J. H. Clemmons, H. O. Funsten, C. A. Kletzing, and G. D. Reeves. Van Allen Probes observations of direct wave-particle interactions. *Geophys. Res. Lett.*, 41(6):1869–1875, 2014. doi: <https://doi.org/10.1002/2013GL059165>.
- R. Fitzpatrick. Plasma Physics. <https://farside.ph.utexas.edu/teaching/plasma/lectures1/node14.html>, 2021. Lecture at the University of Texas at Austin; [Online, accessed 13 January 2024].
- M.-C. Fok and T.-E. Moore. *Drift-Shell Splitting in an Asymmetric Magnetic Field*, pages 327–331. American Geophysical Union (AGU), 1998. ISBN 9781118664162. doi: <https://doi.org/10.1029/GM104p0327>.
- J. C. Foster, J. R. Wygant, M. K. Hudson, A. J. Boyd, D. N. Baker, P. J. Erickson, and H. E. Spence. Shock-induced prompt relativistic electron acceleration in the inner magnetosphere. *J. Geophys. Res.*, 120(3):1661–1674, 2015. doi: <https://doi.org/10.1002/2014JA020642>.
- J. C. Foster, P. J. Erickson, D. N. Baker, A. N. Jaynes, E. V. Mishin, J. F. Fennel, X. Li, M. G. Henderson, and S. G. Kanekal. Observations of the impenetrable barrier, the plasmopause, and the VLF bubble during the 17 March 2015 storm. *J. Geophys. Res.*, 121(6):5537–5548, 2016. doi: <https://doi.org/10.1002/2016JA022509>.
- M. Francois, S. Santandrea, K. Mellab, D. Vrancken, and J. Versluys. The PROBA-V mission: the space segment. *Int. J. Remote Sens.*, 35(7):2548–2564, 2014. doi: <https://doi.org/10.1080/01431161.2014.883098>.
- S. A. Fuselier, D. M. Klumpar, E. G. Shelley, B. J. Anderson, and A. J. Coates. He²⁺ and H⁺ dynamics in the subsolar magnetosheath and plasma depletion layer. *J. Geophys. Res.*, 96(A12):21095–21104, 1991. doi: <https://doi.org/10.1029/91JA02145>.
- N. Yu. Ganushkina, M. W. Liemohn, and S. Dubyagin. Current Systems in the Earth’s Magnetosphere. *Rev. Geophys.*, 56(2):309–332, 2018. doi: <https://doi.org/10.1002/2017RG000590>.
- E. Gatti, A. Longoni, P. Rehak, and M. Sampietro. Dynamics of electrons in drift detectors. *Nucl. Instrum. Methods Phys. Res.*, 253(3):393–399, 1987. ISSN 0168-9002. doi: [https://doi.org/10.1016/0168-9002\(87\)90522-5](https://doi.org/10.1016/0168-9002(87)90522-5).
- M. Gedalin, A. P. Dimmock, C. T. Russell, N. V. Pogorelov, and V. Roytershteyn. Role of the overshoot in the shock self-organization. *J. Plasma Phys.*, 89(2): 905890201, 2023. doi: <https://doi.org/10.1017/S0022377823000090>.

- R. G. Giovanelli. Magnetic and Electric Phenomena in the Sun's Atmosphere associated with Sunspots. *Monthly Notices of the Royal Astronomical Society*, 107(4):338–355, 1947. ISSN 0035-8711. doi: <https://doi.org/10.1093/mnras/107.4.338>.
- St. Gohl, B. Bergmann, C. Granja, A. Owens, M. Pichotka, S. Polanský, and S. Pospíšil. Measurement of particle directions in low earth orbit with a Timepix. *J. Instrum.*, 11(11):C11023, 2016. doi: <https://dx.doi.org/10.1088/1748-0221/11/11/C11023>.
- St. Gohl, B. Bergmann, H. Evans, P. Nieminen, A. Owens, and S. Pospíšil. Study of the radiation fields in LEO with the Space Application of Timepix Radiation Monitor (SATRAM). *Adv. Space Res.*, 63(5):1646–1660, 2019. ISSN 0273-1177. doi: <https://doi.org/10.1016/j.asr.2018.11.016>.
- St. Gohl, F. Němec, and M. Parrot. Variations in Energetic Particle Fluxes around Significant Geomagnetic Storms Observed by the Low-Altitude DEMETER Spacecraft. *Universe*, 7(8):260, 2021. doi: <https://doi.org/10.3390/universe7080260>.
- St. Gohl, M. Malich, B. Bergmann, P. Burian, C. Granja, E. Heijne, M. Holík, J. Jacůbek, J. Janeček, L. Marek, C. Oancea, M. Petro, S. Pospíšil, A. Smetana, P. Soukup, D. Tureček, and M. Vuolo. A miniaturized radiation monitor for continuous dosimetry and particle identification in space. *J. Instrum.*, 17(01):C01066, 2022. doi: <https://dx.doi.org/10.1088/1748-0221/17/01/C01066>.
- St. Gohl, B. Bergmann, M. Kaplan, and F. Němec. Measurement of electron fluxes in a Low Earth Orbit with SATRAM and comparison to EPT data. *Adv. Space Res.*, 72(6):2362–2376, 2023. ISSN 0273-1177. doi: <https://doi.org/10.1016/j.asr.2023.05.033>.
- W. D. Gonzalez and B. T. Tsurutani. Criteria of interplanetary parameters causing intense magnetic storms ($Dst < -100$ nT). *Planet. Space Sci.*, 35(9):1101–1109, 1987. ISSN 0032-0633. doi: [https://doi.org/10.1016/0032-0633\(87\)90015-8](https://doi.org/10.1016/0032-0633(87)90015-8).
- C. Granja, S. Polanský, Z. Vykydal, S. Pospíšil, A. Owens, Z. Kozáček, K. Mellab, and M. Simcak. The SATRAM Timepix spacecraft payload in open space on board the PROBA-V satellite for wide range radiation monitoring in LEO orbit. *Planet. Space Sci.*, 125:114–129, 2016. ISSN 0032-0633. doi: <https://doi.org/10.1016/j.pss.2016.03.009>.
- A. D. Greeley, S. G. Kanekal, Q. Schiller, L. Blum, A. Halford, K. Murphy, T. Raita, and D. N. Baker. Persistent Pitch Angle Anisotropies of Relativistic Electrons in the Outer Radiation Belts. *J. Geophys. Res.*, 129(1):e2023JA031549, 2024. doi: <https://doi.org/10.1029/2023JA031549>.
- M. Gruntman. Energetic neutral atom imaging of space plasmas. *Rev. Sci. Instrum.*, 68(10):3617–3656, 1997. ISSN 0034-6748. doi: <https://doi.org/10.1063/1.1148389>.

- X. Gu, S. Xia, S. Fu, Z. Xiang, B. Ni, J. Guo, and X. Cao. Dynamic Responses of Radiation Belt Electron Fluxes to Magnetic Storms and their Correlations with Magnetospheric Plasma Wave Activities. *Astrophys. J.*, 891(2):127, 2020. doi: 10.3847/1538-4357/ab71fc.
- D. A. Gurnett and A. Bhattacharjee. *Introduction to Plasma Physics: With Space, Laboratory and Astrophysical Applications*. Cambridge University Press, 2 edition, 2017. doi: <https://doi.org/10.1017/9781139226059>.
- C. Hahn, G. Weber, R. Martin, S. Höfer, T. Kämpfer, and Th. Stöhlker. CdTe Timepix detectors for single-photon spectroscopy and linear polarimetry of high-flux hard X-ray radiation. *Rev. Sci. Instr.*, 87(4):043106, 2016. ISSN 0034-6748. doi: <https://doi.org/10.1063/1.4945362>.
- A. J. Halford, S. L. McGregor, K. R. Murphy, R. M. Millan, M. K. Hudson, L. A. Woodger, C. A. Cattel, A. W. Breneman, I. R. Mann, W. S. Kurth, G. B. Hospodarsky, M. Gkioulidou, and J. F. Fennell. BARREL observations of an ICME-shock impact with the magnetosphere and the resultant radiation belt electron loss. *J. Geophys. Res.*, 120(4):2557–2570, 2015. doi: <https://doi.org/10.1002/2014JA020873>.
- Y. X. Hao, Q.-G. Zong, X.-Z. Zhou, S. Y. Fu, R. Rankin, C.-J. Yuan, A. T. Y. Lui, H. E. Spence, J. B. Blake, D. N. Baker, and G. D. Reeves. Electron dropout echoes induced by interplanetary shock: Van Allen Probes observations. *Geophys. Res. Lett.*, 43(11):5597–5605, 2016. doi: <https://doi.org/10.1002/2016GL069140>.
- T. Holý, E. Heijne, J. Jakubek, S. Pospíšil, J. Uher, and Z. Vykydal. Pattern recognition of tracks induced by individual quanta of ionizing radiation in Medipix2 silicon detector. *Nucl. Instrum. Methods Phys. Res.*, 591(1):287–290, 2008. ISSN 0168-9002. doi: <https://doi.org/10.1016/j.nima.2008.03.074>. Radiation Imaging Detectors 2007.
- E. W. Hones. Transient phenomena in the magnetotail and their relation to substorms. *Space Sci. Rev.*, 23(3):393–410, 1979. doi: <https://doi.org/10.1007/BF00172247>.
- G. Hulot, C. C. Finlay, C. G. Constable, N. Olsen, and M. Manda. The Magnetic Field of Planet Earth. *Space Sci. Rev.*, 152(1):159–222, 2010. doi: <http://dx.doi.org/10.1007/s11214-010-9644-0>.
- S. O. Ifedili. Solar neutron decay injection of protons into the radiation belt. *Sol. Phys.*, 171(2), 1997. doi: <https://doi.org/10.1023/A:1004968731799>.
- T. Iijima and T. A. Potemra. The amplitude distribution of field-aligned currents at northern high latitudes observed by Triad. *J. Geophys. Res.*, 81(13):2165–2174, 1976. doi: <https://doi.org/10.1029/JA081i013p02165>.
- T. Iyemori, T. Araki, T. Kamei, and M. Takeda. Mid-latitude geomagnetic indices ASY and SYM (Provisinial). Technical Report 10, Kyoto University, 2000. Kyoto.

- J. Jakubek. Precise energy calibration of pixel detector working in time-over-threshold mode. *Nucl. Instrum. Methods Phys. Res.*, 633:S262–S266, 2011. ISSN 0168-9002. doi: <https://doi.org/10.1016/j.nima.2010.06.183>. 11th International Workshop on Radiation Imaging Detectors (IWORID).
- A. N. Jaynes, D. N. Baker, H. J. Singer, J. V. Rodriguez, T. M. Loto'aniu, A. F. Ali, S. R. Elkington, X. Li, S. G. Kanekal, S. G. Claudepierre, J. F. Fennell, W. Li, R. M. Thorne, C. A. Kletzing, H. E. Spence, and G. D. Reeves. Source and seed populations for relativistic electrons: Their roles in radiation belt changes. *J. Geophys. Res.*, 120(9):7240–7254, 2015. doi: <https://doi.org/10.1002/2015JA021234>.
- L. Jian. Stream Interaction Regions (SIRs) from WIND and ACE Data during 1995 - 2009. http://www.srl.caltech.edu/ACE/ASC/DATA/level3/SIR_List_1995_2009_Jian.pdf, 2021a. [Online, accessed 7-June-2021].
- L. Jian. Interplanetary Coronal Mass Ejections (ICMEs) from Wind and ACE Data during 1995 - 2009. http://www.srl.caltech.edu/ACE/ASC/DATA/level3/ICME_List_1995_2009_Jian.pdf, 2021b. [Online, accessed 7 June 2021].
- L. Jian, C. T. Russell, J. G. Luhmann, and R. M. Skoug. Properties of Interplanetary Coronal Mass Ejections at One AU During 1995 – 2004. *Sol. Phys.*, 239:393–436, 2006. doi: <https://doi.org/10.1007/s11207-006-0133-2>.
- W. R. Johnston, T. P. O'Brien, G. P. Ginet, S. L. Huston, T. B. Guild, and J. A. Fennelly. AE9/AP9/SPM: new models for radiation belt and space plasma specification. In Khanh D. Pham and Joseph L. Cox, editors, *Sensors and Systems for Space Applications VII*, volume 9085, page 908508. International Society for Optics and Photonics, SPIE, 2014. doi: 10.1117/12.2049836.
- W. R. Johnston, T. P. O'Brien, S. L. Huston, T. B. Guild, and G. P. Ginet. Recent Updates to the AE9/AP9/SPM Radiation Belt and Space Plasma Specification Model. *IEEE Trans. Nucl. Sci.*, 62(6):2760–2766, 2015. doi: <https://doi.org/10.1109/TNS.2015.2476470>.
- V. K. Jordanova, M. Spasojevic, and M. F. Thomsen. Modeling the electromagnetic ion cyclotron wave-induced formation of detached subauroral proton arcs. *J. Geophys. Res.*, 112(A8), 2007. doi: <https://doi.org/10.1029/2006JA012215>.
- S. Jurac, J. C. Kasper, J.D. Richardson, and A. J. Lazarus. Geomagnetic disturbances and their relationship to Interplanetary shock parameters. *Geophys. Res. Lett.*, 29(10):101–1–101–4, 2002. doi: <https://doi.org/10.1029/2001GL014034>.
- M. M. H. Kalliokoski, E. K. J. Kilpua, A. Osmane, D. L. Turner, A. N. Jaynes, L. Turc, H. George, and M. Palmroth. Outer radiation belt and inner magnetospheric response to sheath regions of coronal mass ejections: a statistical analysis. *Ann. Geophys.*, 38(3):683–701, 2020. doi: <https://doi.org/10.5194/angeo-38-683-2020>.

- Y. Kamide. Association of DP and DR fields with the interplanetary magnetic field variation. *J. Geophys. Res.*, 79(1):49–55, 1974. doi: <https://doi.org/10.1029/JA079i001p00049>.
- S. Kanekal and Y. Miyoshi. Dynamics of the terrestrial radiation belts: a review of recent results during the VarSITI (Variability of the Sun and Its Terrestrial Impact) era, 2014–2018. *Prog. Earth Planet. Sci.*, 8:35, 2021. doi: <https://doi.org/10.1186/s40645-021-00413-y>.
- S. G. Kanekal, D. N. Baker, J. F. Fennell, A. Jones, Q. Schiller, I. G. Richardson, X. Li, D. L. Turner, S. Califf, S. G. Claudepierre, L. B. Wilson III, A. Jaynes, J. B. Blake, G. D. Reeves, H. E. Spence, C. A. Kletzing, and J. R. Wygant. Prompt acceleration of magnetospheric electrons to ultrarelativistic energies by the 17 March 2015 interplanetary shock. *J. Geophys. Res.*, 121(8):7622–7635, 2016. doi: <https://doi.org/10.1002/2016JA022596>.
- T. Karlsson, A. Kullen, E. Liljeblad, N. Brenning, H. Nilsson, H. Gunell, and M. Hamrin. On the origin of magnetosheath plasmoids and their relation to magnetosheath jets. *J. Geophys. Res.*, 120(9):7390–7403, 2015. doi: <https://doi.org/10.1002/2015JA021487>.
- L. Kepko, R. L. McPherron, O. Amm, S. Apatenkov, W. Baumjohann, J. Birn, M. Lester, R. Nakamura, T. I. Pulkkinen, and V. Sergeev. Substorm Current Wedge Revisited. *Space Sci. Rev.*, 190(1):1–46, 2015. ISSN 1572-9672. doi: <https://doi.org/10.1007/s11214-014-0124-9>.
- E. K. J. Kilpua, Y. Li, J. G. Luhmann, L. K. Jian, and C. T. Russell. On the relationship between magnetic cloud field polarity and geoeffectiveness. *Ann. Geophys.*, 30(7):1037–1050, 2012. doi: <https://doi.org/10.5194/angeo-30-1037-2012>.
- E. K. J. Kilpua, H. Hietala, D. L. Turner, H. E. J. Koskinen, T. I. Pulkkinen, J. V. Rodriguez, G. D. Reeves, S. G. Claudepierre, and H. E. Spence. Unraveling the drivers of the storm time radiation belt response. *Geophys. Res. Lett.*, 42(9):3076–3084, 2015. doi: <https://doi.org/10.1002/2015GL063542>.
- E. K. J. Kilpua, H. E. J. Koskinen, and T. I. Pulkkinen. Coronal mass ejections and their sheath regions in interplanetary space. *Living Rev. Sol. Phys.*, 14(1), 2017. doi: <https://doi.org/10.1007/s41116-017-0009-6>.
- E. K. J. Kilpua, D. L. Turner, A. N. Jaynes, H. Hietala, H. E. J. Koskinen, A. Osmane, M. Palmroth, T. I. Pulkkinen, R. Vainio, D. Baker, and S. G. Claudepierre. Outer Van Allen Radiation Belt Response to Interacting Interplanetary Coronal Mass Ejections. *J. Geophys. Res.*, 124(3):1927–1947, 2019. doi: <https://doi.org/10.1029/2018JA026238>.
- J. H. King and N. E. Papitashvili. Solar Wind Spatial Scales in and Comparisons of Hourly WIND and ACE Plasma and Magnetic Field Data. *J. Geophys. Res.*, 110(A2), 2005. doi: <https://doi.org/10.1029/2004JA010649>.
- M. G. Kivelson and C. T. Russell. *Introduction to Space Physics*. Cambridge University Press, 1995. doi: <https://doi.org/10.1017/9781139878296>.

- . E. J. Koskinen and E. K. J. Kilpua. *Dynamics of the Electron Belts*, pages 213–240. Springer International Publishing, Cham, 2022. ISBN 978-3-030-82167-8. doi: https://doi.org/10.1007/978-3-030-82167-8_7.
- A. S. Kovtyukh. Ion Composition of the Earth’s Radiation Belts in the Range from 100 keV to 100 MeV/nucleon: Fifty Years of Research. *Space Sci. Rev.*, 214:124, 2018. doi: <https://doi.org/10.1007/s11214-018-0560-z>.
- B. Kreisler, G. Anton, J. Durst, and T. Michel. 3D simulation of induced signals in the Medipix detector. In *2007 IEEE Nuclear Science Symposium Conference Record*, volume 4, pages 3166–3169, 2007. doi: <https://doi.org/10.1109/NSSMIC.2007.4436799>.
- A. S. Krieger, A. F. Timothy, and E. C. Roelof. A coronal hole and its identification as the source of a high velocity solar wind stream. *Sol. Phys.*, 29:505–525, 1973. doi: <https://doi.org/10.1007/BF00150828>.
- M. Kroupa, A. Bahadori, T. Campbell-Ricketts, A. Empl, S. M. Hoang, J. Idarraga-Munoz, R. Rios, E. Semones, N. Stoffle, L. Tlustos, D. Tureček, and L. Pinsky. A semiconductor radiation imaging pixel detector for space radiation dosimetry. *Life Sci. Space Res.*, 6:69–78, 2015. ISSN 2214-5524. doi: <https://doi.org/10.1016/j.lssr.2015.06.006>.
- S. Kurita, Y. Miyoshi, S. Kasahara, S. Yokota, Y. Kasahara, S. Matsuda, A. Kumamoto, A. Matsuoka, and I. Shinohara. Deformation of Electron Pitch Angle Distributions Caused by Upper Band Chorus Observed by the Arase Satellite. *Geophys. Res. Lett.*, 45(16):7996–8004, 2018. doi: <https://doi.org/10.1029/2018GL079104>.
- H. Laakso and M. Jarva. Evolution of the plasmopause position. *J. Atmos. Sol.-Terr. Phys.*, 63(11):1171–1178, 2001. ISSN 1364-6826. doi: [https://doi.org/10.1016/S1364-6826\(01\)00008-6](https://doi.org/10.1016/S1364-6826(01)00008-6).
- L. D. Landau and E. M. Lifshitz. *Mechanics: Volume 1*. Course of Theoretical Physics. Elsevier Science, 1976. ISBN 9780750628969.
- L. D. Landau and E. M. Lifshitz. *Electrodynamics of Continuous Media, course of Theoretical Physics*, volume 8. Elsevier, 1982.
- A. Lazarian and E. T. Vishniac. Reconnection in a Weakly Stochastic Field. *Astrophys. J.*, 517(2):700, 1999. doi: <https://dx.doi.org/10.1086/307233>.
- G. Le, C. T. Russell, J. T. Gosling, and M. F. Thomsen. ISEE observations of low-latitude boundary layer for northward interplanetary magnetic field: Implications for cusp reconnection. *J. Geophys. Res.*, 101(A12):27239–27249, 1996. doi: <https://doi.org/10.1029/96JA02528>.
- G. Leand and C. T. Russell. The thickness and structure of high beta magnetopause current layer. *Geophys. Res. Lett.*, 21(23):2451–2454, 1994. doi: <https://doi.org/10.1029/94GL02292>.

- D.-Y. Lee, S. Ohtani, P. C. Brandt, and L. R. Lyons. Energetic neutral atom response to solar wind dynamic pressure enhancements. *J. Geophys. Res.*, 112(A9), 2007. doi: <https://doi.org/10.1029/2007JA012399>.
- S. Lejosne and P. Kollmann. Radiation Belt Radial Diffusion at Earth and Beyond. *Space Sci. Rev.*, 216(1):19, 2020. doi: <https://doi.org/10.1007/s11214-020-0642-6>.
- R. L. Lin, X. X. Zhang, S. Q. Liu, Y. L. Wang, and J. C. Gong. A three-dimensional asymmetric magnetopause model. *J. Geophys. Res.*, 115(A4), 2010. doi: <https://doi.org/10.1029/2009JA014235>.
- Z.-Q. Liu, J. Y. Lu, C. Wang, K. Kabin, J. S. Zhao, M. Wang, J. P. Han, J. Y. Wang, and M. X. Zhao. A three-dimensional high Mach number asymmetric magnetopause model from global MHD simulation. *J. Geophys. Res.*, 120(7):5645–5666, 2015. doi: <https://doi.org/10.1002/2014JA020961>.
- Z. Y. Liu, Q.-G. Zong, Y. X. Hao, X.-Z. Zhou, X. H. Ma, and Y. Liu. Electron dropout echoes induced by interplanetary shock: A statistical study. *J. Geophys. Res.*, 122(8):8037–8050, 2017. doi: <https://doi.org/10.1002/2017JA024045>.
- X. Llopart, M. Campbell, R. Dinapoli, D. San Segundo, and E. Pernigotti. Medipix2: A 64-k pixel readout chip with 55 μm square elements working in single photon counting mode. *IEEE Trans. Nucl. Sci.*, 49(5):2279–2283, 2002. doi: <http://dx.doi.org/10.1109/TNS.2002.803788>.
- X. Llopart, R. Ballabriga, M. Campbell, L. Tlustos, and W. Wong. Timepix, a 65k programmable pixel readout chip for arrival time, energy and/or photon counting measurements. *Nucl. Instrum. Methods Phys. Res.*, 581(1):485–494, 2007. ISSN 0168-9002. doi: <https://doi.org/10.1016/j.nima.2007.08.079>. VCI 2007.
- X. Llopart, J. Alozy, R. Ballabriga, M. Campbell, R. Casanova, V. Gromov, E.H.M. Heijne, T. Poikela, E. Santin, V. Sriskaran, L. Tlustos, and A. Vitkovskiy. Timepix4, a large area pixel detector readout chip which can be tiled on 4 sides providing sub-200 ps timestamp binning. *J. Instrum.*, 17(01):C01044, 2022. doi: <https://dx.doi.org/10.1088/1748-0221/17/01/C01044>.
- L. R. Lyons and R. M. Thorne. Equilibrium structure of radiation belt electrons. *J. Geophys. Res.*, 78(13):2142–2149, 1973. doi: <https://doi.org/10.1029/JA078i013p02142>.
- L. R. Lyons, R. M. Thorne, and C. F. Kennel. Pitch-angle diffusion of radiation belt electrons within the plasmasphere. *J. Geophys. Res.*, 77(19):3455–3474, 1972. doi: <https://doi.org/10.1029/JA077i019p03455>.
- H. Man, M. Zhou and Z. Zhong, X. Deng, and H. Li. Statistics of the Intense Current Structure in the Dayside Magnetopause Boundary Layer. *J. Geophys. Res.*, 126(12):e2021JA029890, 2021. doi: <https://doi.org/10.1029/2021JA029890>.

- R.G. Marsden. The heliosphere after Ulysses. *Astrophys. Space Sci.*, 277:337–347, 2001. doi: <https://doi.org/10.1023/A:1012260014646>.
- D. J. McComas, H. A. Elliott, J. T. Gosling, D. B. Reisenfeld, R. M. Skoug, B. E. Goldstein, M. Neugebauer, and A. Balogh. Ulysses’ second fast-latitude scan: Complexity near solar maximum and the reformation of polar coronal holes. *Geophys. Res. Lett.*, 29(9):4–1–4–4, 2002. doi: <https://doi.org/10.1029/2001GL014164>.
- C. E. McIlwain. Coordinates for mapping the distribution of magnetically trapped particles. *J. Geophys. Res.*, 66(11):3681–3691, 1961. doi: <https://doi.org/10.1029/JZ066i011p03681>.
- C. E. McIlwain. Magnetic coordinates. *Space Sci. Rev.*, 5(5):585–598, 1966. doi: <https://doi.org/10.1007/BF00167327>.
- M. Menvielle, T. Iyemori, A. Marchaudon, M. Nosé, M. Mandea, and M. Korte. *Geomagnetic Indices*, pages 183–228. Springer Netherlands, Dordrecht, 2011. ISBN 978-90-481-9858-0. doi: https://doi.org/10.1007/978-90-481-9858-0_8.
- N. P. Meredith, R. B. Horne, S. A. Glauert, and R. R. Anderson. Slot region electron loss timescales due to plasmaspheric hiss and lightning-generated whistlers. *J. Geophys. Res.*, 112(A8), 2007. doi: <https://doi.org/10.1029/2007JA012413>.
- P. Meyer and J. A. Simpson. Changes in Amplitude of the Cosmic-Ray 27-Day Intensity Variation with Solar Activity. *Phys. Rev.*, 96(4):1085–1088, 1954. doi: <https://doi.org/10.1103/PhysRev.96.1085>.
- P. Meyer, E. N. Parker, and J. A. Simpson. Solar Cosmic Rays of February, 1956 and Their Propagation through Interplanetary Space. *Phys. Rev.*, 104(3):768–783, 1956. doi: <https://doi.org/10.1103/PhysRev.104.768>.
- R.M. Millan and R.M. Thorne. Review of radiation belt relativistic electron losses. *J. Atmos. Sol.-Terr. Phys.*, 69(3):362–377, 2007. ISSN 1364-6826. doi: <https://doi.org/10.1016/j.jastp.2006.06.019>.
- E. V. Mishin and A. V. Streltsov. Chapter 1 - Introduction: near-Earth space environment. In E. V. Mishin and A. V. Streltsov, editors, *Nonlinear Wave and Plasma Structures in the Auroral and Subauroral Geospace*, pages 1–16. Elsevier, 2022. ISBN 978-0-12-820760-4. doi: <https://doi.org/10.1016/B978-0-12-820760-4.00001-6>.
- W. Mishra and L. Teriaca. Propagation of coronal mass ejections from the Sun to the Earth. *J. Astrophys. Astron.*, 44, 2023. doi: <https://doi.org/10.1007/s12036-023-09910-6>.
- Y. Miyoshi, S. Saito, K. Seki, T. Nishiyama, R. Kataoka, K. Asamura, Y. Katoh, Y. Ebihara, T. Sakanoi, M. Hirahara, S. Oyama, S. Kurita, and O. Santolik. Relation between fine structure of energy spectra for pulsating aurora electrons and frequency spectra of whistler mode chorus waves. *J. Geophys. Res.*, 120(9):7728–7736, 2015. doi: <https://doi.org/10.1002/2015JA021562>.

- Y. Miyoshi, S. Saito, S. Kurita, K. Asamura, K. Hosokawa, T. Sakanoi, T. Mitani, Y. Ogawa, S. Oyama, F. Tsuchiya, S. L. Jones, A. N. Jaynes, and J. B. Blake. Relativistic Electron Microbursts as High-Energy Tail of Pulsating Aurora Electrons. *Geophys. Res. Lett.*, 47(21):e2020GL090360, 2020. doi: <https://doi.org/10.1029/2020GL090360>.
- M. B. Moldwin, S. Mayerberger, H. K. Rassoul, T. Barnicki, and R. R. Anderson. Plasmapause response to geomagnetic storms: CRRES results. *J. Geophys. Res.*, 108(A11), 2003. doi: <https://doi.org/10.1029/2003JA010187>.
- K. R. Murphy, C. E. J. Watt, I. R. Mann, I. J. Rae, D. G. Sibeck, A. J. Boyd, C. F. Forsyth, D. L. Turner, S. G. Claudepierre, D. N. Baker, H. E. Spence, G. D. Reeves, J. B. Blake, and J. Fennell. The Global Statistical Response of the Outer Radiation Belt During Geomagnetic Storms. *Geophys. Res. Lett.*, 45(9):3783–3792, 2018. doi: <https://doi.org/10.1002/2017GL076674>.
- P. Mánek, B. Bergmann, P. Burian, L. Meduna, S. Pospíšil, and M. Suk. Randomized Computer Vision Approaches for Pattern Recognition in Timepix and Timepix3 Detectors. Connecting the Dots and Workshop on Intelligent Trackers, 4 2019.
- M. P. Nakada and G. D. Mead. Diffusion of protons in the outer radiation belt. *J. Geophys. Res.*, 70(19):4777–4791, 1965. doi: <https://doi.org/10.1029/JZ070i019p04777>.
- S. Nerney and S. T. Suess. Stagnation Flow in Thin Streamer Boundaries. *Astrophys. J.*, 624(1):378, 2005. doi: <https://dx.doi.org/10.1086/428924>.
- N. F. Ness, C. S. Scearce, and J. B. Seek. Initial results of the imp 1 magnetic field experiment. *J. Geophys. Res.*, 69(17):3531–3569, 1964. doi: <https://doi.org/10.1029/JZ069i017p03531>.
- N. F. Ness, A. J. Hundhausen, and S. J. Bame. Observations of the interplanetary medium: Vela 3 and Imp 3, 1965–1967. *J. Geophys. Res.*, 76(28):6643–6660, 1971. doi: <https://doi.org/10.1029/JA076i028p06643>.
- M. Neugebauer and C. W. Snyder. Mariner 2 observations of the solar wind: 1. Average properties. *J. Geophys. Res.*, 71(19):4469–4484, 1966. doi: <https://doi.org/10.1029/JZ071i019p04469>.
- W. N. Neupert and V. Pizzo. Solar coronal holes as sources of recurrent geomagnetic disturbances. *J. Geophys. Res.*, 79(25):3701–3709, 1974. doi: <https://doi.org/10.1029/JA079i025p03701>.
- L. Nikitina and L. Trichtchenko. Dynamics of Electron Flux in the Slot Region and Geomagnetic Activity. *Space Weather*, 19(4):e2020SW002661, 2021. doi: <https://doi.org/10.1029/2020SW002661>.
- Z. Němeček, J. Šafránková, L. Přech, and J.-A. Sauvaud. *The Structure of Magnetopause Layers at Low Latitudes: INTERBALL Contributions*, pages 71–82. American Geophysical Union (AGU), 2003. ISBN 9781118668566. doi: <https://doi.org/10.1029/133GM07>.

- S. Ohtani and T. Uozumi. Nightside magnetospheric current circuit: Time constants of the solar wind-magnetosphere coupling. *J. Geophys. Res.*, 119(5): 3558–3572, 2014. doi: <https://doi.org/10.1002/2013JA019680>.
- D. M. Oliveira. Magnetohydrodynamic Shocks in the Interplanetary Space: a Theoretical Review. *Braz. J. Phys.*, 47:81–95, 2017. doi: <https://doi.org/10.1007/s13538-016-0472-x>.
- L. G. Ozeke, I. R. Mann, K. R. Murphy, A. W. Degeling, S. G. Claudepierre, and H. E. Spence. Explaining the apparent impenetrable barrier to ultra-relativistic electrons in the outer Van Allen belt. *Nat. Commun.*, 9:1844, 2018. doi: <https://doi.org/10.1038/s41467-018-04162-3>.
- E. N. Parker. Acceleration of Cosmic Rays in Solar Flares. *Phys. Rev.*, 107: 830–836, 1957. doi: <https://doi.org/10.1103/PhysRev.107.830>.
- E. N. Parker. Dynamics of the Interplanetary Gas and Magnetic Fields. *Astrophys. J.*, 128(3):664–676, 1958. ISSN 0004-637X. doi: 10.1086/146579.
- E. N. Parker. *Interplanetary Dynamical Processes*. New York: Interscience Publishers, 1963.
- E. N. Parker. Reflections on Macrophysics and the Sun (Special Historical Review). *Sol. Phys.*, 176:219–247, 1997. doi: <https://doi.org/10.1023/A:1005072231043>.
- G. Paschmann, W. Baumjohann, N. Sckopke, T.-D. Phan, and H. Lühr. Structure of the dayside magnetopause for low magnetic shear. *J. Geophys. Res.*, 98(A8): 13409–13422, 1993. doi: <https://doi.org/10.1029/93JA00646>.
- H. E. Petschek. Magnetic Field Annihilation. In *The Physics of Solar Flares, Proceedings of the AAS-NASA Symposium*, volume 50, page 425. NASA Special Publication, 1964.
- V. Pierrard, J. Goldstein, N. André, V. K. Jordanova, G. A. Kotova, J. F. Lemaire, M. W. Liemohn, and H. Matsui. Recent Progress in Physics-Based Models of the Plasmasphere. *Space Sci. Rev.*, 145(1):193–229, 2009. doi: <https://doi.org/10.1007/s11214-008-9480-7>.
- V. Pierrard, J.-F. Ripoll, G. Cunningham, E. Botek, O. Santolík, S. Thaller, W. S. Kurth, and M. Cosmides. Observations and Simulations of Dropout Events and Flux Decays in October 2013: Comparing MEO Equatorial With LEO Polar Orbit. *J. Geophys. Res.*, 126(6):e2020JA028850, 2021. doi: <https://doi.org/10.1029/2020JA028850>.
- J. Pilchowski, A. Kopp, K. Herbst, and B. Heber. On the definition and calculation of a generalised McIlwain parameter. *Astrophys. Space Sci. Trans.*, 6(1):9–17, 2010. doi: 10.5194/astra-6-9-2010. URL <http://www.astrophys-space-sci-trans.net/6/9/2010/>.
- W. G. Pilipp and G. Morfill. The formation of the plasma sheet resulting from plasma mantle dynamics. *J. Geophys. Res.*, 83(A12):5670–5678, 1978. doi: <https://doi.org/10.1029/JA083iA12p05670>.

- V. J. Pizzo. *Interplanetary Shocks on the Large Scale: A Retrospective on the Last Decade's Theoretical Efforts*, pages 51–68. American Geophysical Union (AGU), 1985. ISBN 9781118664179. doi: <https://doi.org/10.1029/GM035p0051>.
- T. Poikela, J. Plosila, T. Westerlund, M. Campbell, M. De Gaspari, X. Llopart, V. Gromov, R. Kluit, M. van Beuzekom, F. Zappone, V. Zivkovic, C. Brezina, K. Desch, Y. Fu, and A. Kruth. Timepix3: a 65K channel hybrid pixel readout chip with simultaneous ToA/ToT and sparse readout. *J. Instrum.*, 9(05): C05013, May 2014. doi: <https://dx.doi.org/10.1088/1748-0221/9/05/C05013>.
- S. Procz, C. Avila, J. Fey, G. Roque, M. Schuetz, and E. Hamann. X-ray and gamma imaging with Medipix and Timepix detectors in medical research. *Radiat. Meas.*, 127:106104, 2019. ISSN 1350-4487. doi: <https://doi.org/10.1016/j.radmeas.2019.04.007>.
- L. Rakhmanova, M. Riazantseva, and G. Zastenker. Plasma and Magnetic Field Turbulence in the Earth's Magnetosheath at Ion Scales. *Front. Astron. Space Sci.*, 7, 2021. doi: <https://doi.org/10.3389/fspas.2020.616635>.
- G. D. Reeves, K. L. McAdams, R. H. W. Friedel, and T. P. O'Brien. Acceleration and loss of relativistic electrons during geomagnetic storms. *Geophys. Res. Lett.*, 30(10), 2003. doi: <https://doi.org/10.1029/2002GL016513>.
- J.-F. Ripoll, S. G. Claudepierre, A. Y. Ukhorskiy, C. Colpitts, X. Li, J. F. Fennell, and C. Crabtree. Particle Dynamics in the Earth's Radiation Belts: Review of Current Research and Open Questions. *J. Geophys. Res.*, 125(5): e2019JA026735, 2020. doi: <https://doi.org/10.1029/2019JA026735>.
- J. G. Roederer. On the adiabatic motion of energetic particles in a model magnetosphere. *J. Geophys. Res.*, 72(3):981–992, 1967. doi: <https://doi.org/10.1029/JZ072i003p00981>.
- J. G. Roederer and S. Lejosne. Coordinates for Representing Radiation Belt Particle Flux. *J. Geophys. Res.*, 123(2):1381–1387, 2018. doi: <https://doi.org/10.1002/2017JA025053>.
- A. Rosenfeld, S. Alnaghy, M. Petasecca, D. Cutajar, M. Lerch, S. Pospíšil, V. Giacometti, R. Schulte, V. Rosso, M. Würll, C. Granja, M. Martišíková, and K. Parodi. Medipix detectors in radiation therapy for advanced quality-assurance. *Radiat. Meas.*, 130:106211, 2020. ISSN 1350-4487. doi: <https://doi.org/10.1016/j.radmeas.2019.106211>.
- S. S. Rossolenko, E. E. Antonova, Yu. I. Yermolaev, I. P. Kirpichev, N. L. Borodkova, and E. Yu. Budnik. Formation and characteristics of low latitude boundary layer. *Adv. Space Res.*, 41(10):1545–1550, 2008. ISSN 0273-1177. doi: <https://doi.org/10.1016/j.asr.2007.06.069>.
- M. Ruffenach, S. Bourdarie, J. Mekki, D. Falguère, J.-R. Vaillé, and J. Carrone. A proton detector for energies from 2 MeV to 20 MeV. In *European Conference on Radiation and its Effects on Components and Systems (RADECS) 2019*, Montpellier, France, 2019. URL <https://hal.science/hal-02797282>.

- M. Ruffenach, S. Bourdarie, B. Bergmann, S. Gohl, J. Mekki, and J. Vaillé. A New Technique Based on Convolutional Neural Networks to Measure the Energy of Protons and Electrons With a Single Timepix Detector. *IEEE Trans. Nucl. Sci.*, 68(8):1746–1753, 2021. doi: <https://doi.org/10.1109/TNS.2021.3071583>.
- C. T. Russell, J. G. Luhmann, and R. J. Strangeway. *Space Physics: An Introduction*. Cambridge University Press, 2016. ISBN 9781107098824.
- R. Z. Sagdeev and C. F. Kennel. Collisionless shock waves. *Sci. Am.*, 264:106–113, 1991. doi: [10.1038/scientificamerican0491-106](https://doi.org/10.1038/scientificamerican0491-106).
- J. A. Sauvaud, T. Moreau, R. Maggiolo, J.-P. Treilhou, C. Jacquy, A. Cros, J. Coutelier, J. Rouzaud, E. Penou, and M. Gangloff. High-energy electron detection onboard DEMETER: The IDP spectrometer, description and first results on the inner belt. *Planet. Space Sci.*, 54(5):502–511, 2006. ISSN 0032-0633. doi: <https://doi.org/10.1016/j.pss.2005.10.019>.
- J.-A. Sauvaud, R. Maggiolo, C. Jacquy, M. Parrot, J.-J. Berthelier, R. J. Gamble, and C. J. Rodger. Radiation belt electron precipitation due to VLF transmitters: Satellite observations. *Geophys. Res. Lett.*, 35(9), 2008. doi: <https://doi.org/10.1029/2008GL033194>.
- D. M. Sawyer and J. I. Vette. Trapped Particle Environment for Solar Maximum and Solar Minimum (AP8). Technical report, NSSDC Report 76-06, 1976.
- Q. Schiller, D. Gerhardt, L. Blum, X. Li, and S. Palo. Design and Scientific Return of a Miniaturized Particle Telescope Onboard the Colorado Student Space Weather Experiment (CSSWE) CubeSat. In *2014 IEEE Aerospace Conference*, pages 1–14, 2014. doi: <http://dx.doi.org/10.1109/AERO.2014.6836372>.
- Q. Schiller, S. G. Kanekal, L. K. Jian, X. Li, A. Jones, D. N. Baker, A. Jaynes, and H. E. Spence. Prompt injections of highly relativistic electrons induced by interplanetary shocks: A statistical study of Van Allen Probes observations. *Geophys. Res. Lett.*, 43(24):12,317–12,324, 2016. doi: <https://doi.org/10.1002/2016GL071628>.
- A. F. K. Schmidt. *Erdmagnetismus*. [s.n.], 1917.
- R. S. Selesnick, M. K. Hudson, and B. T. Kress. Direct observation of the CRAND proton radiation belt source. *J. Geophys. Res.*, 118(12):7532–7537, 2013. doi: <https://doi.org/10.1002/2013JA019338>.
- R. S. Selesnick, D. N. Baker, A. N. Jaynes, X. Li, S. G. Kanekal, M. K. Hudson, and B. T. Kress. Observations of the inner radiation belt: CRAND and trapped solar protons. *J. Geophys. Res.*, 119(8):6541–6552, 2014. doi: <https://doi.org/10.1002/2014JA020188>.
- R. S. Selesnick, D. N. Baker, A. N. Jaynes, X. Li, S. G. Kanekal, M. K. Hudson, and B. T. Kress. Inward diffusion and loss of radiation belt protons. *J. Geophys. Res.*, 121(3):1969–1978, 2016. doi: <https://doi.org/10.1002/2015JA022154>.

- M. Shoji and Y. Omura. Simulation of electromagnetic ion cyclotron triggered emissions in the Earth's inner magnetosphere. *J. Geophys. Res.*, 116(A5), 2011. doi: <https://doi.org/10.1029/2010JA016351>.
- Y. Y. Shprits, R. M. Thorne, R. Friedel, G. D. Reeves, J. Fennell, D. N. Baker, and S. G. Kanekal. Outward radial diffusion driven by losses at magnetopause. *J. Geophys. Res.*, 111(A11), 2006. doi: <https://doi.org/10.1029/2006JA011657>.
- Y. Y. Shprits, V. Angelopoulos, C. T. Russell, R. J. Strangeway, A. Runov, D. Turner, R. Caron, P. Cruce, D. Leneman, I. Michaelis, V. Petrov, M. Panasyuk, I. Yashin, A. Drozdov, C. L. Russell, V. Kalegaev, I. Nazarkov, and J. H. Clemmons. Scientific Objectives of Electron Losses and Fields Investigation Onboard Lomonosov Satellite. *Space Sci. Rev.*, 214:25, 2017. doi: <https://doi.org/10.1007/s11214-017-0455-4>.
- J.-H. Shue, P. Song, C. T. Russell, J. T. Steinberg, J. K. Chao, G. Zastenker, O. L. Vaisberg, S. Kokubun, H. J. Singer, T. R. Detman, and H. Kawano. Magnetopause location under extreme solar wind conditions. *J. Geophys. Res.*, 103(A8):17691–17700, 1998. doi: <https://doi.org/10.1029/98JA01103>.
- P. Sievers, T. Schneider, T. Michel, and G. Anton. X-ray spectroscopy with photon counting imaging detectors such as Timepix. In *2011 IEEE Nuclear Science Symposium Conference Record*, pages 1826–1828, 2011. doi: <https://doi.org/10.1109/NSSMIC.2011.6154692>.
- J. A. Simpson. Cosmic-Radiation Intensity-Time Variations and Their Origin. III. The Origin of 27-Day Variations. *Phys. Rev.*, 94(2):426–440, 1954. ISSN 0031-899X. doi: <https://doi.org/10.1103/PhysRev.94.426>.
- A. K. Singh, R. P. Singh, and D. Siingh. State studies of Earth's plasmasphere: A review. *Planet. Space Sci.*, 59(9):810–834, 2011. ISSN 0032-0633. doi: <https://doi.org/10.1016/j.pss.2011.03.013>.
- G. L. Siscoe, W. Lotko, and B. U. Ö. Sonnerup. A high-latitude, low-latitude boundary layer model of the convection current system. *J. Geophys. Res.*, 96(A3):3487–3495, 1991. doi: <https://doi.org/10.1029/90JA02362>.
- E. J. Smith and J. H. Wolfe. Observations of interaction regions and corotating shocks between one and five AU: Pioneers 10 and 11. *Geophys. Res. Lett.*, 3(3):137–140, 1976. doi: <https://doi.org/10.1029/GL003i003p00137>.
- P. Song and C. T. Russell. Model of the formation of the low-latitude boundary layer for strongly northward interplanetary magnetic field. *J. Geophys. Res.*, 97(A2):1411–1420, 1992. doi: <https://doi.org/10.1029/91JA02377>.
- C. Spearman. The Proof and Measurement of Association between Two Things. *Am. J. Psychol.*, 15(1):72–101, 1904. ISSN 00029556. doi: <https://doi.org/10.2307/1412159>.
- N. Stoffle, L. Pinsky, M. Kroupa, S. Hoang, J. Idarraga, C. Amberboy, R. Rios, J. Hauss, J. Keller, A. Bahadori, E. Semones, D. Tureček, J. Jakůbek, Z. Vykydal, and S. Pospíšil. Timepix-based radiation environment monitor measurements aboard the International Space Station. *Nucl. Instr. Methods Phys. Res.*,

- 782:143–148, 2015. ISSN 0168-9002. doi: <https://doi.org/10.1016/j.nima.2015.02.016>.
- C. Störmer. Sur les trajectoires des corpuscules électrisés dans l'espace sous l'action du magnétisme terrestre, avec application aux aurores boréales. *Le Radium*, 9:395–399, 1912. doi: [10.1051/radium:01912009011039501](https://doi.org/10.1051/radium:01912009011039501). URL <https://hal.science/jpa-00242574>.
- Z. Su, H. Zhu, F. Xiao, Q.-G. Zong, X.-Z. Zhou, H. Zheng, Y. Wang, S. Wang, Y.-X. Hao, Z. Gao, Z. He, D. N. Baker, H. E. Spence, G. D. Reeves, J. B. Blake, and J. R. Wygant. Ultra-low-frequency wave-driven diffusion of radiation belt relativistic electrons. *Nat. Commun.*, 6:10096, 2015. doi: <https://doi.org/10.1038/ncomms10096>.
- S. T. Suess and S. F. Nerney. Stagnation Flow in Streamer Boundaries. *Astrophys. J.*, 565(2):1275, 2002. doi: <https://dx.doi.org/10.1086/324697>.
- M. Sugiura, T. Kamei, A. Berthelier, and M. Menvielle. *Equatorial Dst index, 1957-1986*. ISGI Publications Office Saint-Maur-Des-Fosses, 1991. URL <https://worldcat.org/title/25515435>.
- P. A. Sweet. 14. The neutral point theory of solar flares. *Symposium - International Astronomical Union*, 6:123–134, 1958. doi: <https://doi.org/10.1017/S0074180900237704>.
- W.-L. Teh, M. Abdullah, and A. M. Hasbi. Lack of relationship between geoeffectiveness and orientations of magnetic clouds with bipolar Bz and unipolar southward Bz. *Planet. Space Sci.*, 115:27–34, 2015. ISSN 0032-0633. doi: <https://doi.org/10.1016/j.pss.2014.11.021>.
- R. M. Thorne, W. Li, B. Ni, Q. Ma, J. Bortnik, D. N. Baker, H. E. Spence, G. D. Reeves, M. G. Henderson, C. A. Kletzing, W. S. Kurth, G. B. Hospodarsky, D. Turner, and V. Angelopoulos. Evolution and slow decay of an unusual narrow ring of relativistic electrons near $L \sim 3.2$ following the September 2012 magnetic storm. *Geophys. Res. Lett.*, 40(14):3507–3511, 2013. doi: <https://doi.org/10.1002/grl.50627>.
- R. M. Thorne, J. Bortnik, W. Li, L. Chen, B. Ni, and Q. Ma. *How Whistler-Mode Waves and Thermal Plasma Density Control the Global Distribution of the Diffuse Aurora and the Dynamical Evolution of Radiation Belt Electrons*, chapter 9, pages 115–125. American Geophysical Union (AGU), 2016. ISBN 9781119066880. doi: <https://doi.org/10.1002/9781119066880.ch9>.
- V. Tichý, T. Holý, J. Jakubek, V. Linhart, S. Pospíšil, and Z. Vykydal. X-ray fluorescence imaging with pixel detectors. *Nucl. Instr. Methods Phys. Res.*, 591(1):67–70, 2008. ISSN 0168-9002. doi: <https://doi.org/10.1016/j.nima.2008.03.122>.
- K. J. Trattner, J. S. Mulcock, S. M. Petriner, and S. A. Fuselier. Probing the boundary between antiparallel and component reconnection during southward interplanetary magnetic field conditions. *J. Geophys. Res.*, 112(A8), 2007. doi: <https://doi.org/10.1029/2007JA012270>.

- K. J. Trattner, S. M. Petrinec, and S. A. Fuselier. The Location of Magnetic Reconnection at Earth's Magnetopause. *Space Sci. Rev.*, 217, 2021. doi: <https://doi.org/10.1007/s11214-021-00817-8>.
- A. S. Tremsin, J. V. Vallerga, O. H. W. Siegmund, J. Woods, L. E. De Long, J. T. Hastings, R. J. Koch, S. A. Morley, Y.-D. Chuang, and S. Roy. Photon-counting MCP/Timepix detectors for soft X-ray imaging and spectroscopic applications. *J. Synchrotron Radiat.*, 28(4):1069–1080, 2021. doi: <https://doi.org/10.1107/S1600577521003908>.
- R. Treumann and W. Baumjohann. Collisionless magnetic reconnection in space plasmas. *Front. Phys.*, 1, 2013. ISSN 2296-424X. doi: <https://doi.org/10.3389/fphy.2013.00031>.
- H. Tsuji, Y. Ebihara, and T. Tanaka. Formation of multiple energy dispersion of H⁺, He⁺, and O⁺ ions in the inner magnetosphere in response to interplanetary shock. *J. Geophys. Res.*, 122(4):4387–4397, 2017. doi: <https://doi.org/10.1002/2016JA023704>.
- B. T. Tsurutani, W. D. Gonzalez, A. L. C. Gonzalez, F. L. Guarnieri, N. Gopalswamy, M. Grande, Y. Kamide, Y. Kasahara, G. Lu, I. Mann, R. McPheron, F. Soraas, and V. Vasyliunas. Corotating solar wind streams and recurrent geomagnetic activity: A review. *J. Geophys. Res.*, 111(A7), 2006. doi: <https://doi.org/10.1029/2005JA011273>.
- B. T. Tsurutani, G. S. Lakhina, O. P. Verkhoglyadova, W. D. Gonzalez, E. Echer, and F. L. Guarnieri. A review of interplanetary discontinuities and their geomagnetic effects. *J. Atmos. Sol.-Terre.Phys.*, 73(1):5–19, 2011. ISSN 1364-6826. doi: <https://doi.org/10.1016/j.jastp.2010.04.001>.
- W. Tu, M. M. Cowee, and K. Liu. Modeling the loss of inner belt protons by magnetic field line curvature scattering. *J. Geophys. Res.*, 119(7):5638–5650, 2014. doi: <https://doi.org/10.1002/2014JA019864>.
- D. L. Turner, S. K. Morley, Y. Miyoshi, B. Ni, and C.-L. Huang. *Outer Radiation Belt Flux Dropouts: Current Understanding and Unresolved Questions*, pages 195–212. American Geophysical Union (AGU), 2012. ISBN 9781118704752. doi: <https://doi.org/10.1029/2012GM001310>.
- D. L. Turner, V. Angelopoulos, W. Li, J. Bortnik, B. Ni, Q. Ma, R. M. Thorne, S. K. Morley, M. G. Henderson, G. D. Reeves, M. Usanova, I. R. Mann, S. G. Claudepierre, J. B. Blake, D. N. Baker, C.-L. Huang, H. Spence, W. Kurth, C. Kletzing, and J. V. Rodriguez. Competing source and loss mechanisms due to wave-particle interactions in Earth's outer radiation belt during the 30 September to 3 October 2012 geomagnetic storm. *J. Geophys. Res.*, 119(3):1960–1979, 2014. doi: <https://doi.org/10.1002/2014JA019770>.
- D. L. Turner, E. K. J. Kilpua, H. Hietala, S. G. Claudepierre, T. P. O'Brien, J. F. Fennell, J. B. Blake, A. N. Jaynes, S. Kanekal, D. N. Baker, H. E. Spence, J.-F. Ripoll, and G. D. Reeves. The Response of Earth's Electron Radiation Belts to Geomagnetic Storms: Statistics From the Van Allen Probes Era Including

- Effects From Different Storm Drivers. *J. Geophys. Res.*, 124(2):1013–1034, 2019. doi: <https://doi.org/10.1029/2018JA026066>.
- M. E. Usanova, A. Drozdov, K. Orlova, I. R. Mann, Y. Shprits, M. T. Robertson, D. L. Turner, D. K. Milling, A. Kale, D. N. Baker, S. A. Thaller, G. D. Reeves, H. E. Spence, C. Kletzing, and J. Wygant. Effect of EMIC waves on relativistic and ultrarelativistic electron populations: Ground-based and Van Allen Probes observations. *Geophys. Res. Lett.*, 41(5):1375–1381, 2014. doi: <https://doi.org/10.1002/2013GL059024>.
- J. A. Van Allen, C. E. McIlwain, and G. H. Ludwig. Radiation observations with satellite 1958 ϵ . *J. Geophys. Res.*, 64(3):271–286, 1959. doi: <https://doi.org/10.1029/JZ064i003p00271>.
- V. M. Vasyliunas. Low-Energy Electrons in the Magnetosphere as Observed by OGO-1 and OGO-3. In R. L. Carovillano, J. F. McClay, and H. R. Radoski, editors, *Physics of the Magnetosphere*, pages 622–640, Dordrecht, 1968. Springer Netherlands. ISBN 978-94-010-3467-8.
- S. N. Vernov, E. V. Gorchakov, P. I. Shavrin, and K. N. Sharvina. Radiation belts in the region of the South-Atlantic magnetic anomaly. *Space Sci. Rev.*, 7(4):490–533, 1967. doi: <https://doi.org/10.1007/BF00182684>.
- J. I. Vette. The AE-8 trapped electron model environment. Technical report, NSSDC/WDC-A-RS-91-24, 1991.
- J. Žemlička, J. Jakůbek, M. Kroupa, and V. Tichý. Energy- and position-sensitive pixel detector Timepix for X-ray fluorescence imaging. *Nucl. Instr. Methods Phys. Res.*, 607(1):202–204, 2009. ISSN 0168-9002. doi: <https://doi.org/10.1016/j.nima.2009.03.140>.
- C. Wang, J. P. Han, H. Li, Z. Peng, and J. D. Richardson. Solar wind-magnetosphere energy coupling function fitting: Results from a global MHD simulation. *J. Geophys. Res.*, 119(8):6199–6212, 2014. doi: <https://doi.org/10.1002/2014JA019834>.
- J. Y. Wang, Z.-H. Huang, C. Wang, and Z.-Q. Liu. Effects of the interplanetary magnetic field clock angle on the shape of bow shock. *Sci. China Earth Sci.*, 58(7):1228–1234, 2015. doi: <https://doi.org/10.1007/s11430-015-5052-3>.
- M. Wang, J. Y. Lu, K. Kabin, H. Z. Yuan, X. Ma, Z.-Q. Liu, Y. F. Yang, J. S. Zhao, and G. Li. The influence of IMF clock angle on the cross section of the tail bow shock. *J. Geophys. Res.*, 121(11):11,077–11,085, 2016. doi: <https://doi.org/10.1002/2016JA022830>.
- R. C. Wentworth, W. M. MacDonald, and S. F. Singer. Lifetimes of Trapped Radiation Belt Particles Determined by Coulomb Scattering. *Phys. Fluids*, 2(5):499–509, 1959. ISSN 0031-9171. doi: <https://doi.org/10.1063/1.1705940>.
- W.S. Wong, J. Alozy, R. Ballabriga, M. Campbell, I. Kremastiotis, X. Llopart, T. Poikela, V. Sriskaran, L. Tlustos, and D. Tureček. Introducing Timepix2, a frame-based pixel detector readout ASIC measuring energy deposition and

- arrival time. *Radiat. Meas.*, 131:106230, 2020. ISSN 1350-4487. doi: <https://doi.org/10.1016/j.radmeas.2019.106230>.
- X. Xing, L. R. Lyons, V. Angelopoulos, D. Larson, J. McFadden, C. Carlson, A. Runov, and U. Auster. Azimuthal plasma pressure gradient in quiet time plasma sheet. *Geophys. Res. Lett.*, 36(14), 2009. doi: <https://doi.org/10.1029/2009GL038881>.
- S. Yashiro, N. Gopalswamy, G. Michalek, O. C. St. Cyr, S. P. Plunkett, N. B. Rich, and R. A. Howard. A catalog of white light coronal mass ejections observed by the SOHO spacecraft. *J. Geophys. Res.*, 109(A7), 2004. doi: <https://doi.org/10.1029/2003JA010282>.
- V. Yurchyshyn, H. Wang, and V. Abramenko. How directions and helicity of erupted solar magnetic fields define geoeffectiveness of coronal mass ejections. *Adv. Space Res.*, 32(10):1965–1970, 2003. ISSN 0273-1177. doi: [https://doi.org/10.1016/S0273-1177\(03\)90634-X](https://doi.org/10.1016/S0273-1177(03)90634-X).
- J. Zhang, I. G. Richardson, D. F. Webb, N. Gopalswamy, E. Huttunen, J. C. Kasper, N. V. Nitta, W. Poomvises, B. J. Thompson, C.-C. Wu, S. Yashiro, and A. N. Zhukov. Solar and interplanetary sources of major geomagnetic storms ($Dst \leq -100$ nT) during 1996–2005. *J. Geophys. Res.*, 112(A10), 2007. doi: <https://doi.org/10.1029/2007JA012321>.
- X.-Y. Zhang and M. B. Moldwin. The source, statistical properties, and geoeffectiveness of long-duration southward interplanetary magnetic field intervals. *J. Geophys. Res.*, 119(2):658–669, 2014. doi: <https://doi.org/10.1002/2013JA018937>.
- H. Zhao, D. N. Baker, X. Li, A. N. Jaynes, and S. G. Kanekal. The Effects of Geomagnetic Storms and Solar Wind Conditions on the Ultrarelativistic Electron Flux Enhancements. *J. Geophys. Res.*, 124(3):1948–1965, 2019. doi: <https://doi.org/10.1029/2018JA026257>.
- X. Zhou, M. Gedalin, C. T. Russell, V. Angelopoulos, and A. Y. Drozdov. Energetic Ion Reflections at Interplanetary Shocks: First Observations From ARTEMIS. *J. Geophys. Res.*, 125(11), 2020. ISSN 2169-9380. doi: <https://doi.org/10.1029/2020JA028174>.
- A. J. Zmuda, J. H. Martin, and F. T. Heuring. Transverse magnetic disturbances at 1100 kilometers in the auroral region. *J. Geophys. Res.*, 71(21):5033–5045, 1966. doi: <https://doi.org/10.1029/JZ071i021p05033>.
- Q.-G. Zong, X.-Z. Zhou, Y. F. Wang, X. Li, P. Song, D. N. Baker, T. A. Fritz, P. W. Daly, M. Dunlop, and A. Pedersen. Energetic electron response to ULF waves induced by interplanetary shocks in the outer radiation belt. *J. Geophys. Res.*, 114(A10), 2009. doi: <https://doi.org/10.1029/2009JA014393>.
- Q.-G. Zong, Y. F. Wang, H. Zhang, S. Y. Fu, H. Zhang, C. R. Wang, C. J. Yuan, and I. Vogiatzis. Fast acceleration of inner magnetospheric hydrogen and oxygen ions by shock induced ULF waves. *J. Geophys. Res.*, 117(A11), 2012. doi: <https://doi.org/10.1029/2012JA018024>.

List of Figures

1.1	Spiral configuration of interplanetary magnetic field lines frozen into a radially expanding solar wind. The orbit of Earth is shown by a dashed curve. Taken from Parker [1963].	6
1.2	An illustration of fast solar wind catching up with slow solar wind causing compression at the front and rarefaction after. The solid arrows show the relative radial component of the wind at each position. The larger hollow arrows show the pressure gradient resulting from the compression of the plasma. Taken from Pizzo [1985]. . .	8
1.3	Schematic variations of the plasma number density (N), pressure (P), magnetic field magnitude (B), and flow speed (V) for all four types of interplanetary shocks. Taken from Oliveira [2017].	9
1.4	Representation of an ICME and the shock formation. Taken from Oliveira [2017].	10
1.5	A simplified model of the magnetopause current sheet with an unmagnetised solar wind on the left and a plasma free magnetosphere on the right. The current flows downwards in the y-direction. It is carried by the collective action of solar wind particles. Each particle completes half a gyration in the magnetospheric magnetic field before returning to the magnetosheath. Taken from Kivelson and Russell [1995].	12
1.6	Noon–midnight cross section of Earth’s magnetosphere drawn to scale. The positive x-axis points towards the Sun, while the night-side is drawn on the negative side of the x-axis. Compressed day-side magnetic field and the cusps above the magnetic poles on the positive side of the x-axis can be seen. The dashed lines show trajectories followed by particles in the plasma mantle. For more information, see text. Taken from Pilipp and Morfill [1978].	14
1.7	A very basic illustration of magnetic reconnection at an x-type magnetic line. The magnetic field and plasma flow inwards from the top and bottom and flow outwards to the left and right. The central shaded area corresponds to the diffusion region, where $R_m < 1$ and the ideal MHD breaks down. Taken from Kivelson and Russell [1995].	15
1.8	The Dungey cycle, describing the flow of plasma and magnetic field line convection within the magnetosphere driven by magnetic reconnection. The evolution of a given magnetic field line from Earth starts on the dayside (marked as 1 and 1’). Then, following the numbering, the newly reconnected field lines move to the night-side to eventually reconnect, in the far tail (6 and 6’). Taken from Kivelson and Russell [1995].	17

1.9	Noon-midnight view of the plasma regions in the inner magnetosphere. The plasmasphere and the radiation belts occupy more or less the same region. Taken from Kivelson and Russell [1995]. . .	18
1.10	Rough schematic representation of the currents in the magnetosphere. See text for explanation. Taken from Kivelson and Russell [1995].	19
1.11	Exemplary presentation of the three basic particle motions executed by particles trapped in the radiation belts: Gyration, bounce motion in between mirror points, and drift motion around the Earth. Taken from [Gruntman, 1997].	23
1.12	A typical geomagnetic storm as seen by the Dst index. Taken from Burton et al. [1975]. The red vertical lines and text were added to show the three phases of the storm.	29
2.1	An example of a Timepix detector [ESA, 2019].	31
2.2	Schematic of the Timepix detector. An ionising particle strikes the sensor and creates electron-hole pairs. When the charges approach the bottom, a signal is created. Adapted from [Mánek et al., 2019]	32
3.1	The SATRAM module (red circle) attached to the Proba-V satellite prior to launch. Adapted from Granja et al. [2016].	36
3.2	Inside view and scale of the SATRAM module with the Timepix sensor marked with the red circle. Photograph by Carlos Granja.	36
3.3	Relative number of noisy pixels on a weekly basis from August 2014 until June 2023. Until the end of 2021, the number of noisy pixels stays below 0.6%. In 2022, the number of noisy pixels rose quite significantly, up to a maximum of about 22%. The detector recovered in 2023.	38
3.4	Noisy pixel distribution over the Timepix sensor for the years (a) 2015, (b) 2019, (c) 2022, and (d) 2023. The pixels in the lower left corner suffered damage during the launch of the Proba-V satellite. The colour scale represents the number of times a pixel is considered noisy. Note that for 2023, only six month are considered and, therefore, the counts are reduced.	39
3.5	Same as Figure 3.4, but excluding noisy pixels from the edges and the lower left corner of the sensor as seen in Figure 3.4c. The relative number of noisy pixels is greatly reduced.	40
3.6	Photograph of the EPT instrument with cover removed. Taken from [Cyamukungu et al., 2014].	40
3.7	Cross section view of EPT with its twelve sensor modules: S1/S3, S2 and D1 to D10. S1/S3 and S2 define the Low Energy Section (LES) and D1 to D10 define the High Energy Section (HES). The LES defines the FoV of 52°. Taken from [Cyamukungu et al., 2014].	41
3.8	Photograph of the IDP instrument. Shown is the sensor head and the electronic box below. Taken from [Sauvaud et al., 2006]. . . .	43
3.9	Cross-section view of IDP: the collimator made of aluminium is shown in green, the thin aluminium foil for stopping photons and protons below 500 keV is presented in yellow, and the silicon sensor is in red. Taken from [Sauvaud et al., 2006].	43

4.1	Model integrated energy spectrum averaged over the SATRAM orbit for (a) electrons and (b) protons obtained using the AE-8-min and AP-8-min models, respectively. The threshold energies of 500 keV for electrons and 8.8 MeV for protons are marked with red vertical lines.	46
4.2	Stopping power calculated from simulated data. Electrons are presented in red and protons in blue.	49
4.3	Stopping power calculated from SATRAM data. Three stopping power intervals are marked (from left to right): Electrons, protons, and heavier ions.	49
4.4	Particles sorted according to their stopping power into three channels: (a) low stopping power ($\leq 10 \text{ MeV cm}^2 \text{ g}^{-1}$), (b) intermediate stopping power ($10 \text{ MeV cm}^2 \text{ g}^{-1} < \leq 100 \text{ MeV cm}^2 \text{ g}^{-1}$), and (c) high stopping power ($> 100 \text{ MeV cm}^2 \text{ g}^{-1}$).	50
4.5	Particle identification via decision tree using the shape, cluster height, and stopping power. It is denoted whether the stopping power and the angles relative to the sensor can be calculated. CM stands for the centre of mass related to the energy deposition and GC means geometrical centre. See text for details.	51
4.6	Simulation of energy per pixel compared to the number of hit pixels for SATRAM. The bottom edge of the distribution corresponds to 100% electrons, while the top edge resembles 100% protons. The visible lines between $\approx 40\text{k}$ and 60k are unique to a specific particle composition of electrons and protons.	53
4.7	Energy per pixel as a function of the number of pixel hits for SATRAM matching measurement (blue) and simulation (red). The best match for higher number of pixel hits ($> 40\text{k}$) is found for 100% electrons for the lower branch and a 85/15% electron/proton composition for the upper branch.	54
4.8	Scheme of the NN with one input layer with seven features from Table 4.2, two hidden layers with seven neurons each, and one output layer.	56
4.9	Confusion matrix for the NN between truly and falsely identified protons and electrons.	56
5.1	Geographical map of the local mean energy of particles identified in low occupancy frames measured in 2015.	61
5.2	An example of a simulated electron event showcasing track interruption, backscattering, and production of secondary particles. (a) The complete event. (b) Only primary tracks. (c) Only tracks corresponding to secondary particles. See text for explanation. . .	63
5.3	Electron fluxes as a function of time (60s bins) and L-shell (0.5 bins) for EPT (top) and SATRAM (bottom) for the year 2015. The fluxes generally agree, with the EPT results being smoother than the SATRAM results.	64
5.4	Same as Figure 5.3, but for the year 2020. From around July, SATRAM data starts to thin out, potentially due to the increased number of noisy pixels.	65

5.5	The SATRAM fluxes directly compared with the EPT fluxes for the years (a) 2015 and (b) 2020. The corresponding correlation coefficients are 0.83 and 0.85, respectively. The majority of the data points are concentrated close to the unity line (black) and lie within a deviation of one order of magnitude, marked by the magenta lines.	66
5.6	Flux distribution over the world measured by (a) SATRAM and (b) EPT during the year 2015.	67
6.1	Average energetic particle fluxes are colour-coded as a function of energy (ordinate) and L-shell (abscissa) separately for the (a) daytime and (b) nighttime. Adapted from Gohl et al. [2021].	71
6.2	Superposed epoch analysis of all five geomagnetic storms in a seven-day window starting one day before the Dst minimum. The average energetic particle flux in the energy range between 70 keV and 2.34 MeV is colour-coded as a function of the L-shell (ordinate) and time relative to the Dst minimum (abscissa). The average Dst index time dependence is overplotted by the thick black curve. There are four time intervals marked by vertical blue lines: one day “Before” the Dst minimum, at the Dst maximum preceding the storm onset (“Pre”), at the Dst minimum (“Max”), and one day after the Dst minimum (“Post”). Adapted from Gohl et al. [2021].	72
6.3	The same as Figure 6.2 but separated according to (a) Type 1 storms and (b) Type 2 storms. Adapted from Gohl et al. [2021].	72
6.4	Average energetic particle fluxes in L-shell range between 1 and 6 as a function of energy (ordinate) and time relative to the Dst minimum (abscissa) for (a) Type 1 storms and (b) Type 2 storms. Adapted from Gohl et al. [2021].	73
6.5	Average energetic particle fluxes during Type 1 storms are colour-coded as a function of energy (ordinate) and L-shell (abscissa) during four selected two-hour-long time subintervals. (a) One day before the Dst minimum. (b) Around the Dst maximum just before the storm onset. (c) Around the Dst minimum. (d) One day after the Dst minimum. Adapted from Gohl et al. [2021].	74
6.6	The same as Figure 6.5, but for Type 2 storms. Adapted from Gohl et al. [2021].	75
6.7	Dependences obtained for the fifth storm that fits neither Type 1 nor Type 2 classification. (a) Energetic particle fluxes colour-coded as a function of L-shell (ordinate) and time from the Dst minimum (abscissa). The Dst index is overplotted by the thick black curve. (b) Average energetic particle fluxes at L-shells between 1 and 6 colour-coded as a function of energy (ordinate) and time relative to the Dst minimum (abscissa). Adapted from Gohl et al. [2021].	76
6.8	Time dependences of the AE and Dst indices, solar wind flow speed v , solar wind plasma number density n , IMF magnitude B , IMF B_z component, and the plasma beta β for (a) Type 1 storms, (b) Type 2 storms, and (c) the special case. Adapted from Gohl et al. [2021].	77

6.9	The particle flux measured during the storm on 15 December 2006 in the energy range 2057.6–2342.4 keV (blue). The leftmost flank is fitted with a hyperbolic tangent (red). The position of the L barrier is defined as the point, where the flank reaches half of its height. This position is marked by the vertical black line. Adapted from Gohl et al. [2021].	77
6.10	The impenetrable barrier L-shells as a function of energy for all five storms. The colours represent the different storm types, blue being Type 1 storms, green Type 2 storms, and red corresponds to the special case. Adapted from Gohl et al. [2021].	78
6.11	Examples of IP shock arrival events showing the solar wind dynamic pressure (top), subsolar magnetopause distance (middle), and IMF B_z (bottom), as well as electron fluxes (colour-coded) as a function of L-shell (middle ordinate) and time relative to the shock arrival in a seven day window starting one day before the shock arrival. The grey boxes mark the time periods used for the subsequent analysis.	80
6.12	An example of the dependences of the electron flux ratio Φ_a/Φ_b on (from left to right) the subsolar magnetopause distance r_0 , IMF B_z , the solar wind dynamic pressure ratio p_a/p_b , and the energy input E_{in} for L-shells between 1.5 and 2.0, and the energy between 0.6 and 0.7 MeV.	81
6.13	Ratio of electron fluxes Φ_a/Φ_b as a function of the distance between the subsolar magnetopause position and the L-shell, $Dist = r_0 - L$ for (a) negative average IMF B_z after the shock arrival and (b) positive average IMF B_z after the shock arrival. Points that are out of range for this plot are displayed at lower flux ratios, with their actual flux ratio value shown in orange or red. The red colour means that the measured flux before the shock arrival is zero, and it is changed to 10^{-7} particles per ($cm^2 sr MeV$) to avoid division by zero.	82
6.14	Spearman correlation between IMF B_z after the shock and the ratio of electron fluxes as a function of L-shell.	83
6.15	Spearman correlation between the energy input into the magnetosphere after the shock and the ratio of electron fluxes as a function of L-shell.	83
6.16	Spearman correlation between the ratio of the solar wind dynamic pressure after the shock and the ratio of electron fluxes as a function of L-shell.	83
6.17	Spearman correlation between the subsolar magnetopause distance after the shock and the ratio of electron fluxes as a function of L-shell.	83
6.18	Spearman correlation between the distance $Dist$ between the magnetopause location r_0 and the measurement L-shell, and the ratio of electron fluxes as a function of the energy bin (see Table 3.1). The results obtained for the whole data set (blue), for events with average negative IMF B_z after the shock arrival (green), and for events with average positive IMF B_z after the shock arrival (red).	84

A.1	Electron fluxes as a function of time (60 s bins) and L-shell (0.5 bins) for (top) EPT and (bottom) SATRAM for the year 2016. . .	127
A.2	Electron fluxes as a function of time (60 s bins) and L-shell (0.5 bins) for (top) EPT and (bottom) SATRAM for the year 2017. . .	127
A.3	Electron fluxes as a function of time (60 s bins) and L-shell (0.5 bins) for (top) EPT and (bottom) SATRAM for the year 2018. . .	128
A.4	Electron fluxes as a function of time (60 s bins) and L-shell (0.5 bins) for (top) EPT and (bottom) SATRAM for the year 2019. . .	128
A.5	Electron fluxes as a function of time (60 s bins) and L-shell (0.5 bins) for (top) EPT and (bottom) SATRAM for the year 2021. . .	129
A.6	Electron fluxes as a function of time (60 s bins) and L-shell (0.5 bins) for (top) EPT and (bottom) SATRAM for the year 2022. . .	129
A.7	The SATRAM fluxes directly compared with EPT fluxes for the years (a) 2016,(b) 2017, and (c) 2018 with the correlation factors 0.84, 0.82 and 0.85, respectively. The black line is the unity line and the magenta lines mark a one order of magnitude deviation from the unity line.	130
A.8	The SATRAM fluxes directly compared with EPT fluxes for the years (a) 2019, (b) 2021, and (c) 2022 with the correlation factors 0.82, 0.84 and 0.83, respectively. The black line is the unity line and the magenta lines mark a one order of magnitude deviation from the unity line.	130

List of Tables

1.1	Classification of geomagnetic storms according to the Dst index. .	28
3.1	Energy channels in MeV for each particle type.	42
4.1	Particle classification according to the shape of a corresponding track, after Holý et al. [2008].	47
4.2	List of features used in the NN for particle identification.	55
6.1	A list of five strong, isolated geomagnetic storms identified during the DEMETER mission. Selection criteria are: i) Dst index below -100 nT, and ii) no other events in a seven-day period around the storm starting one day before the Dst minimum. The date of each storm type (see text), and the storm source (ICME or CIR) are displayed. Adapted from Gohl et al. [2021].	70

List of Abbreviations

ADC	Analogue-to-Digital Converter
AE	Auroral Electrojet
AL	Auroral Lower (electrojet)
ASIC	Application-Specific Integrated Circuit
ASY	ASYmmetric disturbance index
AU	Astronomical Units
AU (index)	Auroral Upper (electrojet)
CERN	Conseil Européen pour la Recherche Nucléaire (European Organization for Nuclear Research)
CIR	Corotating Interaction Region
CM	Centre of Mass
CME	Coronal Mass Ejection
CMOS	Complementary Metal–Oxide–Semiconductor
CNN	Convolutional Neural Network
CRAND	Cosmic Ray Albedo Neutron Decay
DAC	Data ACquisition
DAM	Digital and Absorber Modules
DEMETER	Detection of Electro-Magnetic Emissions Transmitted from Earthquake Regions
Dst	Disturbance Storm Time
EMIC	ElectroMagnetic Ion Cyclotron
EPT	Energetic Particle Telescope
ESA	European Space Agency
FoV	Field of View
FPGA	Field Programmable Gate Array
GEANT	GEometry ANd Tracking
GC	Geometrical Centre
GCR	Galactic Cosmic Rays
HES	High Energy Section
ICARE	Influence of Space Radiation on Advanced Components (translation from French)
ICME	Interplanetary Coronal Mass Ejection
IDP	Instrument for the Detection of Particle
IMF	Interplanetary Magnetic Field
IP shocks	InterPlanetary shocks
IRBEM	International Radiation Belt Environment Modeling
ISS	International Space Station
LEO	Low Earth Orbit
LES	Low Energy Section
LLBL	Low Latitude Boundary Layer
MEO	Medium Earth Orbit
MIRAM	MIniaturized RAdiation Monitor
MHD	MagnetoHydroDynamics
NGRM	Next Generation Radiation Monitor
NIEL	Non-Ionising Energy Loss

NN	Neural Network
NS	North-to-South
PAN	Penetrating Particle Analyser
PCB	Printed Circuit Board
PIPS	Passivated Implanted Planar Silicon
Proba-V	PRoject for OnBoard Autonomy–Vegetation
PSBL	Plasma-Sheet Boundary Layer
S	South
SATRAM	Space Application of Timepix Based Radiation Monitor
SEU	Single Event Upset
SI	Sudden Impulse
SN	South-to-North
SPENVIS	SPace ENVironment Information System
SSA	South Atlantic Anomaly
SSC	Sudden Storm Commencement
SYM	SYMmetric disturbance index
SWIMMR	Space Weather Instrumentation, Measurement, Modelling and Risk
ToA	Time of Arrival
ToT	Time over Threshold
ULF	Ultra Low Frequency
VLF	Very Low Frequency

List of Publications

- B. Bergmann, St. Gohl, D. Garvey, J. Jelínek, and P. Smolyanskiy. Results and Perspectives of Timepix Detectors in Space—From Radiation Monitoring in Low Earth Orbit to Astroparticle Physics. *Instruments*, 8(1), 2024. ISSN 2410-390X. doi: <https://doi.org/10.3390/instruments8010017>.
- R. Filgas, M. Malich, T. Kuwahara, J. Broulím, M. Holík, M. Sakal, Y. Murata, H. Tomio, St. Gohl, and J. M. Pineda T. RISEPix—A Timepix-based radiation monitor telescope onboard the RISESAT satellite. *Astron. Nachr.*, 340(7):674–680, 2019. doi: <https://doi.org/10.1002/asna.201913674>.
- St. Gohl, B. Bergmann, C. Granja, A. Owens, M. Pichotka, S. Polanský, and S. Pospíšil. Measurement of particle directions in low earth orbit with a Timepix. *J. Instrum.*, 11(11):C11023, 2016. doi: <https://dx.doi.org/10.1088/1748-0221/11/11/C11023>.
- St. Gohl, B. Bergmann, and S. Pospíšil. Design Study of a New Miniaturized Radiation Monitor Based on Previous Experience with the Space Application of the Timepix Radiation Monitor (SATRAM). In *2018 IEEE Nuclear Science Symposium and Medical Imaging Conference Proceedings (NSS/MIC)*, pages 1–7, 2018. doi: <https://doi.org/10.1109/NSSMIC.2018.8824453>.
- St. Gohl, B. Bergmann, H. Evans, P. Nieminen, A. Owens, and S. Pospíšil. Study of the radiation fields in LEO with the Space Application of Timepix Radiation Monitor (SATRAM). *Adv. Space Res.*, 63(5):1646–1660, 2019. ISSN 0273-1177. doi: <https://doi.org/10.1016/j.asr.2018.11.016>.
- St. Gohl, F. Němec, and M. Parrot. Variations in Energetic Particle Fluxes around Significant Geomagnetic Storms Observed by the Low-Altitude DEMETER Spacecraft. *Universe*, 7(8):260, 2021. doi: <https://doi.org/10.3390/universe7080260>.
- St. Gohl, M. Malich, B. Bergmann, P. Burian, C. Granja, E. Heijne, M. Holík, J. Jacúbek, J. Janeček, L. Marek, C. Oancea, M. Petro, S. Pospíšil, A. Smetana, P. Soukup, D. Tureček, and M. Vuolo. A miniaturized radiation monitor for continuous dosimetry and particle identification in space. *J. Instrum.*, 17(01):C01066, 2022. doi: <https://dx.doi.org/10.1088/1748-0221/17/01/C01066>.
- St. Gohl, B. Bergmann, M. Kaplan, and F. Němec. Measurement of electron fluxes in a Low Earth Orbit with SATRAM and comparison to EPT data. *Adv. Space Res.*, 72(6):2362–2376, 2023. ISSN 0273-1177. doi: <https://doi.org/10.1016/j.asr.2023.05.033>.
- M. Ruffenach, S. Bourdarie, B. Bergmann, St. Gohl, J. Mekki, and J. Vaillé. A New Technique Based on Convolutional Neural Networks to Measure the Energy of Protons and Electrons With a Single Timepix Detector. *IEEE Trans. Nucl. Sci.*, 68(8):1746–1753, 2021. doi: <https://doi.org/10.1109/TNS.2021.3071583>.

A. Attachments

A.1 Complete Data for SATRAM comparison with EPT

The figures shown here are the data that was not presented in Section 5.2. The data is from the years 2016 to 2019, 2021, and 2022.

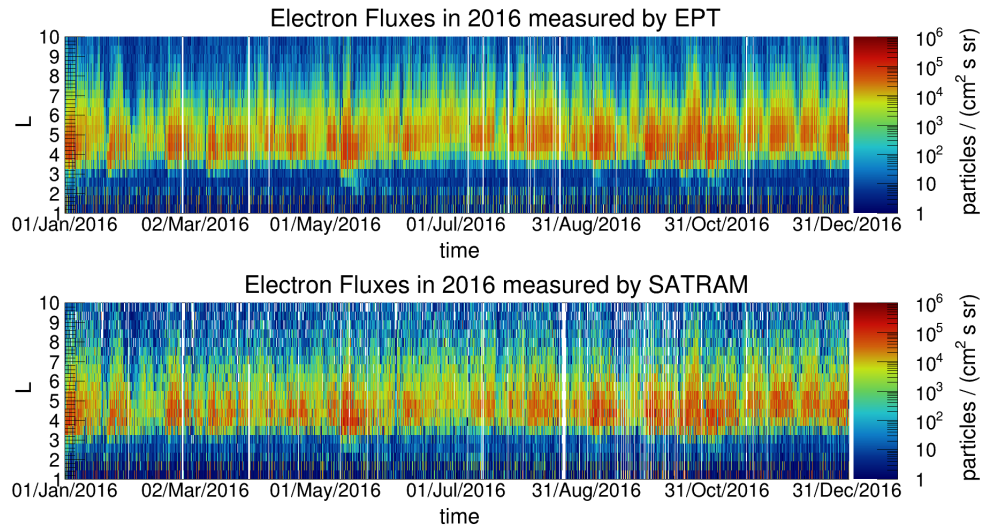


Figure A.1: Electron fluxes as a function of time (60 s bins) and L-shell (0.5 bins) for (top) EPT and (bottom) SATRAM for the year 2016.

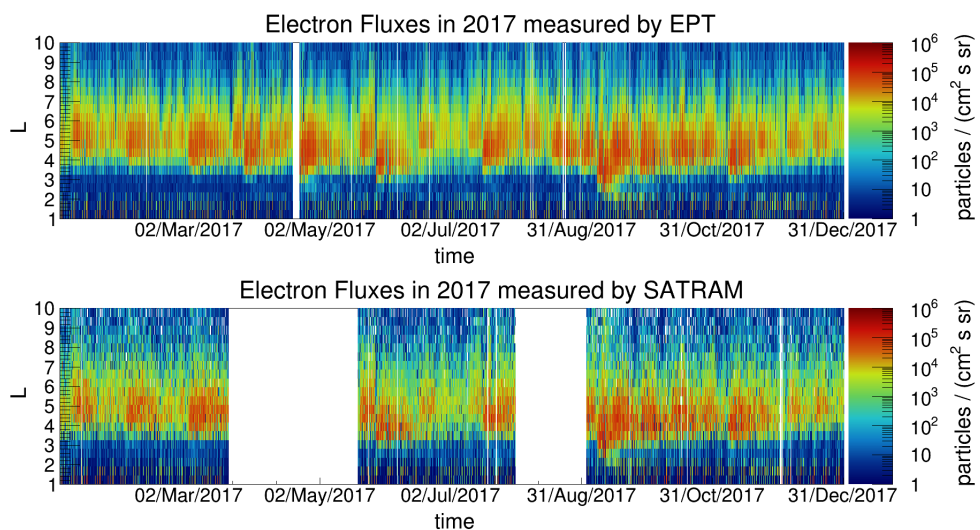


Figure A.2: Electron fluxes as a function of time (60 s bins) and L-shell (0.5 bins) for (top) EPT and (bottom) SATRAM for the year 2017.

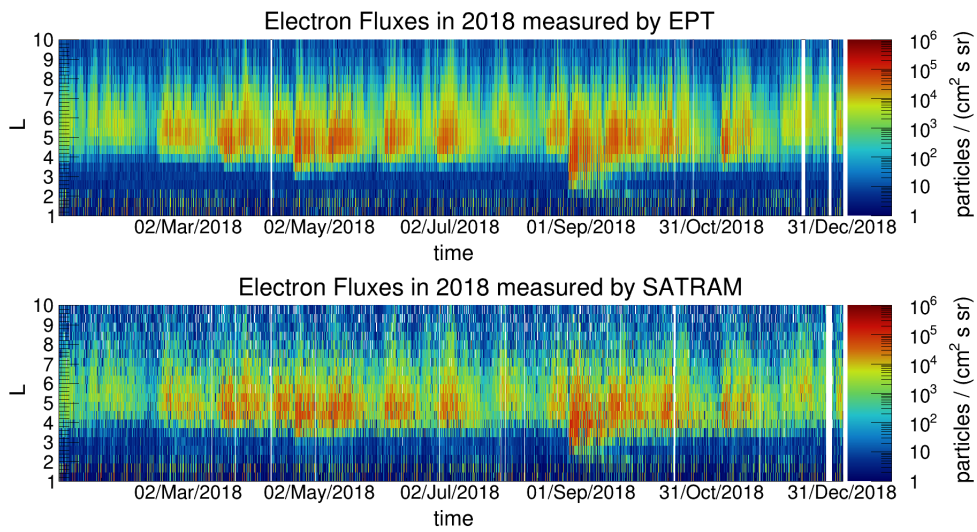


Figure A.3: Electron fluxes as a function of time (60 s bins) and L-shell (0.5 bins) for (top) EPT and (bottom) SATRAM for the year 2018.

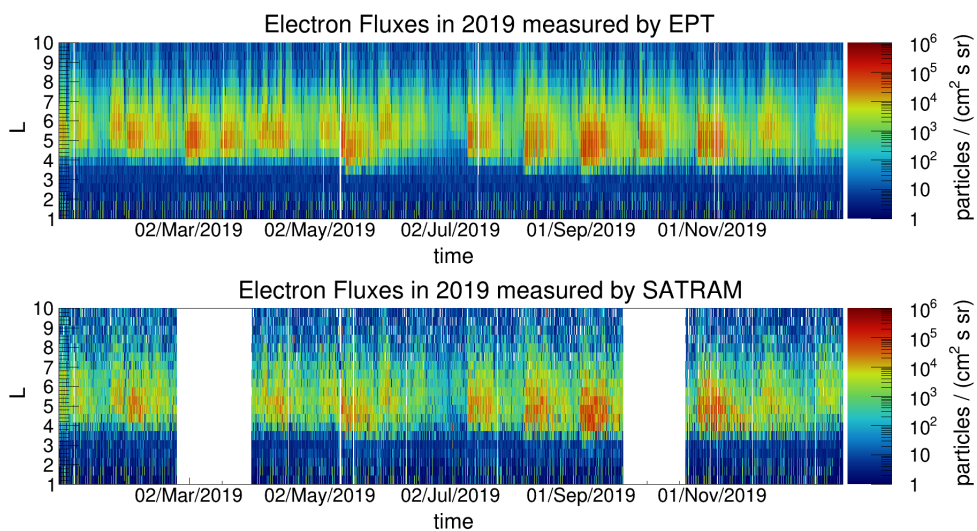


Figure A.4: Electron fluxes as a function of time (60 s bins) and L-shell (0.5 bins) for (top) EPT and (bottom) SATRAM for the year 2019.

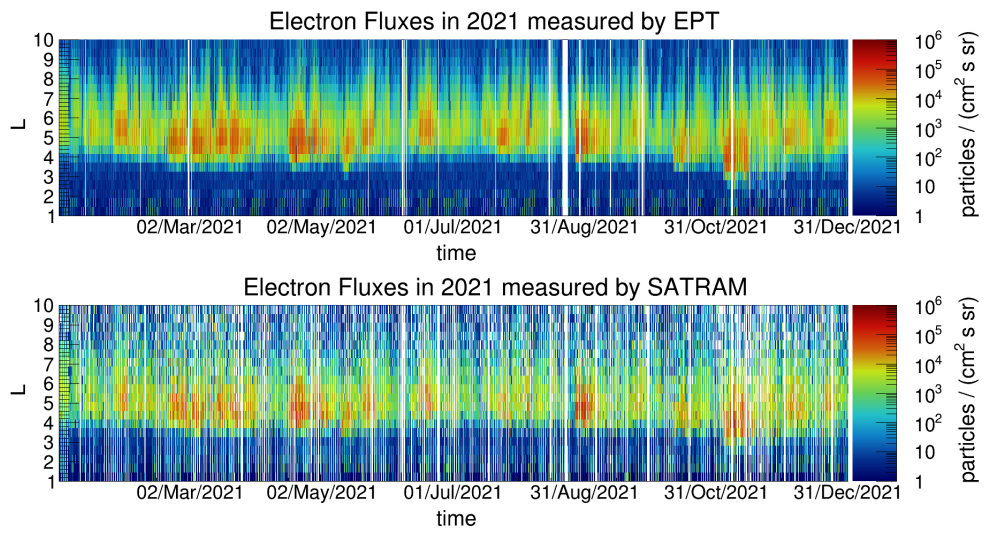


Figure A.5: Electron fluxes as a function of time (60 s bins) and L-shell (0.5 bins) for (top) EPT and (bottom) SATRAM for the year 2021.

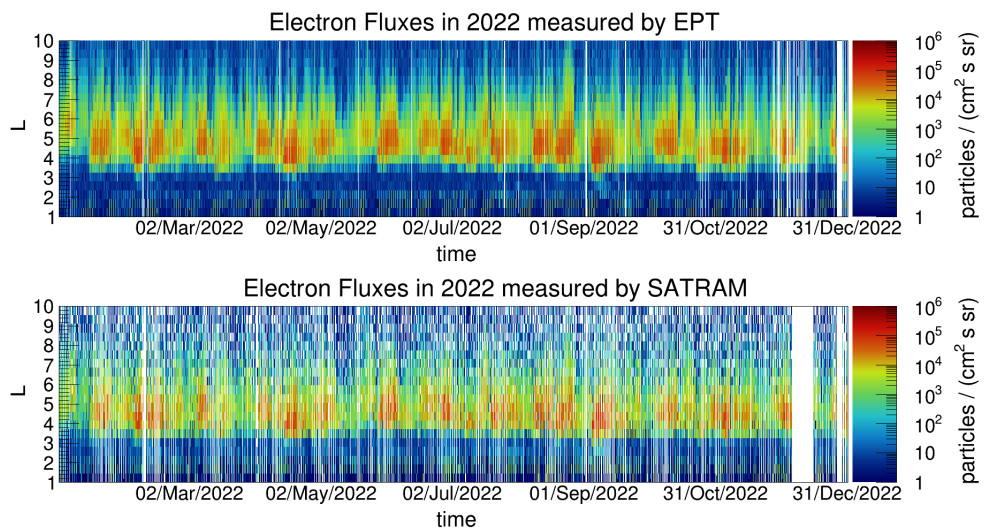


Figure A.6: Electron fluxes as a function of time (60 s bins) and L-shell (0.5 bins) for (top) EPT and (bottom) SATRAM for the year 2022.

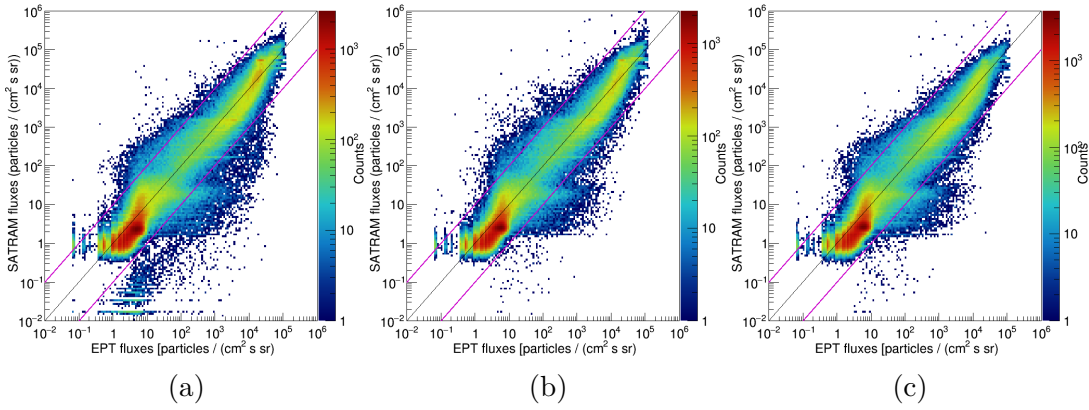


Figure A.7: The SATRAM fluxes directly compared with EPT fluxes for the years (a) 2016, (b) 2017, and (c) 2018 with the correlation factors 0.84, 0.82 and 0.85, respectively. The black line is the unity line and the magenta lines mark a one order of magnitude deviation from the unity line.

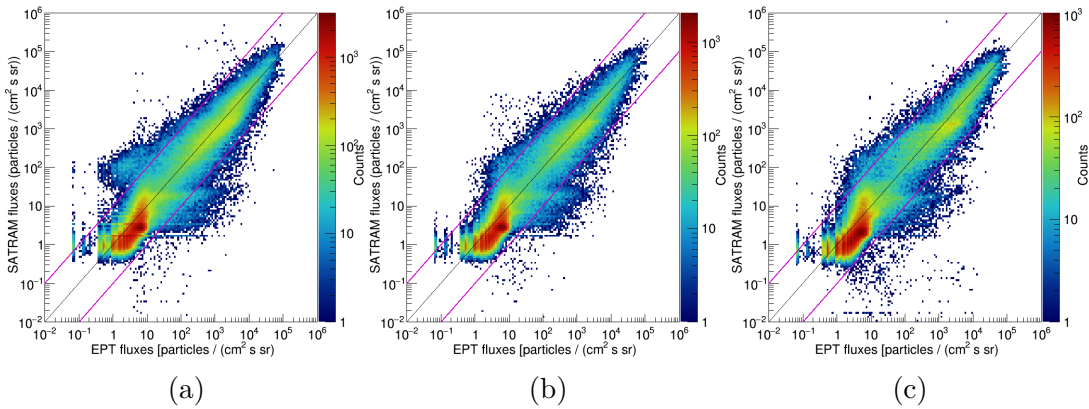


Figure A.8: The SATRAM fluxes directly compared with EPT fluxes for the years (a) 2019, (b) 2021, and (c) 2022 with the correlation factors 0.82, 0.84 and 0.83, respectively. The black line is the unity line and the magenta lines mark a one order of magnitude deviation from the unity line.